Institut für Angewandte Physik
Fachrichtung Physik
Fakultät Mathematik und Naturwissenschaften
Technische Universität Dresden

Local-scale optical properties of single-crystal ferroelectrics

Dissertation
zur Erlangung des akademischen Grades
Doctor rerum naturalium
(Dr. rer. nat.)

vorgelegt von

Tobias Otto
*

(2006)

*Zum Datenschutz sind weitere persönliche Daten in dieser öffentlichen Version unterdrückt.

1. Gutachter: Prof. Dr. L. M. Eng

2. Gutachter: Prof. Dr. G. Gerlach

3. Gutachter: Prof. R. Ramesh

Die Arbeit wurde eingereicht am 17. Januar 2006 und verteidigt am 15. Mai 2006.

Kurzfassung

Das Ziel dieser Arbeit ist die optische Untersuchung von ferroelektrischen Domänen und Domänenwänden auf lokaler Skala. Dafür wurden neuartige nichtinvasive Ansätze entwickelt, die auf der Anwendung optischer Rastersondenmikroskopie basieren. Die untersuchten Schlüsseleigenschaften umfassen den elektrooptischen Effekt für verschiedene Domänenorientierungen und die Brechungindexänderungen an Domänenwänden an Bariumtitanat-Einkristallen.

Die lokale Messung der elektrooptischen Eigenschaften wurde mit räumlich stark begrenzten elektrischen Feldern durchgeführt, die mittels elektrisch leitfähigen Spitzen angelegt wurden. Dieser experimentelle Ansatz erlaubt nicht nur die Messung verschiedener elektrooptischer Koeffizienten, sondern auch die Unterscheidung von allen auftretenden, auch antiparallelen, Domänenausrichtungen. Durch Anlegen eines zusätzlichen elektrischen Feldes mittels der gleichen Spitze konnte auch das ferroelektrische Schalten mit dieser optischen Methode untersucht werden.

Die Experimente wurden durch eine numerische Modellierung der elektrischen Feldverteilung und der resultierenden elektrooptischen Antwort begleitet. Die Ergebnisse der Modellierung sind dabei in sehr guter Übereinstimmung mit den experimentellen Ergebnissen. Dies erlaubt auch die Trennung von Beiträgen verschiedener elektrooptischer Koeffizienten und den entsprechenden Feldkomponenten.

Für die experimentelle Untersuchung von den theoretisch vorhergesagten Brechungsindexprofilen einzelner Domänenwände, wurde die Sensitivität der optischen Sonde auf lokale Änderungen des Brechungsindex mittels Polarisations- und Positionsmodulation erhöht. Obwohl die Abbildung einer einzelnen Domänenwand nicht gelang, konnte damit zumindest eine obere Grenze für den optischen Effekt einer Domänenwand experimentell gewonnen werden, welche verträglich mit den theoretischen Vorhersagen ist.

Abstract

The goal of this thesis is the optical investigation of ferroelectric domains and domain walls at the very local scale. For that, novel noninvasive approaches based on optical scanning probe microscopy are developed. The key properties investigated are the electro-optic effect for different domain orientations and refractive-index changes at single domain walls of barium titanate single crystals.

The local probing of the electro-optic response is performed with strongly confined electric fields, applied via a conductive tip. With this approach we can not only probe different electro-optic coefficients, but also identify all occurring domain orientations, even antiparallel ones. The application of additional bias fields by the same tip is used to investigate ferroelectric switching and domain growth by optical means.

The experiments are supported by numerical modelling of the electric-field distribution and the resulting electro-optic response. The modelling shows excellent agreement with the measurements, and allows us to separate the contributions of different electro-optic coefficients and their associated electric-field components.

For the experimental observation of the theoretically predicted refractive-index profiles at single ferroelectric domain walls, polarization and position modulation of the optical probe is used to obtain high sensitivity to local modifications of the refractive index. An upper limit to the optical effect to the optical effect of a single domain wall is deduced from the experiment, which is compatible with the effect predicted by theory.

Contents

Chapter 1

Introduction

Science, industry, and society promote the 21st century sometimes as the century of the photon [1], since optical technology is conquering the world. An enormous diversity of applications is developing. Information technology, for which optical fiber networks already play an important role, will profit not only from a further increase of bandwidth, for instance by wavelength division multiplexing, but also from direct optical information processing. Light-assisted control of chemical and biological processes will allow production of novel molecules and compounds for sensor applications such as "lab on chip", and for medical purposes, such as specially designed drugs. Additionally, optical technologies allow minimally invasive medical diagnostics and therapy, for instance in combination with endoscopic surgery. Finally, measurements and microscopy with highest resolution will provide not only novel sensory applications, but also a deeper understanding of the fundamental processes in nature.

The development of compact or even integrated optical devices requires the micro- and nano-optical design of materials with tailored optical properties. Photonic crystals, crystals with controllable anisotropy, or photorefractive crystals are only a small selection of such materials allowing the control of the propagation of light at small length scales.

Ferroelectric crystals are typically characterized by outstanding optical properties, including the coupling to electrical fields and mechanical deformations. Therefore, this class of material is a very promising candidate for the development of smart micro- and nano-optical structures and devices. The optical anisotropy of these materials as well as their electro-optical and nonlinear optical properties are strongly linked with their ferroelectric polarization. The latter may be reoriented by sufficiently strong external electric fields, allowing the static and dynamic fabrication of artificial domain arrangements down to the nanoscale. This provides active tunability of optical properties via the domain orientation or the presence of domain walls.

The local-scale characterization of optical properties of ferroelectric domains and domain walls as well as their interaction with localized electric fields is therefore of basic interest for the development of novel or improved optical applications. Therefrom is the basic intention of this work derived, namely to investigate the domain structure at the surface of barium titanate single crystals optically with highest spatial resolution.

For experiments with highest spatial optical resolution, we apply optical scanning probe techniques. Beside confocal laser scanning microscopy, which allows pushing the resolution of classical light microscopy to the diffraction limit, this includes scanning near-field optical microscopy, which provides a resolution much better than the diffraction limit. Since the sample is inspected in a sequence of single points, the operation of very sensitive detectors and additional modulation techniques become possible. If a conductive tip is used as the probe, it may also serve as a local electrode for the external application of electric fields, so that, no further electrodes have to be prepared at the surface of the sample, which therefore can be left in its virgin state.

Concerning the static optical properties, the investigations reported here are focussed on the refractive-index profiles of domain walls, as the optical anisotropy of single-domain states has already been characterized widely by macroscopic experiments. The aim of the related experiments is to find evidence for the theoretically predicted refractive-index profiles of single 180° domain walls.

Much more attention is put on the local change of optical properties induced by external electric bias fields, since this allows us not only to determine the orientation of the ferroelectric polarization completely, but also to investigate the influence of a localized electric-field distribution on ferroelectric switching. This work concentrates on the inspection of barium titanate single crystals since this is one of the best characterized ferroelectric materials. The material parameters, available in the literature, allow a precise theoretical description of the optical properties. The modelling of measurable effects, based on theoretical or given bulk values, finally provides a deeper understanding of the performed experiments.

This thesis is structured as follows. After a general introduction to ferroelectrics in chapter 2, an overview of the materials and instrumentation used is given in chapter 3. The interaction of the addressed optical properties with external bias fields is covered in chapters 4 to 6. The probing of certain electro-optic coefficients for the determination of an already present domain pattern is described in chapter 4. The same method is used in chapter 5 for the measurement of ferroelectric hysteresis. The experimental results of chapters 4 and 5 are finally supported by numerical modelling reported in chapter 6. The theoretical and experimental inspection of the optical properties of single ferroelectric domain walls is reported in chapter 7. The work is concluded by a summary of the most important results and an outlook to future work on this topic.

Chapter 2

Ferroelectricity

Selected historical milestones, related to the discovery of ferroelectricity, open this chapter. This is followed by the basic definition of ferroelectric materials and an introduction to their properties. A short overview of the commonly used theoretical descriptions is given, and then the origin of the most outstanding optical properties of ferroelectrics is discussed in more detail. The chapter closes with a list of selected applications.

2.1 Discovery of ferroelectricity

The following historical remarks are excerpted from [2, 3, 4].

In 1921 Joseph Valasek found ferroelectricity in sodium potassium tartrate tetrahydrate ($NaKC_4H_4O_6\,(H_2O)_4$) for the first time. This material is better known as Seignette or Rochelle salt, since it was prepared first by Elie Seignette in the town of Rochelle, France, in 1655 for medical purposes. Prior to ferroelectricity in Rochelle salt, Brewster discovered its pyroelectric activity in 1824 , P. and P. J. Curie its piezoelectricity in 1880, and Pockels its electro-optic properties in 1894.

The discovery of ferroelectricity in potassium dihydrogen phosphate, KDP (KH_2PO_4) by Busch and Scherer in 1935 lead to the identification of numerous ferroelectric materials of the KDP family. KDP also became the subject of the first outstanding basic theoretical work by J. C. Slater in 1941.

Nevertheless, the final breakthrough in this field is marked by the introduction of ceramic perovskite dielectrics such as barium titanate ($BaTiO_3$) by Wainer and Solomon in 1940. These materials were used for high-k dielectrics in capacitors. Although they were not identified to be ferroelectric at first, the origin of their anomalously high dielectric permittivity raised strong interest. The discovery of ferroelectric switching in barium titanate in 1945 by von Hippel as well as Wul and Goldman showed the existence of ferroelectricity in simple oxide materials for the first time. Hence, barium titanate initiated the discovery of a large number of ferroelectric materials and furthermore a lot of important phenomenological and theoretical work in the field of ferroelectrics.

2.2 Basics of ferroelectricity

Ferroelectrics are characterized by a spontaneous electrical polarization $\vec{P}$ that is switchable by an external electric field $\vec{E}$. This polarization, which is present even in the absence of an external electric field, is common to pyroelectric materials and can emerge from a spontaneous displacement of charged constituents or from spontaneous ordering of built-in electric dipoles. Ferroelectricity is established if the spontaneous polarization can be switched between at least two equilibrium states of orientation by an external field of practicable magnitude. The switching behavior is characterized by a hysteresis loop in terms of the ferroelectric polarization as a function of the external electric field, as illustrated in Fig. 2.1.

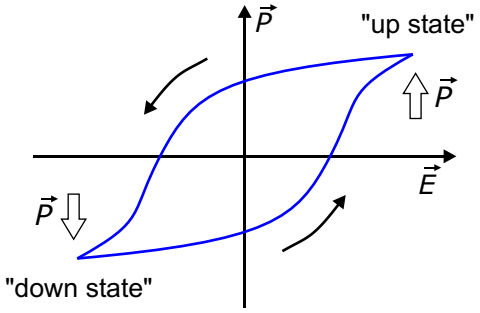

Fig. 2.1 *Hysteresis loop characterizing ferroelectric switching. The application of an external electric field $\vec{E}$ initiates ferroelectric switching of the dielectric polarization $\vec{P}$ between at least two equilibrium states of orientation.*

The occurrence of ferroelectricity is typically limited to certain phases of the material. It vanishes above a critical temperature called the Curie temperature T_C. At this temperature, the material passes through a phase transition of first or second order, and therefore a lot of material properties show a remarkable temperature dependence [5], especially close to this phase transition.

To illustrate the formation of ferroelectric polarization, the structure of the barium titanate unit cell is sketched in Fig. 2.2. For temperatures T above the Curie temperature ($T > T_C$), the material is in its cubic phase, which shows no spontaneous polarization. This phase is not ferroelectric and therefore also called “paraelectric”. Below the Curie temperature ($T < T_C$), the unit cell gets tetragonal, accompanied by a spontaneous shift of the positively charged titanium ions (Ti^{4+}) against the negatively charged oxygen ions (O^{2-}). This leads to a spontaneous electrical polarization $\vec{P}_s$, even without the presence of any external electric field. Since this polarization $\vec{P}_s$ may be reoriented by external fields, this phase is called “ferroelectric”.

In addition to the tetragonal phase, there appear two more structural phases at lower temperatures, which are ferroelectric as well. These phases are characterized by further deformation of the initial unit cell and different orientation of the ferroelectric polarization $\vec{P}_s$ within the unit cell as indicated at the top of Fig. 2.3, which displays also the temperature dependence of the spontaneous polarization for the different phases.

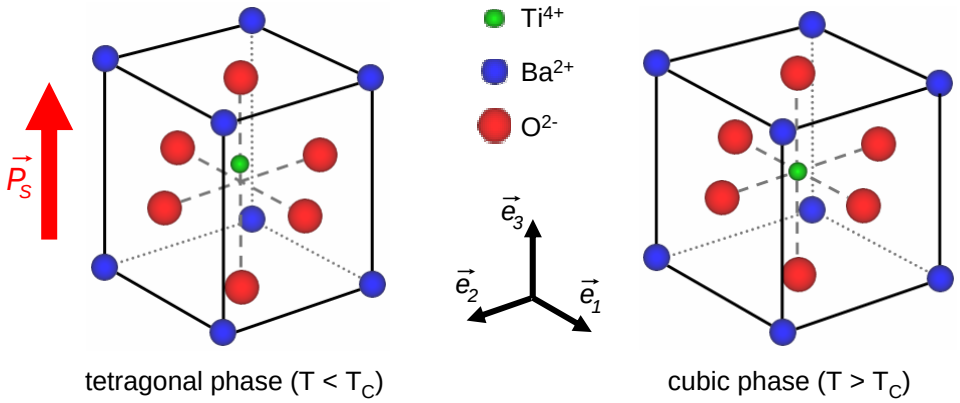

Fig. 2.2 *Structure of the barium titanate unit cell in its tetragonal (left) and cubic (right) phases [6]. In the tetragonal phase, found for temperatures T below the Curie temperature T_C, the positively charged Ti^{4+} ions and the negatively charged O^{2-} ions are displaced with respect to each other along the $\vec{e}_3$ direction. This leads to a spontaneous polarization $\vec{P}_s$. In the cubic phase ($T > T_C$), the centers of mass for positive and negative charges coincide and spontaneous any polarization disappears.*

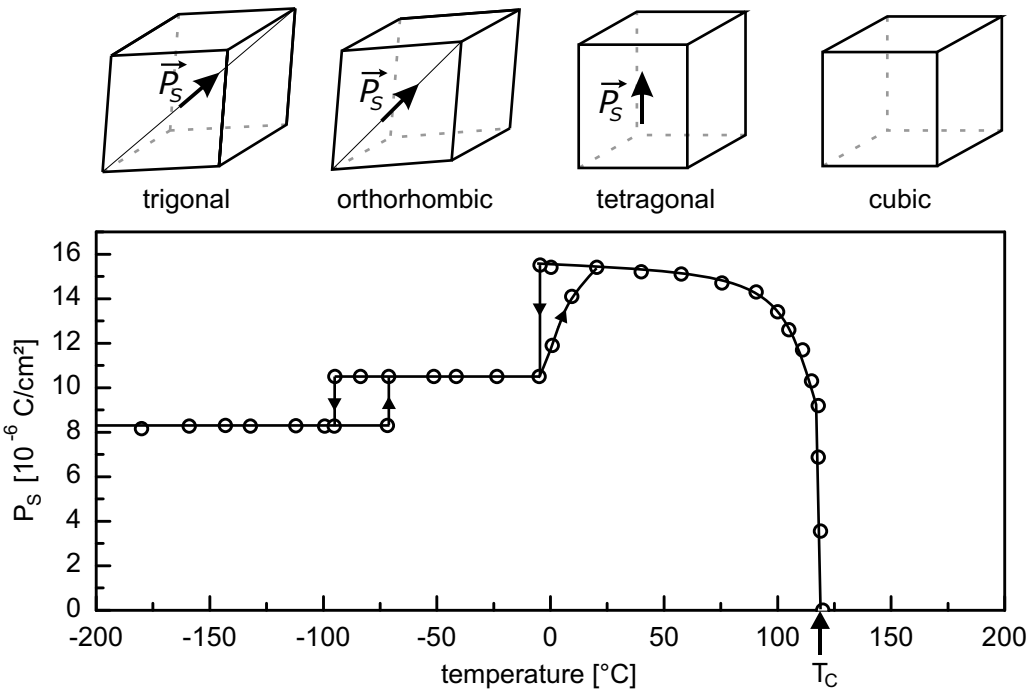

Fig. 2.3 *Spontaneous polarization and structural phases of barium titanate displayed as function of temperature. The sketches at the top schematically show the related unit-cell deformation [7]. The small arrows indicate the orientation of the spontaneous polarization $\vec{P}_s$ within the unit cell. The bottom curve corresponds to the temperature dependence of the spontaneous polarization, indicating the Curie temperature T_C of the phase transition to the ferroelectric phase as well as the two other structural phase transitions at lower temperatures [8].*

At first, ferroelectricity was known to exist in crystalline materials. For this case, the occurrence is closely linked to the crystal symmetry, as illustrated in Fig. 2.4. We find ferroelectric crystals in a subgroup of pyroelectric crystals in up to 10 of the 32 symmetry point groups. Pyroelectric crystals are a subset of piezoelectric crystals and show a spontaneous polarization at zero external field. Because of this hierarchy, it is obvious that all ferroelectric crystals show also pyroelectric and piezoelectric properties.

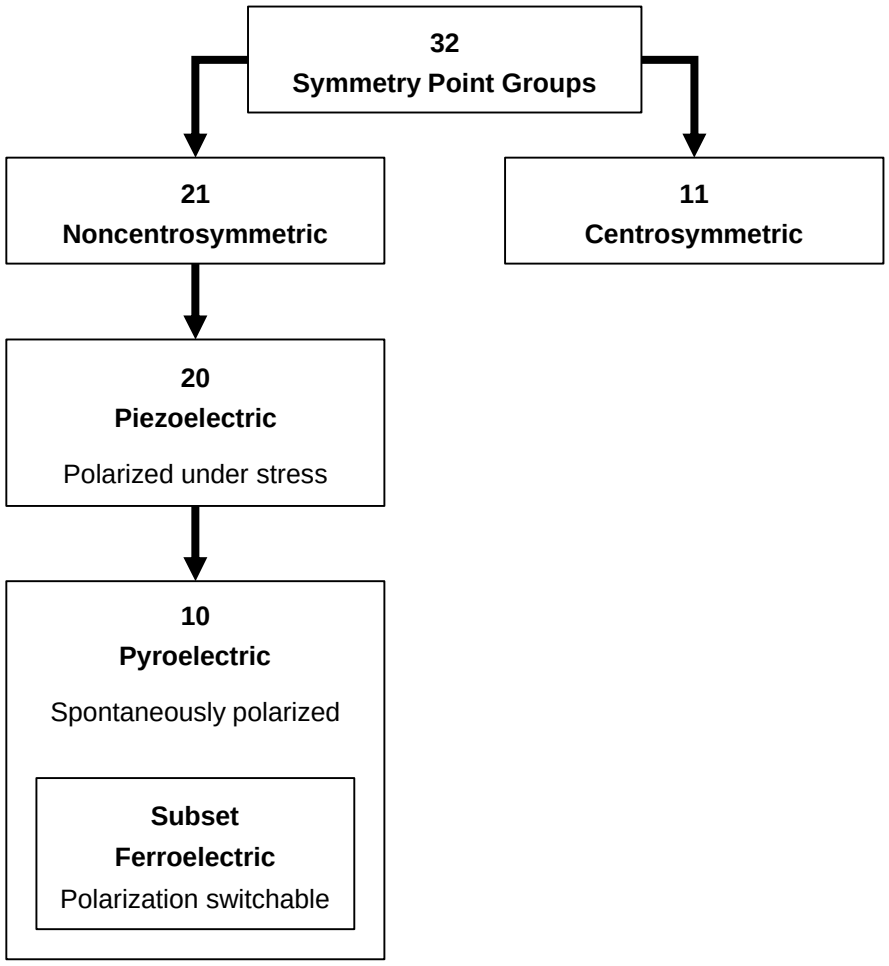

Fig. 2.4 *Classification of ferroelectric crystals on the basis of symmetry point group. A ferroelectric crystal belongs to the group of pyroelectric and piezoelectric crystals as well. Adapted from [3].*

Meanwhile, ferroelectricity has also been found in a variety of other material classes. Germanium telluride ($GeTe$) is a prominent example of ferroelectric narrow-band-gap semiconductors [5]. Liquid crystals reveal ferroelectric properties in certain phases if the molecules provide a net electric dipole moment [9]. There are even ferroelectric polymers, such as for example polyvinylidenfluoride (PVDF) [10], extending the variety of ferroelectric materials.

2.3 Ferroelectric domains

Ferroelectric crystals are not uniformly polarized in general. More typical is the formation of domains characterized by different orientations of the spontaneous polarization. The number of possible domain orientations depends on the material. There are uniaxial ferroelectrics that have only two antiparallel states of orientation like for instance triglycin-sulfate (TGS) or lithium niobate ($LiNbO_3$), while there exist also multiaxial ferroelectrics that have more than two states. Barium titanate for instance can show up to six states of orientation of the spontaneous polarization in its tetragonal phase as indicated in Fig. 2.5. If we assume that the sample surface is parallel to one of the tetragonal unit-cell faces, then these states can be divided into two groups. Four states correspond to the a domain orientation with the spontaneous polarization being parallel to the sample surface, while for the remaining two c domain states the spontaneous polarization is oriented normal to the sample surface.

The driving force for the evolution of a domain structure is the balancing of electrostatic field energy W_e and elastic domain wall energy W_d. In a sample of finite size, the spontaneous polarization P_s is linked with a surface charge $\sigma = P_s$. This charge builds up a depolarization field, which contributes to W_e. The formation of every new domain lowers the electrostatic field energy, while the total energy of the domain walls is increased. Within this simple picture, the balancing of these energies determines the final equilibrium domain structure. In reality, a lot of other interactions, such as impurities, defects, internal and external stress, have an enormous impact on the formation of the domain structure. Therefore, quite complex domain structures can be found, as illustrated:

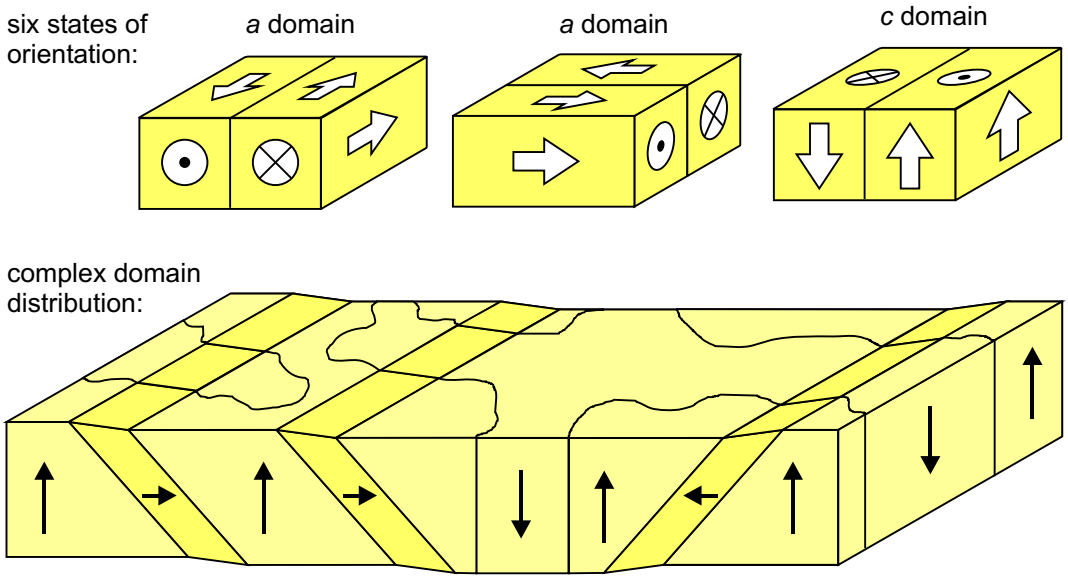

Fig. 2.5 *Ferroelectric domain types and structures of barium titanate in its tetragonal phase. Up to six domain orientations with the spontaneous polarization oriented parallel (a domain) or normal (c domain) to the sample surface can be found. Different domain orientations can be observed to form quite complex domain patterns.*

Concerning the formation of a domain structure, also the thickness of a single domain wall is of interest, since it determines the lower limit of the domain size. In ferroelectrics, no long-range ordering is present and therefore very narrow domain walls with widths in the order of the lattice constant are expected [5]. Nevertheless, a complete understanding is still lacking due to limited experimental data and little theoretical work. The thickness of a 180° domain wall is assumed to be in the order of 5...20 Å [11, 12].

2.4 Theory of ferroelectrics

There is a variety of approaches to describing ferroelectric materials and their properties. Depending on the property or interaction considered, already a phenomenological description can give reasonable results [5]. For that, a macroscopic characterization is used in the framework of classical mechanics and thermodynamics. Such a description is normally formulated in terms of thermodynamic potentials with different sets of variables, considering only mean values of for instance the electric field. Prominent models of this type, such as the Ginzburg-Landau theory, are reported in detail within various textbooks [5, 6, 13, 14].

For studies of the dynamic mechanism of the phase transition as well as the interaction with lattice dynamics, a time-dependent description is required. The description can start in a very microscopic manner with the Hamiltonian of the complete many-body problem. Beside approximations of the Hamiltonian itself, further simplification is achieved by substituting local fields by their mean values. The application of statistical methods finally allows the description in terms of an ensemble average. Within this approach, it turns out that the phase transition is finally connected with the lattice dynamics and can be described within the framework of the "soft-mode" concept [13].

More sophisticated investigations about the microscopic nature of ferroelectric crystals have become popular in recent years. Growing computational power allows first-principle studies accounting for more complex Hamiltonians within the framework of density functional theory [15], Monte Carlo simulations [16, 12], or other methods [17].

Origin of the outstanding optical properties of ferroelectric crystals

Ferroelectric crystals are well known for their outstanding optical properties. Beside strong birefringence, they typically show large values of the electro-optical and nonlinear optical coefficients. The general enhancement of these properties suggests a connection with the occurrence of ferroelectricity, which is characterized by the presence of spontaneous polarization. The latter changes the optical properties by its major contribution to the local electric field. The influence of the spontaneous polarization on the optical properties is also modified by other sources of local electric fields. This idea is supported by various theoretical approaches as follows:

Phenomenological approach

The following considerations are based on a discussion reported in [5]. We start with an expression of Gibbs' free energy G in terms of the dielectric displacement $D = D_i$, with D_i denoting the component along the polar axis i. For a ferroelectric crystal being centrosymmetric in its paraelectric phase, G is given by

$$G = \frac{1}{2}\alpha D^2 + \frac{1}{4}\gamma D^4 + \frac{1}{6}\delta D^6 \,, \tag{2.1}$$

with coefficients α, β, and γ. Since the electric field E is given by the first derivative of G with respect to D, the second derivative yields the inverse dielectric constant $\kappa = \varepsilon^{-1}$, given by

$$\kappa = \varepsilon^{-1} = \alpha + 3\gamma D^2 + 5\delta D^4 \,. \tag{2.2}$$

The displacement D is composed of an electric-field-induced displacement D_E and the spontaneous polarization P_S according to $D = D_E + P_S$. Hence κ can be rewritten as

$$\kappa = \left(\alpha + 3\gamma P_S^2 + 5\delta P_S^4\right) + \left(6\gamma P_S + 20\delta P_S^3\right) D_E + \left(3\gamma + 30\delta P_S^2\right) D_E^2 + \dots \,. \tag{2.3}$$

At optical frequencies, we can express ε in terms of the refractive index n as $\varepsilon = n^2\varepsilon_0$, and Eq. 2.3 can be written as

$$\kappa = \left(n^2\varepsilon_0\right)^{-1} = \left(n_0^2\varepsilon_0\right)^{-1} + f' D_E + g' D_E^2 + \dots \,, \tag{2.4}$$

with the refractive index at zero external field n_0 and the coefficients f' and g' describing the linear and quadratic electro-optic effect respectively. To the lowest order in P_S, these parameters are identified as

$$n_0^{-2} = \varepsilon_0\alpha + 3\varepsilon_0\gamma P_S^2 \quad \text{, and} \quad f' = 6\gamma P_S = 2g' P_S \,. \tag{2.5}$$

This indicates a change Δn of the refractive index along the polar axis being proportional to the square of the spontaneous polarization. Furthermore, the coefficient for the linear electro-optic effect f' is found to be the same as for the quadratic electro-optic effect g', multiplied by the spontaneous polarization P_S. Thus, the spontaneous polarization affects the birefringence and the linear electro-optic properties of ferroelectric crystals, qualifying it to be one source of the outstanding optical properties.

Microscopic approach

The dielectric interaction of light with matter is primarily characterized by the electronic polarization induced by the optical fields $\vec{E}^o$ in each individual constituent atom or ion i. Any type of additional interaction with the electrons of the constituents will change the polarizability, which leads to altered optical properties. At this point, the primary focus is put on the influence of the spontaneous polarization again. Within the lattice of a ferroelectric crystal, the influence of this polarization is included in the interaction with

the local electric field $\vec{E}$. Since the spontaneous polarization is generated by the special configuration of the crystal lattice, the corresponding local electric fields also show a strong dependence on lattice deformations and lattice dynamics. Therefore, a variety of secondary interactions affect the optical properties via changed local electric fields.

The primary effect of the local electric field $\vec{E}$ on the electronic polarizability of each individual ion of the considered ferroelectric crystal can be derived by quantum mechanical perturbation theory [18]. With this fundamental approach, a diversity of problems such as the optical properties of domain walls [19, 20] or thin films [21] can be addressed. Selected aspects of this method and its application to the optical properties of single ferroelectric domain walls are summarized in chapter 7.2.

For the description of the optical properties with respect to the local electric field, the electronic dipole moment $\vec{p}^{\,e}(i)$ for each individual ion i can be condensed to

$$p_k^e(i) = \alpha_0(i)\left[1 - \theta_k(i)E^2 + \ldots\right] E_k \,, \tag{2.6}$$

with the polarizability $\alpha_0(i)$ of the free ion i at zero field, and $\theta_k(i)$ describing moments of the electronic charge distribution with respect to the dominating component of $\vec{E}$ [22]. For further discussion, the local electric field $\vec{E}$ can be split into the contributions of bias fields $\vec{E}^b$ and optical fields $\vec{E}^o$. An expression for the electronic polarizability with respect to the optical fields $\widetilde{\alpha}_{kl}^o(i)$ is determined by taking the derivative of $\vec{p}^{\,e}(i)$ with respect to $\vec{E}^o$:

$$\widetilde{\alpha}_{kl}^o(i) = \frac{\partial}{\partial E_l^o} p_k^e(i) = \alpha_0(i)\left[\delta_{kl} - \theta_k(i)\left(E^2(i)\delta_{kl} + 2E_k(i)E_l(i)\right) + \ldots\right] . \tag{2.7}$$

Considering only effects being linear in $\vec{E}^o$, we omit all terms of Eq. 2.7 containing additional components of $\vec{E}^o$, since they describe purely nonlinear-optical effects. The resulting $\widetilde{\alpha}_{kl}^o(i)$ can be expressed in matrix notation by (qualifier i omitted)

$$\widetilde{\alpha}_{kl}^o = \alpha_0 \begin{pmatrix} 1-\theta_1(E^b)^2-2\theta_1(E_1^b)^2 & -2\theta_1 E_1^b E_2^b & -2\theta_1 E_1^b E_3^b \\ -2\theta_2 E_1^b E_2^b & 1-\theta_2(E^b)^2-2\theta_2(E_2^b)^2 & -2\theta_2 E_2^b E_3^b \\ -2\theta_3 E_1^b E_3^b & -2\theta_3 E_2^b E_3^b & 1-\theta_3(E^b)^2-2\theta_3(E_3^b)^2 \end{pmatrix} . \tag{2.8}$$

The influence of the spontaneous polarization $\vec{P}_s$ can be discussed in terms of the corresponding field $\vec{E}^s(i)$ by assuming $\vec{E}^b(i) = \vec{E}^s(i) \sim \vec{P}_s$, where the absolute value of $\vec{E}^s(i)$ may still vary with ion i. Since the reference frame is chosen such that $\vec{P}_s$ points along $\vec{e}_3$, only the 3-component E_3^s remains and Eq. 2.8 is simplified to

$$\widetilde{\alpha}_{kl}^o = \alpha_0 \begin{pmatrix} 1-\theta_1(E_3^s)^2 & 0 & 0 \\ 0 & 1-\theta_2(E_3^s)^2 & 0 \\ 0 & 0 & 1-3\,\theta_3(E_3^s)^2 \end{pmatrix} , \tag{2.9}$$

indicating that already the contribution of ion i to the optical properties depends quadratically on the field $\vec{E}^s$. The same is true for the macroscopic optical properties, as derived

by averaging all contributions $\widetilde{\alpha}^{o}_{kl}(i)$ of the constituent ions i across the unit cell. This finally illustrates that the influence of the spontaneous polarization on the birefringence of a ferroelectric specimen is proportional to $(\vec{P}_s)^2$, similar to the findings of the phenomenological approach.

Within this framework, also the purely electronic contribution to the electro-optic effect of a single ion can be discussed by adding an external electric field $\vec{E}^e$ to the local electric bias field according to $\vec{E}^b(i) = \vec{E}^s(i) + \vec{E}^e$. Eq. 2.8 yields

$$\widetilde{\alpha}^{opt}_{kl}(i) = \widetilde{\alpha}^{opt}_{kl}(i)|_{\vec{E}^e=0} + \widetilde{\alpha}^{(eo)}_{kl}(i) + \dots \,, \tag{2.10}$$

with $\widetilde{\alpha}^{(eo)}_{kl}(i)$ being the linear contribution in terms of the external electric field $\vec{E}^e$, given by

$$\widetilde{\alpha}^{(eo)}_{kl} = \alpha_0 \begin{pmatrix} -2\theta_1 E^s_3 E^e_3 & 0 & -2\theta_1 E^s_1 E^e_3 \\ 0 & -2\theta_2 E^s_3 E^e_3 & -2\theta_2 E^s_2 E^e_3 \\ -2\theta_3 E^s_1 E^e_3 & -2\theta_3 E^s_2 E^e_3 & -4\theta_3 E^s_3 E^e_3 \end{pmatrix} . \tag{2.11}$$

It turns out that all contributions being linear in the external field $\vec{E}^e$ occur only in combination with E^s_3 (Eq. 2.11), underlining that the electro-optic coefficients are strongly influenced by the value of the spontaneous polarization.

Altogether, the discussion presented considers the electronic contributions in an isolated form only. Due to dipole-dipole interaction between the constituent ions as well as ionic and other lattice coupling, a lot of further contributions are missing in this description. Nevertheless, already the purely electronic contribution reveals the basic dependence of the optical properties on local electric fields.

2.5 Applications

The general importance of ferroelectric materials stems not only from their ferroelectric properties, that means the switchable polarization itself, but even more from their exciting dielectric, pyroelectric, piezoelectric, electro-optic, and nonlinear-optic properties. From these properties result a huge area of functionalities.

Ferroelectric materials typically exhibit large values of dielectric permittivity. Therefore, they are suitable for the application as high-k ($k{=}\kappa{=}\varepsilon/\varepsilon_0$) material in capacitor structures, such as multilayer thin-film capacitors and decoupling capacitors in microwave monolithic integrated circuits (MMIC). They are also used as cell dielectric in dynamic random access memory (DRAM) devices, or as gate oxide material in field effect transistors [23]. The pyroelectric properties are used for temperature sensing and infrared-radiation detection, which is a basis for infrared imaging also [5]. The piezoelectric properties are not only used for simple electric actuators. They are also one of the basic ingredients in microelectromechanical systems (MEMS), which combine electronics with sensors, transducers, and actuators [23]. Beside the piezoelectric properties, such devices may incorporate also other

material properties. Applications of MEMS cover for instance piezoelectric micromotors and pumps, air-bag accellerometers, actuating cantilevers, chemical micro-sensors, and micro-mirror displays. MEMS are also applied for surface-acoustic-wave (SAW) filters, pyroelectric IR microsensors, and ultrasonic high-frequency imaging [23].

Ferroelectric crystals of sufficient optical quality have a lot of further applications. Acousto- and electro-optic modulators make use of the extraordinary piezoelectric and electro-optic properties of such crystals. Another application is holographic data storage, which makes use of the photorefractive properties [11]. Furthermore, the large nonlinear optical effects in ferroelectric crystals are used for applications in optical frequency conversion [11], where conversion efficiency is increased by quasi-phase matching, which can be realized by a specific pattern of periodically poled domains.

Beside quasi-phase matching, only a minority of applications makes direct use of ferroelectric domain orientation so far. The most propagated one is information storage either in nonvolatile memory cells such as ferroelectric random access memories (FRAM) [23] or in nanoscopic mass data storage devices [5]. Nevertheless, the growing interest in smart materials and structures and integration of more complex functionalities will push this field of applications further [11].

Chapter 3

Materials and instrumentation

This chapter gives an overview of the materials and instrumentation used. After the description of the barium titanate single-crystal samples, the focus is put on the characterization of the probes used for the optical scanning probe experiments of this work. The presentation of the instrumentation includes also a description of common scanning probe techniques. The chapter closes with notes about the incorporated laser light sources and detector modules.

3.1 Barium titanate single crystals

The present work is focussed on the investigation of single crystalline barium titanate. It is one of the best investigated ferroelectric materials and therefore a lot of crystal parameters are available in the literature [24]. Barium titanate has a perovskite structure and can be found in four different structural phases depending on temperature, as already illustrated in Fig. 2.3. Since the experiments of this work are run at room temperature, only the tetragonal phase is addressed here. There we find up to six orientations of ferroelectric polarization, which can form a complex domain structure (Fig. 2.5). This allows us to study all major domain orientations not only in a single sample, but also in a single experiment.

The single-crystal pieces used in this work were grown by the Remeika method [25]. The crystal thickness varies from sample to sample in the range of 100...200 µm, while the lateral size is in the order of a few millimeters. The samples are highly transparent and have a yellowish color as shown in Fig. 3.1. This is in accordance with the recorded transmittance spectrum revealing increased absorption for wavelengths shorter than 450 nm. Similar crystals have been characterized by piezoresponse force microscopy, polarized-light microscopy, and micro-Raman spectroscopy in previous work of our group, partly in cooperation with others [26, 27].

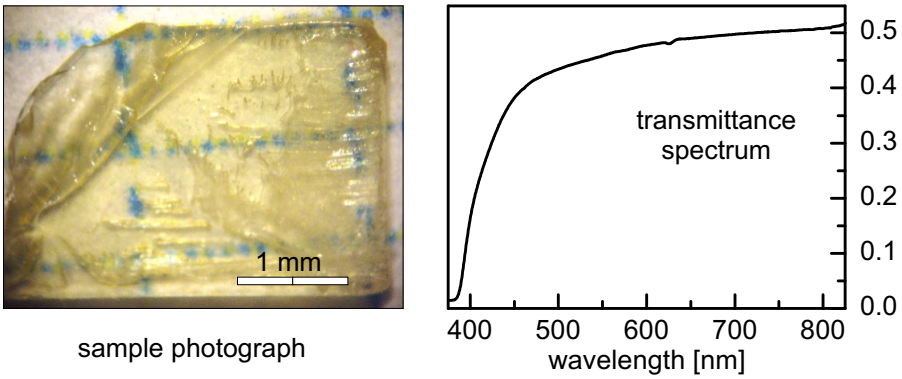

Fig. 3.1 *Properties of a barium titanate single-crystal sample. The transparent crystal of about 200 µm thickness shows a yellowish color. This is also in agreement with the transmittance spectrum indicating increased absorption at wavelengths shorter than 450 nm. The spectrum was kindly provided by T. Härtling.*

The material parameters of barium titanate reported in the literature vary significantly [24]. This variation stems not only from experimental errors. Much more influence can be attributed to the quality of the investigated samples. Already slightly changed compositions and different impurity or defect concentrations can change certain material parameters significantly [28, 29]. In this work, we therefore mainly use reference values of dielectric and optical properties of barium titanate taken from a review [24]. Selected parameter values reported in that work are listed in Table 3.1. The material parameters of the individual samples examined in this work may differ from the tabulated values, which constitutes an additional source of errors.

Table 3.1 *Dielectric and optical constants of barium titanate [24].*

dielectric permittivity	refractive index	electro-optic coefficients	
		unclamped	clamped
$\varepsilon_{11} = 4400$	$n_a = 2.41$	$r_{113} = 8$ pm/V	$r_{113} = 10.2$ pm/V
$\varepsilon_{33} = 130$	$n_c = 2.36$	$r_{333} = 105$ pm/V	$r_{333} = 40.6$ pm/V
		$r_{131} = 1300$ pm/V	$r_{131} = 730$ pm/V

Broad application of single-crystalline barium titanate is limited so far by the difficulty of crystal growth and the relatively low Curie temperature of 120°C. Nevertheless, its large value of spontaneous polarization makes it suitable for nonlinear-optical applications and the large electro-optic constants favor barium titanate crystals for the use as photorefractive material. Finally, the lead-free composition of barium titanate makes it attractive as a replacement for lead-based piezoelectrics [30].

3.2 Optical scanning probe microscopy

In optical scanning probe microscopy, the sample is inspected in a sequence of single-point measurements. In contrast to the parallel imaging of multiple sample points, which is used in classical light microscopy, this drastically extends the available range of optical excitation and detection techniques. For measurements at low light levels or detection of modulated signals at high frequencies, single-point detectors such as photodiodes can be used. Because of the simplification to single-point measurements, also the optical excitation and/or detection may be restricted to very small volumes. Depending on the probe type used, this allows us to improve the available spatial resolution by confining the optically addressed area.

There are several approaches to the implementation of confined optical probes. The classical one is the use of the confinement in a focal spot. In this case the resolution is limited by diffraction. The limitation can be overcome by placing a small aperture very close to the point of interest. This idea goes back to a proposal of E. H. Synge in 1928 [31], and allows one to detect the near field of the sample, which is composed of propagating (detectable also in the far field) and non-propagating (detectable only very close to the sample) light.

The most common principle of aperture probes is to couple light through a small hole in a tapered metal structure. Such optical tips can be produced, for example, from optical fibers by etching or pulling with subsequent metal deposition [32]. Another option is to use a microfabricated structure based on silicon technology as aperture [33]. The problem of all these tips is the small overall transmittance of such probes, which stems not only from the small aperture, but also from an effect called cut-off, which means that an optical wave gets exponentially damped if it is confined in structures smaller than its wavelength [34].

An alternative way to confine the optically inspected sample volume is to use a probe that scatters light from the point of interest [35, 36]. Whether the scattering is supported by local enhancement of optical fields due to plasmonic resonances [37] or not, the problem of this type of scanning near-field optical microscopy (SNOM) is the separation of the near-field signal from the background light [38], while the confinement of the inspected volume might be much easier than in aperture SNOM.

3.2.1 Diffraction-limited focal spot

The diffraction-limited focal spot is typically used in confocal laser scanning microscopy, an advancement of classical microscopy. Here, the exciting laser light is focussed onto a single spot of the sample. By using an objective with a high numerical aperture, the focal spot is confined laterally and axially, allowing one to address a narrow layer of the sample. The origin of the light detected is further limited by an additional aperture in the image plane. This eliminates out-of-focus light and increases resolution towards the diffraction limit.

In the present setup, a high-numerical aperture objective (Zeiss NA 1.3) with immersion oil is used, offering not only a small spot size but also excellent polarization properties. Figure 3.2 illustrates the focussing and shows the achieved resolution measured at an *a*-*c* domain transition of a barium titanate sample with properly selected polarization of the light.

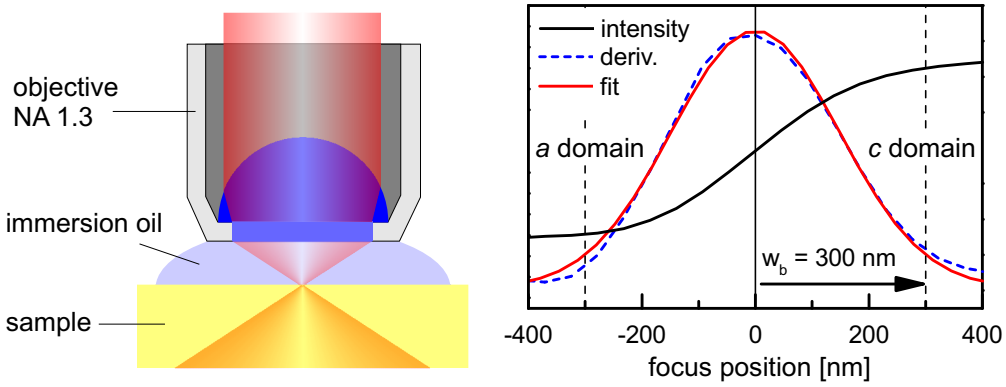

Fig. 3.2 *Diffraction limited spot produced by focussing a laser beam with an objective of high numerical aperture of 1.3 combined with immersion oil. The spot size is deduced by scanning the spot across an a-c domain transition with properly adjusted polarization.*

3.2.2 Etched fiber tips

There are several methods reported for the etching of fiber tips [39, 32, 40, 41, 42]. Commonly, a reagent based on hydrofluoric acid is used, covered with a liquid such as iso-octane to prevent fast evaporation. The basic approach is to etch the bare fiber by simply dipping it into the reagent [41]. The disadvantage of this method is that the etching process is strongly affected by convection and mechanical disturbances. This is the reason why the resulting tips often show a rough surface. Another approach uses the selective etching behavior of the fiber core and cladding combined with a very small depth of dipping, which has to be controlled during the etching process. This way, one can produce high-quality tips but with a big effort [42]. Therefore, we use in our group the quite common method of tube etching [39]. Here, the fiber is etched inside its acrylate jacket. This protects the etching process from large-scale convection and mechanical disturbances and leads to tips with a much smoother surface. However, one finds that the etching result depends strongly on the type of fiber used. One reason for this may be the different properties of the fiber jacket, since the etching depends more on the transport of the reagent and of the products of the etching process through the fiber jacket [43, 44] than through its open end, as proposed by [39]. For the preparation of tips by tube etching, we use a fiber of type FS-SN-3224. This fiber is manufactured by the company 3M and designed for single-mode operation at a wavelength of 630 nm.

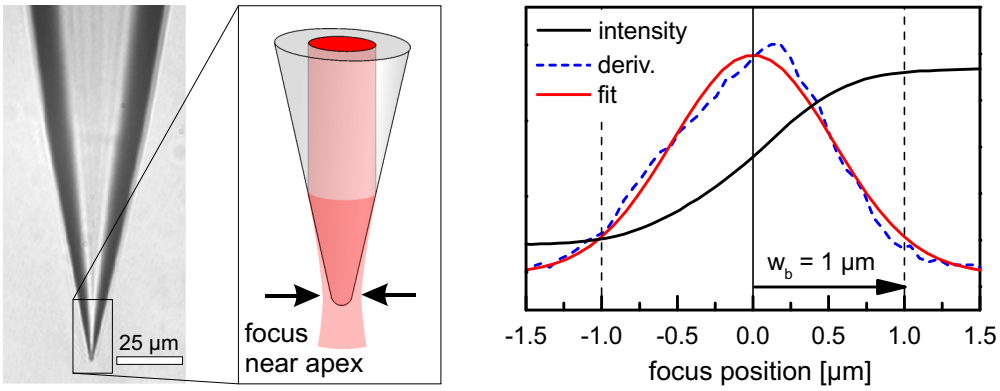

Fig. 3.3 *Fiber tip prepared by tube etching. The tapered end leads to an additional focussing of the light. The spot size at the apex is measured by recording the transmitted light intensity while the tip is scanned across a step of a vapor-deposited chromium layer. The spot size is found to be in the order of 2 µm in diameter.*

Because of the tapered shape of the fiber tip the emitted light is slightly focussed close to the tip apex (Fig. 3.3). The spot at the tip apex may be characterized by scanning the approached tip across a thin structured chromium film, while topography and transmitted light intensity are being recorded. With this, not only the spot diameter at the tip apex, but also the lateral displacement between tip apex and the center of the spot can be determined. The obtained spot diameter varies in the range of 1..4 µm, but is found to be in the order of 2 µm for most of the tips. The lateral shift between the center of the spot and the apex is found to be up to 0.5 µm.

For the application of electric fields, such bare optical fiber tips are turned into electrically conductive probes by an ultrathin chromium coating of a few nanometers in thickness. This provides sufficient conductivity, while still leaving the tip semitransparent [45]. Compared to the deposition of other transparent conductors such as indium tin oxide (ITO), the preparation of the chromium layers is very easy.

Since there is no additional aperture limiting the radiation at the apex, these tips provide high output intensities as well as very good polarization properties in general. This means that very high degrees of linear polarization in excess of 90% are reached for any selected orientation, typically.

3.2.3 Pulled fiber tips with aperture

Pulled fiber tips are produced by pulling a locally heated optical fiber until it is teared apart into two tapered fiber ends. The tip shape depends on the heating parameters as well as on the pulling force. Pulled tips exhibit smaller opening angles than etched fiber tips, and may therefore exhibit less mechanical stability. In combination with a deposited metal aperture the small opening angle also increases the cut-off effect, so the transmitted power decreases even more.

The pulled tips used in this work, purchased from Nanonics, have a specified aperture of 50 or 100 nm (Fig. 3.4), and provide very low output powers of usually no more than 0.1 nW. In the experiments, it was found that these tips often show poor electrical conductivity, at least at the apex. The polarization properties of these tips are characterized by degrees of linear polarization of more than 50%, but also by a quite strong orientation dependence, which can be attributed to asymmetries of the metal aperture.

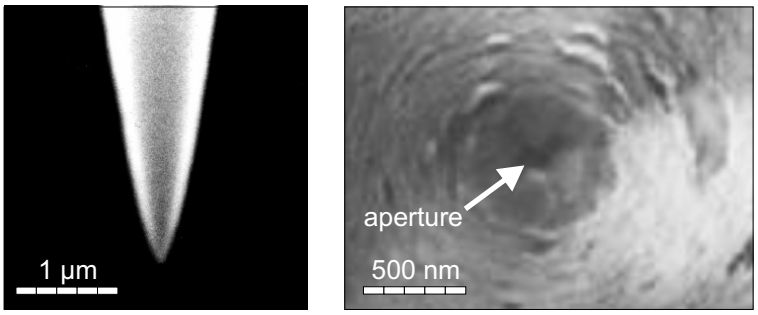

Fig. 3.4 *SEM micrographs of a pulled fiber with a deposited metal layer forming an aperture of about of 100 nm in diameter (source: Nanonics datasheet).*

3.2.4 Cantilever SNOM probes

These microfabricated probes are prepared on the base of a silicon cantilever structure, which is covered with an aluminum layer. This metal layer forms also a hollow pyramid with the aperture at its apex. The pyramid has a comparably large opening angle and the diameter of the aperture is specified to be about 100 nm as shown in Fig. 3.5.

To operate these tips, one has not only to couple light through the aperture, but also to control the tip-sample separation by detection of the cantilever bending. This is usually done by complex optics combining light coupling and beam deflection into a single system. Unfortunately, such a system could not be integrated into our present optical scanning probe stages effectively, and therefore these cantilever probes are operated differently.

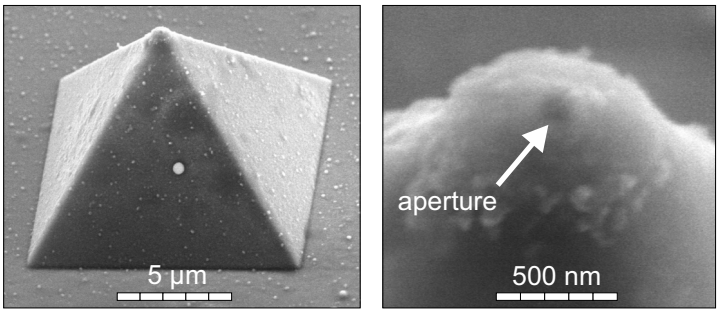

Fig. 3.5 *SEM micrograph of a cantilever SNOM probe after excessive use. The aperture at the apex of the hollow pyramid with a diameter of about 100 nm is surrounded by a ring of particles picked up during scanning.*

The approach we used is based on gluing a cleaved optical fiber with its flat end face onto the cantilever, as illustrated in Fig. 3.6. It was found that this provides efficient light coupling through the aperture. Before attaching the fiber to the cantilever, it is coated by black paint to reduce stray light emission from the fiber side wall. The transparent glue is hardened in a state that has been adjusted to provide the highest light coupling ratio. After removal of the extending parts of the lever by mechanical breaking, the remaining part is contacted electrically by conductive silver paint. After this preparation, these tips are operated like any other standard tapered-fiber probe.

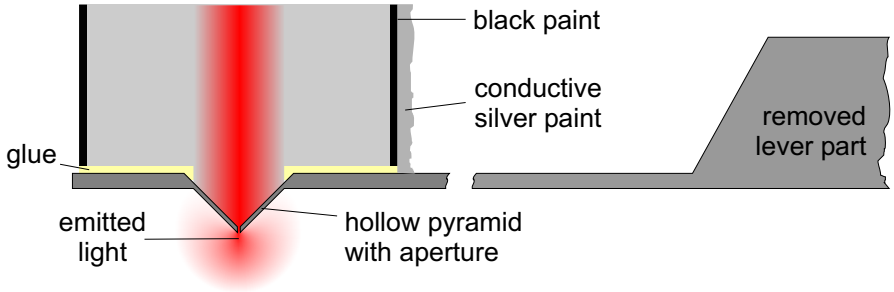

Fig. 3.6 *Steps for conversion of a SNOM cantilever probe into a fiber probe. The cleaved optical fiber, coated by black paint for stray light reduction, is glued onto the cantilever in a position adjusted for maximum transmitted intensity. After hardening of the glue, the extending parts of the lever are broken away and the remaining part is contacted electrically by conductive silver paint.*

In our setup, an optical output power of up to 50 nW was achieved with these tips. But like the pulled aperture probes, these probes are characterized by moderate polarization properties. Again, only low degrees of polarization in the order of 50% are achieved and a strong orientation dependence is observed. However the well defined and robust metal structure of these micromachined tips exhibits a very good electrical conductivity in contrast to the pulled aperture probes.

3.3 Instrumentation

3.3.1 Inverted optical microscope

The present setup is based on an Zeiss Axiovert 135 TV inverted optical microscope [46]. It is equipped with a piezo-driven actuator frame allowing us to scan the sample in three dimensions with respect to the fixed optical axis of the microscope as illustrated in Fig. 3.7. The inverted body of the microscope allows the attachment of additional scanning probe stages such as SNOM or AFM on top of the scanned sample. All scanning probe stages allow manual positioning with respect to the optical axis of the microscope. This and the

positioning of the sample can be done with the accuracy given by the optical inspection through the microscope. Therefore, the setup allows us to apply different scanning probe as well as additional optical methods to collect complementary information from the same selected spot on sample without a single removal of the sample.

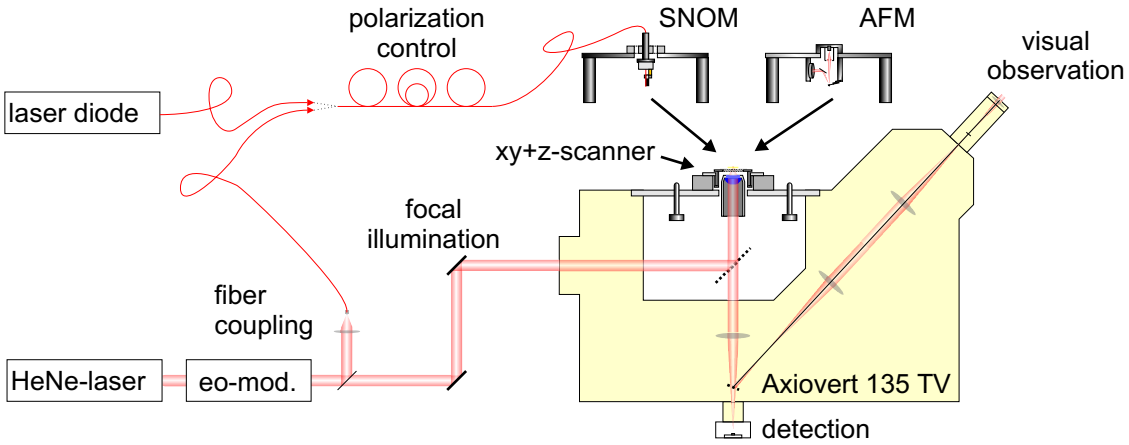

Fig. 3.7 *The Axiovert 135 TV inverted optical microscope as experiment platform. Equipped with a 3D piezo-driven sample scanner, the microscope is the basis for scanning probe experiments featured with excellent optical observation and detection capabilities. The modular design allows combination of different methods to obtain information from the same sample position. For optical excitation, there are various laser light sources at different wavelengths available. They can be equipped with modulation capabilities for intensity or polarization modulation. The laser light can be used for focal excitation or for illumination through a SNOM fiber.*

3.3.2 SNOM stage

The operation of the home-built SNOM head is based on shear-force detection for control of the tip-sample separation [47]. To detect the shear-force interaction, the tip is glued to a standard quartz tuning fork as shown in Fig. 3.8. While the whole system is being excited mechanically at its resonance frequency by a shaker piezo, the oscillation is monitored by the voltage generated at the electrical contacts of the tuning fork. Lock-in detection is used to determine the tip oscillation amplitude at low signal noise.

The tip-sample separation is controlled by demanding a certain additional damping of the tip amplitude. The sensitivity to the shear-force interaction between tip and sample is limited by the internal damping of the tip-on-tuning-fork system, which is characterized by the quality factor Q. The Q value depends strongly on the mounting of the tip and tuning fork and varies from 100 to 1000. A higher Q value provides better sensitivity, but also means that the system requires more time to adapt the oscillation amplitude to a changed tip-sample interaction.

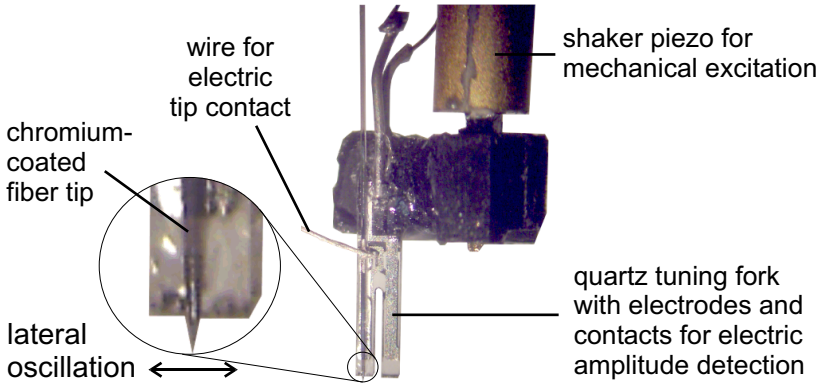

Fig. 3.8 *Assembly for tuning-fork-based shear-force detection. The tip is glued onto one prong of the tuning fork. Electrical contact is made by an additional wire contacted with conductive silver glue. The system is excited mechanically by a shaker piezo and the resulting oscillation amplitude is detected electrically at the contacts of the tuning fork.*

The correlation between selected damping and real tip-sample separation is different for each individual tip. This is not only due to the varying sensitivity, but also due to possible differences in the shear-force interaction itself, which is influenced by the tip shape, for example. Furthermore, as the experiments are carried out under ambient conditions, a water adsorption layer will be present on the surface of the sample and the tip [48, 49]. The thickness of these water layers depends strongly on the wettability of the involved materials, but also on the ambient conditions such as humidity and temperature. When the tip is approached to the sample, a meniscus is formed [50], providing viscous damping of the tip oscillation [51]. The viscosity of the water layer between the tip and the sample changes significantly if the gap gets as small as a few molecular layers [52]. Altogether, the formation of a meniscus, the changing viscosity, as well as direct sample-surface interaction result in a large complexity of the overall shear-force interaction. The absolute values of the tip-sample separation estimated within this work are therefore potentially subject to large errors.

Figure 3.9 shows an approach curve recorded on a barium titanate single-crystal sample. One finds that the shape of the curve depends not only on the ambient conditions, but also on for how much time the tip is kept retracted prior to approach. This might be a consequence of different water coverage and underlines the difficulty of keeping experimental conditions under control.

Nevertheless, estimates for the water layer thickness as well as the tip-sample separation can be deduced from Fig. 3.9. When the tip approaches the sample, the point of initial contact of the tip with the water layer, called “snap-in”, is clearly visible and defines the zero z position. Further approach by more than 10 nm is characterized by only a small decrease in amplitude, which can be attributed to small viscous damping by the water layer. When the tip gets even closer to the sample surface, the damping increases significantly, which might be caused by increased viscosity of the water layer and/or the

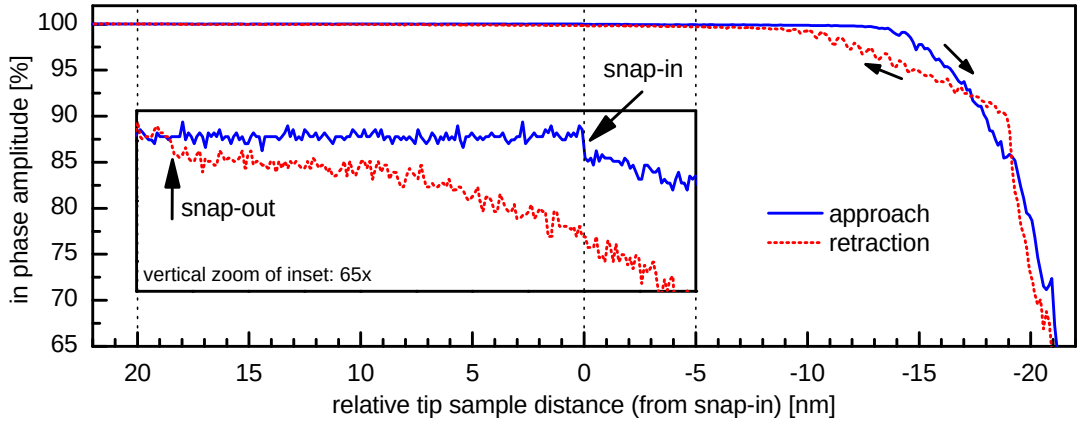

Fig. 3.9 *Tip approach curve recorded on a $BaTiO_3$ sample with a tuning-fork-based shear-force detection system. Approach is characterized by a clear snap-in, marking the initial contact of the tip with the water adsorption layer of the sample, followed by several nanometers of small damping due to viscous damping within the water layer. Further approach leads to a strong increase of the damping, which can be attributed to increased viscosity and/or direct interaction with the sample surface. Retraction is characterized by increased damping in the viscous region and a shifted snap-out, indicating meniscus formation.*

onset of direct interaction with the sample surface [51]. Since these two mechanisms cannot be distinguished in this experiment, the sample surface position can only be estimated. The upper limit is the point of increased interaction, while the lower limit is given by the point where the extrapolated amplitude reaches 0%. For the curve shown in Fig. 3.9, this gives a sample surface position in the range of -15...-25 nm on the present z scale.

For the curve section around the "snap-in" position, the retraction curve is characterized by a stronger damping that the approach curve. Also, the point called "snap-out", characterized by the return of the tip amplitude to its initial value, is located at an almost 20 nm larger tip-sample distance than the "snap-in". This clearly indicates a meniscus being teared apart and illustrates the effect of the wetted surfaces.

3.3.3 AFM stage

The home-built AFM head uses the beam deflection principle to detect the bending of the cantilever. As illustrated in Fig. 3.10, a laser beam is focussed onto the free end of the cantilever and the reflected beam is directed to the center of a four-quadrant photodiode. The bending of the cantilever as well as a buckling lead to a vertical movement of the reflected spot, which is measured as a difference between the top and the bottom channels of the four-quadrant diode. In contrast, a torsion of the cantilever causes a horizontal movement of the spot, which is measured as a difference between the left and the right channels.

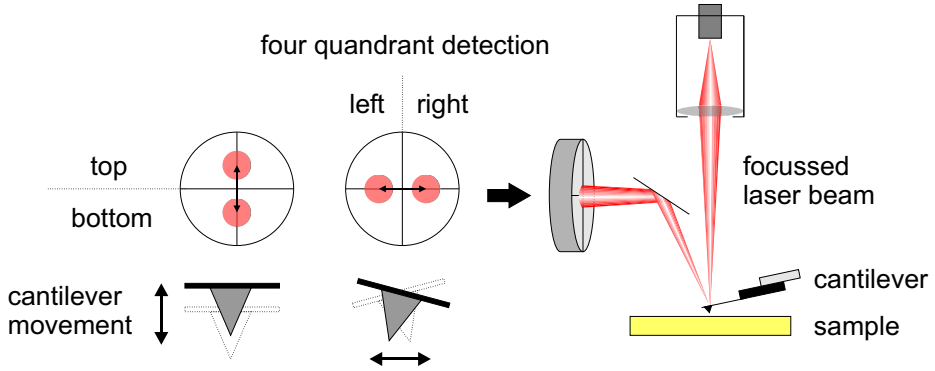

Fig. 3.10 *Basic layout of the AFM head. The AFM is equipped with a beam deflection system that is able to detect vertical and horizontal movement of the cantilever tip end in the "top-bottom" and "left-right" signal channels of the four-quadrant detection system, respectively.*

Within this work, the AFM stage is used for reference measurements utilizing piezoresponse force microscopy (PFM) [53, 54]. This method is able to reveal the three-dimensional distribution of ferroelectric polarization with high resolution by probing the electromechanical properties of the sample. For this, the AFM cantilever is placed in contact with the sample surface as illustrated in Fig. 3.11. A bias voltage applied between the cantilever and the counter-electrode induces a mechanical motion of the sample by the converse piezoelectric effect. Because of the mechanical contact, this motion is transferred to the cantilever and can be measured by the four-quadrant detection system.

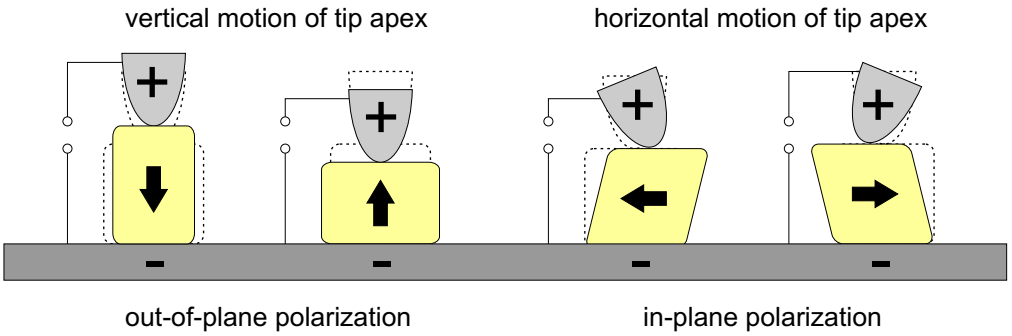

Fig. 3.11 *Operation principle of piezoresponse force microscopy. The sample below the biased tip gets deformed due to the converse piezoelectric effect. This is transferred into a cantilever movement that can be detected by the beam deflection system as illustrated in Fig. 3.10. Figure adapted from [55, 56].*

3.3.4 Laser light sources

In this work, two different monochromatic laser light sources are used. The first one is a helium-neon laser operating at a wavelength of 632.8 nm, which can be combined with a properly aligned electro-optic modulator for optical polarization rotation. If a polarization rotation $\geq 90°$ is required, then the bandwidth limitation of the modulator restricts operating frequencies to the range of 0...100 kHz. The laser source is not only used for focal excitation but also for illumination through optical fiber probes. The second light source used is a laser diode operating at a wavelength of about 650 nm. The emitted light is coupled directly into an optical single-mode fiber. To achieve high coupling ratios of up to 70%, the fiber end has to be positioned very close to the emitting crystal. This became possible after removal of the exit window of the laser diode, by aligning the fiber by means of a standard fiber coupling stage. The advantage of the laser diode is that its output intensity can easily be modulated up to very high frequencies. To achieve this, a simple laser diode driver circuit is equipped with an additional current path, allowing us to modulate the driving current by an external voltage. The circuit provides excellent intensity modulation capabilities, which were verified up to operating frequencies of at least 250 MHz.

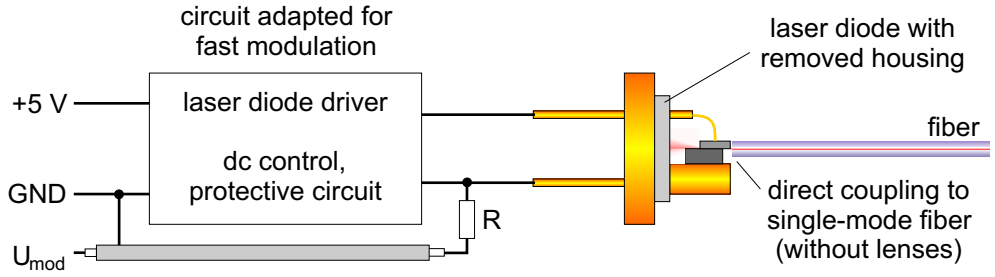

Fig. 3.12 *Principle of home-built fast laser diode modulation and highly efficient fiber coupling. Fast modulation capabilities are added to a standard low-cost dc laser driver circuit by introducing an additional modulation current via the resistor R. Efficient coupling into a single-mode fiber is achieved by removal of the window part of the housing and direct adjustment of the fiber in front of the emitting laser crystal. This way, coupling ratios of up to 70% can be achieved.*

3.3.5 Optical detectors

The selection of the proper detection system is essential for the measurement of small effects such as the electro-optic effect. One has to meet several competing requirements. Statistical noise defines the absolute minimum of detected light power required for such a measurement. But there is also an upper limit to the light power given by the capabilities of the optical probe or by the necessity of avoiding photoinduced side effects. Therefore the challenge is to use as small light power as possible but as much as needed to beat the noise.

Very low light levels can easily be detected by single-photon-counting modules (SPCM). Such devices are based on avalanche photodiodes operated at break-down conditions. Due to the limitation of the maximum possible count rate in the order of 10^6 counts per second, the relative sensitivity is limited by statistical noise to 10^{-3} for a measurement period of 1 second. A higher sensitivity can only be achieved by an increase of the integration time, which is not suitable for scanning probe imaging.

Therefore, the detectors used are based on sensitive photodiodes combined with a single stage of high amplification to keep additional electronic noise as small as possible. Since gain competes with bandwidth, a low-noise operational amplifier with a high gain-bandwidth product and low input bias currents (OPA657, Texas Instruments) is used to achieve high amplification at the required bandwidth.

Two different detector modules were built to match the capabilities of the probes used (Fig. 3.13). The first one is based on a silicon PIN photodiode and operates at a maximum light power of 1 µW with a constant gain up to frequencies of 100 kHz. The second one uses a silicon avalanche photodiode and an amplification stage set up for higher gain. The maximum operating light power can be selected via the gain of the avalanche photodiode in the range of 1..50 nW. This detector shows constant gain for frequencies of up to 30 kHz.

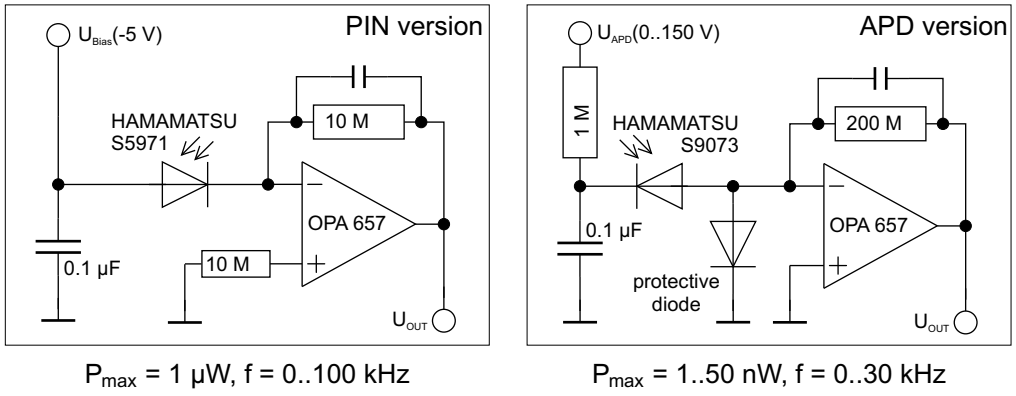

Fig. 3.13 *Circuits of the used PIN and APD detector versions. The PIN version has a fixed sensitivity of about 4V/µW, while the sensitivity of the APD detector is selectable in the range of 0.04...4 V/nW by adjusting the reverse bias voltage U_{APD}.*

.

Chapter 4

Electro-optic domain imaging

First, this chapter introduces the electro-optic effect of differently oriented ferroelectric domains on the basis of a simple model. This is followed by the description of the applied experimental approach. The main part of this chapter presents the results of the measurements, obtained with different probe types and in different frequency regimes.

4.1 Electro-optic effect

There are materials that change their optical properties, in particular their refractive index, under the influence of an external electric field. This electro-optic effect depends strongly on the material class and can be linear, quadratic or even of higher order in terms of the applied electric field. Especially the occurrence of odd-order effects such as the linear electro-optic effect is determined by the crystal symmetry. Since ferroelectric crystals are expected to show a large linear electro-optic effect as stated in Sec. 2.4, this effect can be used to break the optical symmetry between antiparallel domains.

For the illustration of this approach, let us consider a crystal with the symmetry point group $4mm$ (e.g. barium titanate at room temperature) that is illuminated by a plane optical wave and is subject to a homogenous external electric field. The applied electric field $\vec{E}$ changes the inverse dielectric tensor $\boldsymbol{\eta}$ due to the electro-optic effect according to [24]

$$\Delta\eta_{ij} = \Delta\varepsilon_{ij}^{-1} = \left(r_{ijk}^{S} + p_{ijmn}^{E} d_{kmn}\right) E_k = r_{ijk}^{T} E_k \,. \tag{4.1}$$

The effect arises from a pure electro-optical contribution, described by the strain-free ("clamped") electro-optic tensor $\boldsymbol{r}^S$, together with an elasto-optic contribution, described by the piezoelectric coefficients d_{kmn} and the elasto-optic tensor $\boldsymbol{p}^E$. Both effects are combined into the stress free ("unclamped") electro-optic tensor $\boldsymbol{r}^T$. Depending on conditions such as mechanical constraints or time dependence of the applied electric field, different magnitudes of the elasto-optic contribution can be expected. For this reason, we describe the electro-optic effect in the more general terms of an effective electro-optic tensor $\boldsymbol{r}^{\text{eff}}$.

The influence of the external electric field can be described as a deformation of the refractive-index ellipsoid as illustrated in Fig. 4.1. The change of the ellipsoid depends on the domain orientation with respect to the applied field.

If we assume a normal mode of optical polarization (purely ordinary or purely extraordinary), the refractive index can be expressed by [57]

$$n(\vec{u}) = (\eta_{ij} u_i u_j)^{-1/2}\,, \tag{4.2}$$

where $\vec{u}$ is the unit vector along the polarization direction of the light beam. This vector $\vec{u}$ determines which point of the refractive-index ellipsoid is probed and which elements of the inverse epsilon tensor $\boldsymbol{\eta}$ are tested in the experiment.

In our experiments, the illumination and the applied electric field are aligned perpendicular to the sample surface approximately. To describe the sample properties, we use the crystal coordinates, with the ferroelectric polarization pointing along $\vec{e}_3$, which defines the c axis of the crystal as illustrated in Fig. 4.1.

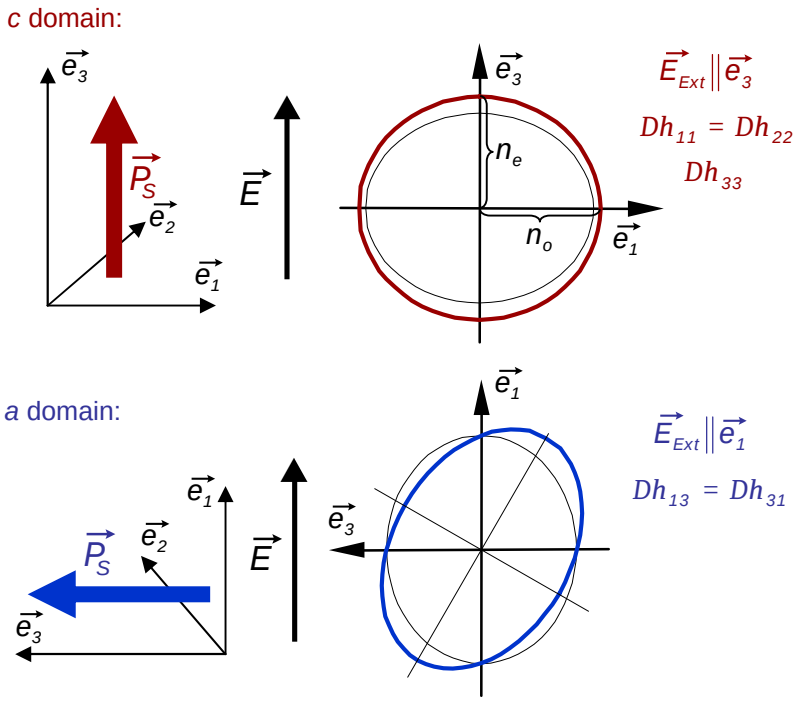

Fig. 4.1 *Change of the refractive-index ellipsoid due to an external electric field for a crystal with 4mm symmetry. In case of a c domain configuration only the diagonal elements η_{11}, η_{22}, and η_{33} are changed. This leads to a "breathing" of the refractive-index ellipsoid at a fixed orientation. In case of an a domain, only the non-diagonal elements η_{13} and η_{31} are changed. This leads to a tilting and "breathing" of the refractive-index ellipsoid in the $\vec{e}_1\vec{e}_3$ plane. The extension along $\vec{e}_2$ is thereby left unchanged.*

For the c domain configuration illustrated at the top of Fig. 4.1, $\vec{e}_3$ is normal to the sample surface. An electric field applied along $\vec{e}_3$ changes all diagonal elements of $\boldsymbol{\eta}$, but does not create any off-diagonal elements [58]. The two independent optical polarization orientations along $\vec{e}_1$ and $\vec{e}_2$ probe the change of $\eta_{11} = \eta_{22} = 1/n_a^2$, and experience therefore the same modified refractive index given by

$$n_1 = n_2 = \frac{n_o}{\sqrt{1 + n_o^2\, r_{113}^{\text{eff}} E_3}}, \tag{4.3}$$

where n_o denotes the ordinary refractive index of the birefringent crystal at zero electric field.

The refractive index for a reversed orientation of ferroelectric polarization can be described by changing the sign of E_3 in Eq. 4.3 (Appendix A.1), leading to the desired difference of refractive index between antiparallel c domains.

In case of an a domain configuration, which is illustrated at the bottom of Fig. 4.1, the surface normal as well as the applied electric field point along $\vec{e}_1$. The electric field $\vec{E} = E_1\vec{e}_1$ leaves the diagonal elements of $\boldsymbol{\eta}$ unaffected while creating off-diagonal elements η_{13} and η_{31}. Since illumination exactly along $\vec{e}_1$ can probe only the components η_{22} and η_{33}, no optical contrast would arise unless the illumination becomes slightly off-axis by an angle ϕ in the $\vec{e}_1\vec{e}_3$ plane. Only then, the elements η_{13} and η_{31} become trackable. Light polarized in the $\vec{e}_1\vec{e}_3$ plane is subject to a refractive index given by:

$$n(E_1) = \left(\frac{\sin^2\phi}{n_o^2} + \frac{\cos^2\phi}{n_e^2} + 2 r_{131}^{\text{eff}} E_1 \sin\phi\cos\phi \right)^{-1/2}, \tag{4.4}$$

with n_e the extraordinary refractive index of the birefringent crystal at zero electric field. Light polarized along $\vec{e}_2$, however, is unaffected by E_1 leading to an additional polarization dependence. A reversed ferroelectric polarization $\vec{P}$ under constant illumination and field geometry can be described by altering the sign of E_1 in Eq. 4.4. Hence, antiparallel domains again are characterized by a difference of refractive index.

4.2 Experimental approach

The approach taken for the local-scale measurement of the electro-optic effect is based on near-field scanning optical microscopy. This method is extended by the simultaneous application of localized external electric fields by means of electrically conductive optical tips. This allows us to probe the electro-optic effect in a confined sample volume. Similar approaches to local-scale electro-optic measurements make use of confocal illumination and detection in combination with macroscopic [59, 60] or nanoscopic [61] electrodes. In contrast to this, we combine the application of the electric field with optical illumination by the same tip.

The main reason for the use of such tips is the improved confinement of the probed sample volume for increased resolution. In the case of electro-optic response, this can be achieved by confining the light or the external electric field as illustrated in Fig. 4.2.

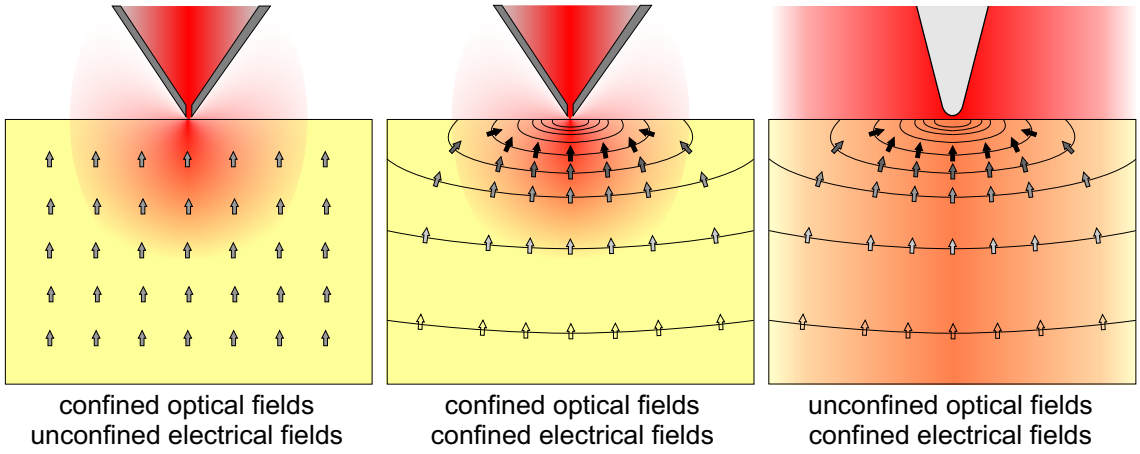

Fig. 4.2 *Three options to confine the probed volume for resolution enhancement in electro-optic-response measurements. Either confinement of the optical fields (left), confinement of the probing electric fields (right), or the combination of both (center) can be used to achieve confinement of the probed volume.*

The purely optical confinement can be improved by limiting the optically inspected sample volume by an aperture, like it is typically done in SNOM applications. In this case, there is no need for the confinement of the electric field as shown on the left side of Fig. 4.2. Alternatively, the use of a sharp tip as an electrode confines the applied electric field as shown on the right side of Fig. 4.2. Because of the geometry, the electric field strength very close to the tip apex is enhanced and a good confinement of the probed volume can be achieved without confinement of the optical field. In general, we can use a mixture of both confinement mechanisms as illustrated in the center of Fig. 4.2 for a conductive aperture probe.

For detection of the change of the refractive index induced by the applied electric field, there are primarily three options: the effect on the transmitted or reflected light intensity and the effect on the phase of light wave travelling through the sample. Since it can be complicated to ensure enough stability of the optical path in SNOM experiments, we focus in this work on the first two options only. The values of transmitted and reflected light intensity are changed at refractive-index jumps typically, limiting the sensitivity to regions with significant index change. This indicates top-surface sensitivity for our experimental approach, since the electric probing field applied by the tip is localized very close to the sample surface. The description in terms of a pure surface effect will be further discussed in Sec. 6.3.1.

The experiments are implemented on the Axiovert 135 TV inverted optical microscope in combination with the SNOM stage as described in Sec. 3.3.1. The sample is mounted on the xyz scanner of the microscope by attaching it to a glass slide, which is covered with an ultrathin but still transparent chromium layer forming an electrode. This way, not only mounting but also a counter electrode for the application of electric fields is

provided, while the sample itself can be kept free of electrode material. Visual inspection in combination with polarized-light microscopy allows the adjustment of the sample position and orientation with respect to the preadjusted optical probe. This includes also the correct alignment of the optical polarization with respect to the domain orientation.

For obtaining optical information, the light emitted from the tip is transmitted through the sample and collected with the microscope objective (Achrostigmat 40×/0.65) as illustrated in Fig. 4.3. The light power is detected by a home-built photodetector (Sec. 3.3.5). For probing the electro-optic effect, a voltage is applied between the conductive tip and the counter-electrode. The electro-optic response changes the transmitted light intensity due to the local change of the refractive index at the sample surface. For increased sensitivity and to suppress noise and drift, the applied voltage is sinusoidally modulated, leading to a modulation of the detected light intensity, which is demodulated by a phase-sensitive lock-in amplifier.

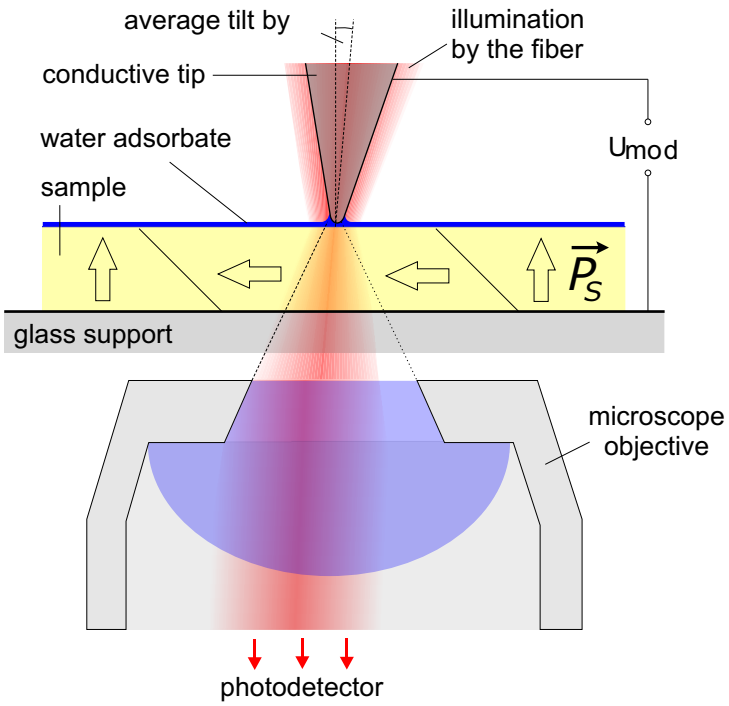

Fig. 4.3 *Basic setup used for electro-optic response measurements. The sample is attached to a chromium-coated glass slide, which forms the counter electrode for the application of electric fields by the conductive tip. The inspected spot on the sample is illuminated by the fiber tip, and the power of the transmitted light, collected by the microscope objective, is detected by a photodetector. The water adsorption layer allows proper operation of the shear-force distance control and provides a better matching of the dielectric constant inside the gap between tip and sample. An average tilt of the optical tip is introduced to obtain an effective electro-optic-response signal for a domains.*

Since the experiment is run under ambient conditions, the sample is typically covered with a water adsorption layer, which because of the polar nature of ferroelectric samples can be rather thick. However, this layer allows not only proper noncontact operation of the shear-force distance control (Sec. 3.3.2), but also provides a better matching of the dielectric constants in the gap and in the sample, which increases the applied electric field inside the sample (Sec. 6.2.4).

4.3 Experimental results

Within this work the obtained results for the local-scale probing of the electro-optic effect are presented in terms of the "normalized electro-optic response" signal s. This value corresponds to the relative change of transmitted light power P_t with respect to the applied voltage U between tip and counter electrode and is given by

$$s = s_t = \frac{P_t - P_{t|E=0}}{P_{t|E=0}} \frac{1}{U} \,. \tag{4.5}$$

The optionally presented intensity and topography information corresponds to the dc part of the optical detector signal and the output of the distance control feedback loop, respectively.

4.3.1 Electro-optic domain imaging using an etched fiber tip

The etched fiber tips do not provide any additional aperture at the tip apex (Sec. 3.2.2). Therefore, the radiated light is rather unconfined and provides poor lateral resolution. According to the right-hand side of Fig. 4.2, spatial confinement for the measurement of local electro-optic properties in this case is provided mainly by the localized distribution of the probing electric field.

First preliminary electro-optic domain imaging of reasonable quality was achieved with a less sensitive detector and therefore at a higher detected light power of about 8 µW. The modulation voltage was set to $U_{\mathrm{mod}} = 5.8\ \mathrm{V_{pp}}$ at a frequency $f = 10.7$ kHz, far above the bandwidth of the tip-sample distance control loop, but within the bandwidth of the detector.

Figure 4.4 shows the measured electro-optically induced contrast between different domain orientations. Not only a and c domains but also antiparallel a and antiparallel c domains can be clearly distinguished. The difference in transmitted light power between antiparallel c domains measures ∼30 pW. The two-dimensional domain distribution observed here is in excellent agreement with piezoresponse force measurements performed at the same sample position as shown in Fig. 4.5. This is a proof that Fig. 4.4 indeed reveals a true map of ferroelectric domains and domain walls at the sample surface.

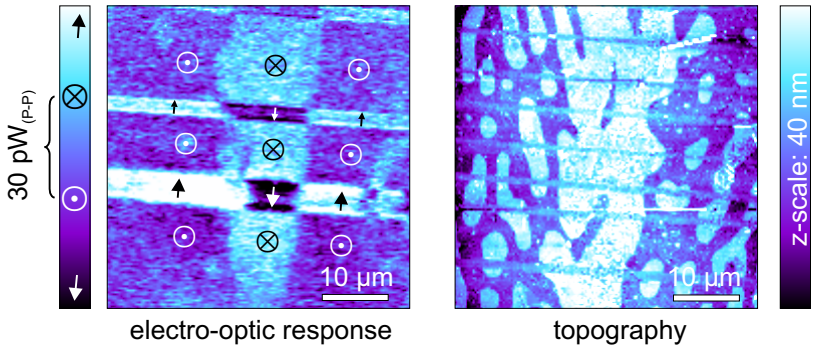

Fig. 4.4 *Electro-optic response obtained by an etched fiber tip. The naturally grown domain pattern of a $BaTiO_3$ single crystal was imaged by recording the local electro-optic response. Not only a and c domain orientation, but also antiparallel a and antiparallel c domains are distinguished as indicated by the arrows showing the direction of polarization. There is no systematic cross-talk with the sample topography shown on the right-hand side.*

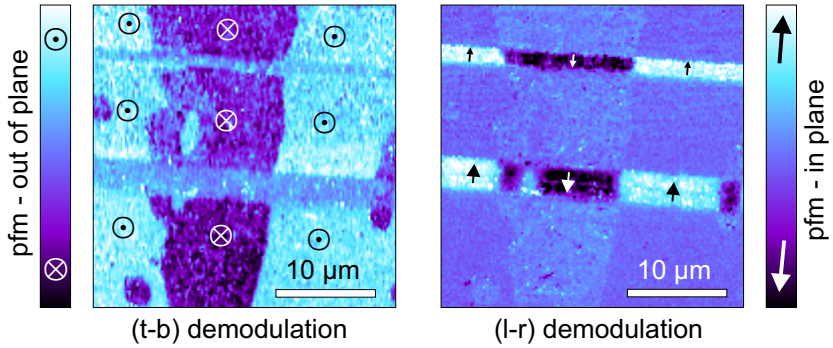

Fig. 4.5 *Ferroelectric domain pattern obtained by piezoresponse force microscopy. The demodulation of the (t-b) channel corresponds to the out-of-plane polarization, while the (l-r) channel corresponds to the in-plane polarization. The domain pattern is in good agreement with the one obtained from the electro-optic response (Fig. 4.4).*

Additionally, Fig. 4.6 illustrates the dependence of the electro-optic signal on the optical polarization. As mentioned in conjunction with Eq. 4.2, the contrast between antiparallel *a* domains is expected to vanish if the polarization is chosen along $\vec{e}_2$, i.e., for a perpendicular alignment of ferroelectric and optical polarizations. This is indeed confirmed by the results shown in Fig. 4.6. Orthogonal *a* domains thus are directly deducible in our experiment by simply rotating the optical polarization [62]. Hence, the full 3-dimensional polarization distribution can be obtained.

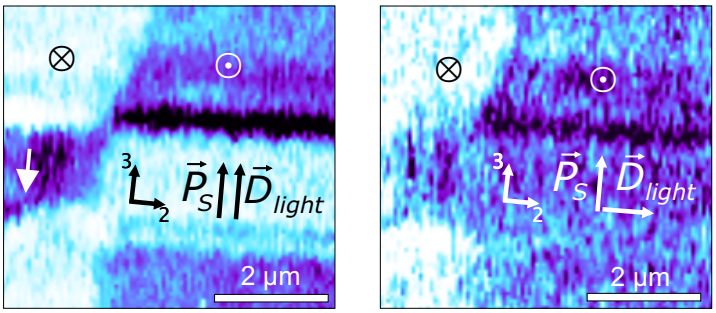

Fig. 4.6 *Dependence of the electro-optic response on the polarization orientation of the optical field. For a domain areas an effective electro-optic response signal can be obtained, if the optical polarization $\vec{D}_{light}$ is aligned parallel to the ferroelectric polarization $\vec{P}_S$ (left). This signal vanishes for perpendicular alignment of $\vec{D}_{light}$ and $\vec{P}_S$ (right). The electro-optic response of c domain areas is present for both cases.*

For etched fiber tips, the lateral resolution of the electro-optic response is determined by the confinement of the probing electric field rather than the confinement of the optical field. Since the distribution of the probing electric field within the anisotropic sample is different for the various domain orientations (Sec. 6.2.3), the achievable resolution may vary for different domain transition types. Line profiles of the electro-optic response across these transitions are shown in Fig. 4.7. From them, a lateral resolution of 250 nm can be deduced for *a*-*a* and *a*-*c* transitions, while a somewhat lower resolution of 370 nm is found for *c*-*c* transitions. Altogether, the lateral resolution of the electro-optic response is significantly better than the purely optical resolution, which is given by the optical spot size of typically 1 µm.

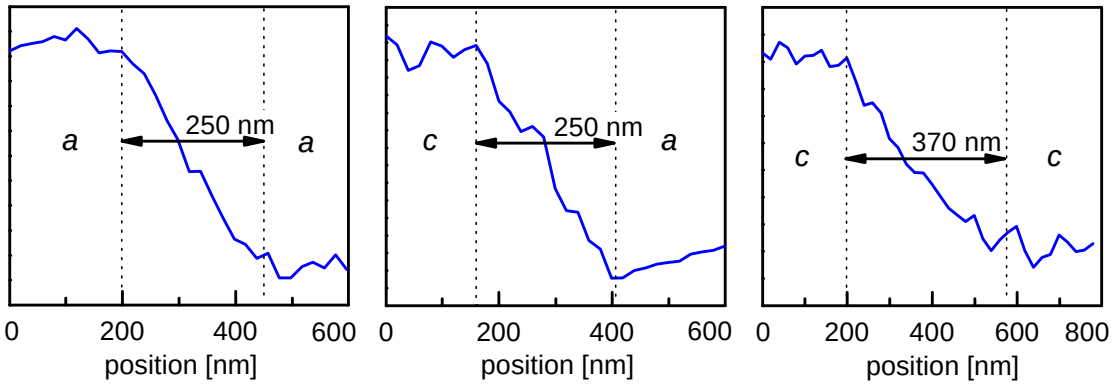

Fig. 4.7 *Spatial resolution of electro-optic imaging as obtained with an etched fiber tip. The achievable resolution varies with the domain type due to different distributions of the probing electric field within the anisotropic sample. The confinement of this field improves the resolution to 250 nm for a-a and a-c transitions and to 370 nm for c-c transitions, which is better than the purely optical resolution given by the spot size of about 1 µm.*

Some first experiments, operating with a light power above 10 µW, revealed a limited stability of the imaged domain pattern in some rare cases. Since effects of optical absorption and concomitant local heating cannot be excluded in principle, it is advisable to decrease the power. As operation at lower light intensities leads to a loss of signal-to-noise ratio, very sensitive detection close to the statistical noise limit is required. Later on, the detector was modified to provide sufficient sensitivity at the highest possible bandwidth (Sec. 3.3.5). Figure 4.8 shows the result of an electro-optic response measurement performed with a light power of 0.3 µW, and at a modulation frequency of the probing electric field of 102 kHz, which is the frequency limit of the the lock-in amplifier in use (SR 830). Even under these more difficult conditions, all domain orientations can be deduced with sufficient S/N ratio. The additionally recorded signal channels reveal a correlation only between the topography and the dc intensity, while there is no general correlation with the ac electro-optic response.

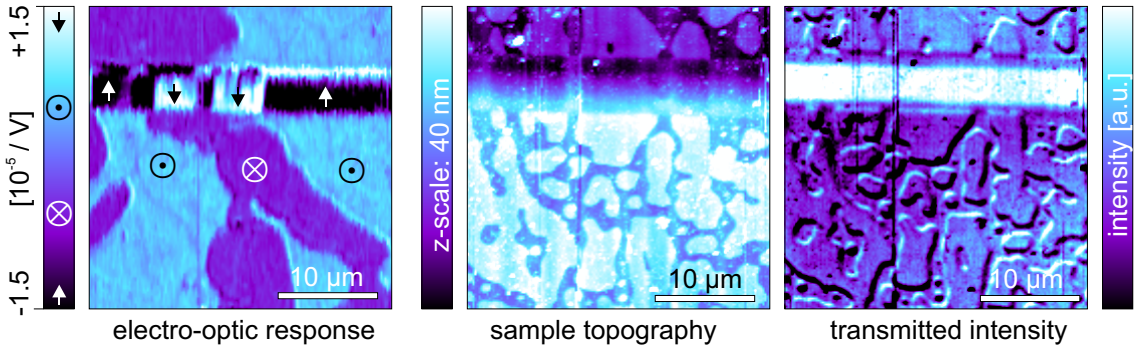

Fig. 4.8 *Electro-optic response measurement at decreased light power and increased frequency. The reduction of the light power is advisable to suppress possible effects of absorption and local heating on the stability of the domain pattern. The measurement is carried out at a light power of 0.3 µW and a frequency of the probing field of 102 kHz. Again, there is no crosstalk between the topography and the electro-optic response signal. Only the additionally recorded dc power reveals significant correlation with topography.*

4.3.2 Electro-optic domain imaging using an aperture tip

With this type of probe, the probed volume is mainly determined by the confinement of the light, while the confinement of the probing electric field is less pronounced. As a consequence of the geometry of the tip electrode, it is also expected that the probing field is lower at the center of the aperture than at its border, because the electrode is missing within the aperture. The border regions may contribute strongly to the effective electro-optic response and this might decrease the resolution.

It is obvious that one has to use very small apertures to achieve high resolution. But since transmittance is very low for small apertures, one has to make a trade-off between

resolution and light power. Compared to etched fiber tips, a further improvement of the detection sensitivity is needed. This is achieved by combining higher amplification of the detector circuit with the built-in amplification of an avalanche photodiode as described for the APD detector version in Sec. 3.3.5.

First measurements with aperture probes were done with pulled fiber tips manufactured by Nanonics (Sec. 3.2.3). Since these tips show a very low transmittance, the tips with the highest output power were chosen at the expense of a possibly larger aperture and, hence, less optical confinement. Attempts to detect an electro-optic response signal failed first, probably because of low electrical conductivity of the tip end. Only after the deposition of an additional thin chromium layer, was it possible to detect an electro-optic response signal again. Figure 4.9 shows the image of a *c* domain area of the $BaTiO_3$ crystal, intersected by a stripe-like *a* domain. The image quality is quite low because of the bad S/N ratio resulting from the very low light power of 0.16 nW. The averaged profile of the *a*-*c* transition gives a poor resolution of only about 500 nm, much worse than expected from the nominal aperture diameter of about 100 nm.

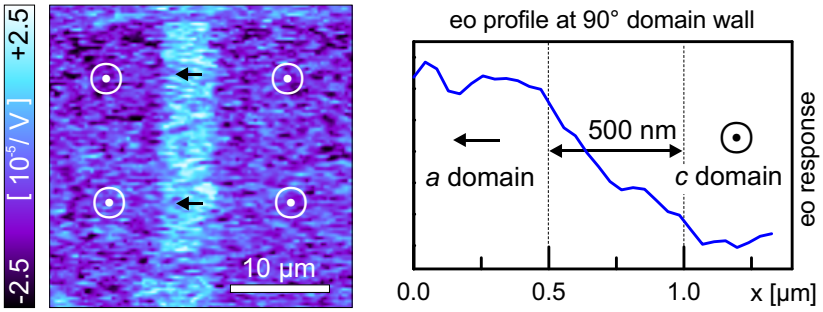

Fig. 4.9 *Electro-optic response measured by a Nanonics aperture fiber probe, additionally coated with a thin chromium layer to improve conductivity. The bad S/N ratio is a result of the very low light power of 0.16 nW. Compared to the nominal aperture diameter of 100 nm, only a poor resolution of 500 nm is found.*

Better performance was achieved with the adapted cantilever SNOM probes. These tips provide good conductivity and much higher transmittance. Figure 4.10 shows one of the first domain images obtained with these tips at a light power of 25 nW, showing not only sufficient S/N ratio, but also high resolution of about 200 nm for the separation of antiparallel *c* domains.

Not only in the measurements shown, but also in all subsequent measurements with aperture tips, any clear contrast between antiparallel *a* domains is missing, independently of the occasional tilt of the tip axis. This is in contradiction to the measurements with simple tips without aperture (Figs. 4.4, 4.8). The important difference, beside the effective spot size, is the directional distribution of the emitted light. The lateral confinement of an optical field is connected to a minimum width of the directional distribution, which is fundamentally given by the uncertainty principle of position in space and momentum. Since the confinement by the aperture is quite strong, light emission into a large solid angle is

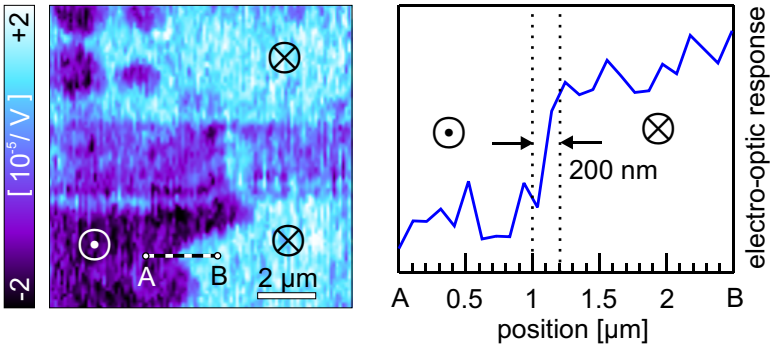

Fig. 4.10 *Electro-optic response measured by an adapted SNOM cantilever probe at a light power of 25 nW. High resolution of about 200 nm for transitions between antiparallel c domains is observed. Any clear contrast between antiparallel a domains is missing.*

expected. In contrast, the light accepted for detection is limited to a cone characterized by the effective numerical aperture of the setup. Therefore, only a part of the emitted light from aperture tips is collected for detection. This part is almost independent of a small average tilt of the tip axis and therefore there is no clear contrast between antiparallel *a* domain areas.

To obtain a significant contrast between antiparallel *a* domains, there are two options. The first one is to tilt the sample with respect to the optical axis, but this is limited by the available z range of the scanner, which has to compensate the introduced tilt during scanning. The second option is to block a part of the collected light as illustrated on the left side of Fig. 4.11. This way, the symmetry of the directional distribution can easily be broken and a clear contrast between antiparallel *a* domains can again be obtained as shown on the right side of Fig. 4.11. This contrast will be essential for the localization of 180° domain walls within in-plane-polarized regions studied in Sec. 7.4.

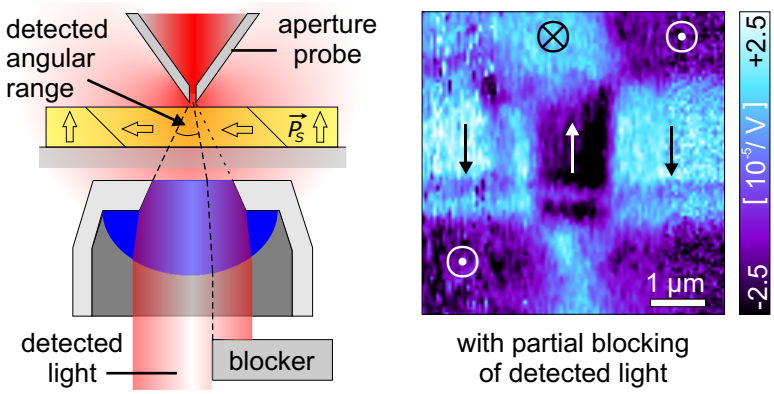

Fig. 4.11 *Electro-optic response measured by an adapted SNOM cantilever. To obtain an effective a domain signal, the angular distribution of the collected light was made asymmetric with respect to the surface normal by blocking a part of the detection beam. This restores the contrast between antiparallel a domains as shown in the right image.*

4.3.3 Electro-optic response at high frequencies

Realizing optical devices with active functionality for the use in high-speed communication systems or for fast information processing requires operation with high bandwidth. Limitations are not only due to the frequency response of the chosen material structure. A problem stems also from the external circuitry, since it may have to drive quite a large capacitance at high frequencies. This capacitance can be either parasitic, for example caused by the wiring, or intrinsic, stemming from the functional device itself. In case of barium titanate this is a severe problem due to its high dielectric constant. Nevertheless, high-speed electro-optic waveguide modulators operating at up to 40 GHz have been demonstrated with barium titanate thin films on a magnesium oxide substrate so far [63].

Since a growing number of applications are based on a functional ferroelectric material with a specific artificial domain pattern, it gets interesting to study such domain structures locally also at high frequencies. Therefore, the experiment was modified to demonstrate electro-optic response at high frequencies. The setup is limited in frequency range by the capabilities of the available equipment and by the influence of wiring and series resistances in combination with the tip-sample and stray capacitance.

The detectors (Sec. 3.3.5) used in the present experiments were designed for high sensitivity and therefore they are limited to small bandwidth. To extend the detection of the electro-optic response to frequencies much higher than the detector bandwidth, frequency mixing is utilized. The principle works as follows: If two signal modulations with different frequencies are linked by a multiplication operation, the result contains not only terms varying with the input frequencies but also terms varying with the difference and the sum of the input frequencies. By this, it gets possible to detect high-frequency effects at much lower frequencies. To achieve this, one needs of course a second source of high-frequency modulation. In the present experiments this is achieved by modulating the intensity of the laser light source as described in Sec. 3.3.4. In the absence of the sample, this leads to a light intensity I_{Src} described by

$$I_{Src} = I_0 \cdot \left(1 + A_{Src} \sin\left(\omega_{Src}\, t\right)\right) . \tag{4.6}$$

It is oscillating at the frequency ω_{Src} with a relative amplitude A_{Src} around its average value I_0. A value of $A_{Src} = 1$ corresponds to 100% modulation, i.e. an oscillation between zero and $2I_0$. If now the sample is inserted, the detected intensity will be lowered by a factor T_{EO} (Eq. 4.7). This value corresponds to the transmission coefficient of the sample. It incorporates also the electro-optic response with a relative amplitude of A_{EO} at its modulation frequency ω_{EO}:

$$T_{EO} = T_0 \cdot \left(1 + A_{EO} \sin\left(\omega_{EO}\, t\right)\right) \tag{4.7}$$

The final intensity I_{Out} is described by

$$\begin{aligned} I_{Out} &= I_{Src} \cdot T_{EO} \\ &= I_0 T_0 \Big(1 + A_{Src} \sin(\omega_{Src}\, t) + A_{EO} \sin(\omega_{EO}\, t) \\ &\qquad + A_{Src} A_{EO} \sin(\omega_{Src}\, t) \sin(\omega_{EO}\, t) \Big) . \end{aligned} \tag{4.8}$$

This expression can be rearranged to

$$\begin{aligned} I_{Out} = \quad & I_0 T_0 \\ & + I_0 T_0 \cdot \left(A_{Src} \sin(\omega_{Src}\, t) + A_{EO} \sin(\omega_{EO}\, t) \right) \\ & + I_0 T_0 \cdot \frac{A_{Src} A_{EO}}{2} \Big(\cos\big((\omega_{Src} - \omega_{EO})\, t\big) - \cos\big((\omega_{Src} + \omega_{EO})\, t\big) \Big) . \end{aligned} \tag{4.9}$$

The first line of the right-hand side of Eq. (4.9) corresponds to the average detected intensity, while the second line contains components oscillating at the input frequencies ω_{Src} and ω_{EO}. The third line represents the contribution of the sum and difference frequencies we are interested in. The prefactors of these terms indicate the price we have to pay for the extended frequency range, namely a lowering of the detected signal amplitude by a factor $A_{Src}/2$. For a fully modulated light source A_{Src} equals 1, leading to a signal amplitude of 50% compared to direct demodulation of the electro-optic response. This is, of course, a critical point concerning effective S/N ratio. Figure 4.12 shows the results of high-frequency electro-optic-response measurements for different probe types. It is found that the signal sits on a relatively large frequency-dependent offset, which can obscure the true electro-optic response. For the electro-optic response measurements to provide satisfactory domain imaging, they must therefore be performed in those specific frequency ranges that show only minor offsets.

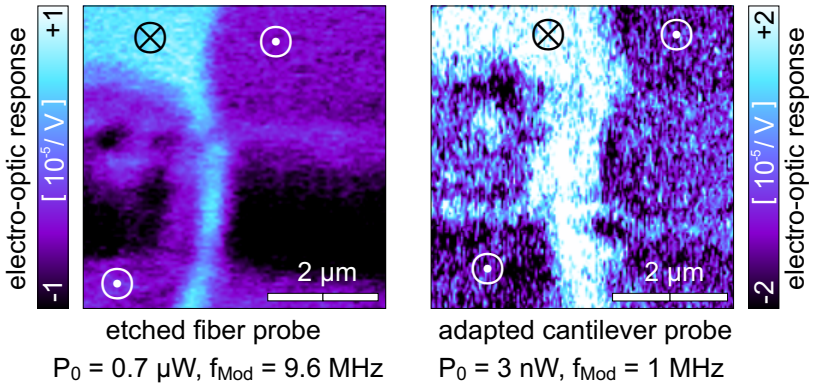

Fig. 4.12 *Electro-optic response at high frequencies. The bandwidth limitation of the detection is overcome by frequency down-mixing based on a modulated laser light source. The values of the normalized electro-optic response are almost the same as for lower frequencies, while the S/N ratio is lower.*

4.3.4 Imaging artifacts

Optical information obtained by SNOM measurements is typically subject to strong topography artifacts [64]. This is found not to be the case for the electro-optic-response measurements. Here, the sample topography affects mainly the dc value of the transmitted light power (Fig. 4.8). To first order, the electro-optic response, which is obtained by a modulation technique, remains unaffected by this.

But electro-optic domain imaging is subject to a different type of artifacts. Especially *a-c* domain boundaries are often found to appear "decorated" in the electro-optic response signal (Figs. 4.6, 4.8, 4.13). Depending on the particular tip used, this effect may be either quite pronounced or almost negligible. Therefore, it can be assumed that the tip properties play an important role for this type of artifact. While special tip properties alter the obtained electro-optic response uniformly across single-domain areas, their influence reveals itself at domain boundaries. There, for instance asymmetries of the tip in combination with the extraordinary electric-field distribution can enhance the electro-optic response significantly.

Figure 4.13 shows in detail the characteristic of an *a-c* domain wall as measured with two different tips and at different sample positions. It is remarkable that only one side of the *a* domain stripes seems to be affected, showing a rim in which the sign of the signal is opposite to that inside the *a* domain. A similar effect at the other boundary may be hidden by the dominating *a* domain signal because of less magnitude and possibly different sign.

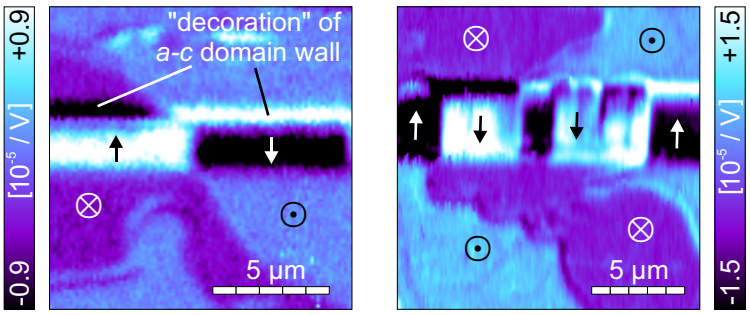

Fig. 4.13 *Artifacts in electro-optic response measurement. A decoration of the a-c domain boundary is found very often, showing large electro-optic response of opposite sign as compared with the a domain signal.*

4.4 Conclusions

The presented local-scale measurement of the electro-optic effect is capable of distinguishing all domain orientations clearly. It allows us to address different electro-optic coefficients of the sample via the polarization of the light and the average tilt of the optical axis. This optical method is found to be suitable for domain imaging, and the observed domain distributions are confirmed by results obtained by piezoresponse force microscopy at the same sample position.

In contrast to typical SNOM methods, the information obtained from the electro-optic response is almost free of topography artifacts. The individual tip properties such as the geometrical shape, conductivity, and optical output are reflected by the absolute values of the electro-optic response and by the resolution, as well as the imaging characteristics at domain boundaries. There, we can find imaging artifacts that vary from tip to tip. Experiments performed with different types of optical probe, both without and with aperture, not only provide further control of the resolution, but also reveal what influence the confinement of the optical as well as the electric probing fields has.

In comparison to PFM, another advantage of the presented optical method is that the ferroelectric domain structure can be inspected even at high frequencies of the applied electric field. In combination with a modulated light source, electro-optic domain imaging of good quality could be achieved for frequencies up to at least 10 MHz. At higher frequencies, the imaging quality deteriorates because of frequency-dependent offsets of the detector signal as well as the growing influence of stray and sample capacitance in combination with the series resistance of the conductive tip.

The main problem of the electro-optic-response method is the limited availability of tips with sufficient optical quality and good electrical conductivity. With improved probes, the resolution as well as the S/N ratio could be enhanced significantly. An ideal probe should provide a conductive structure of small size (a very sharp tip for instance) for the confinement of the applied electric field, as well as a confinement of the optical field at reasonable light intensities.

The interpretation and understanding of the experimental results, as obtained with the present tips, gets substantial support from numerical modelling of the electric-field distribution and the related electro-optic response, as will be reported in detail in chapter 6.

Chapter 5

Electro-optic measurement of ferroelectric hysteresis

After a short introduction to ferroelectric hysteresis, an overview of the commonly used methods for its measurement is given. The main part of this chapter is focussed on the hysteresis measurement by electro-optic response. Experimental results are presented for a sequence of different tip-sample separations which reveal the distance dependence. Reference measurements with different probe types and probing methods back up the significance of the experiments.

5.1 Introduction

The switching of the spontaneous polarization between different states of orientation under the influence of external electric fields is crucial for ferroelectric materials. It is characterized by a hysteresis loop in terms of the spontaneous polarization or a connected quantity as a function of the electric field. From the hysteresis curve, not only the switchable polarization and coercive fields, but also the effect of imprint and fatigue can be deduced as illustrated in Fig. 5.1. Imprint is a shift of the hysteresis curve due to built-in fields and partially unswitchable polarization. Fatigue is an effect of aging, which reduces the value of the spontaneous polarization if the switching field is cycled a large number of times.

The obtained parameters not only characterize the performance of a ferroelectric material, but also reveal the conditions needed for artificial domain orientation and domain engineering. The general trend towards device miniaturization requires characterization at small length scales and investigations of size-dependent effects, since it is expected that there is a fundamental size limit for the occurrence of ferroelectricity [65].

The classical method of hysteresis measurement is based on the monitoring of the switching current [8, 66]. The fact that the switching current is proportional to the switched sample area, makes this method unpracticable for very small structures due to small switching currents. Nevertheless, electric hysteresis measurements have been reported for free-standing structures with an area down to 0.04 μm^2 contacted by an AFM cantilever [67, 68].

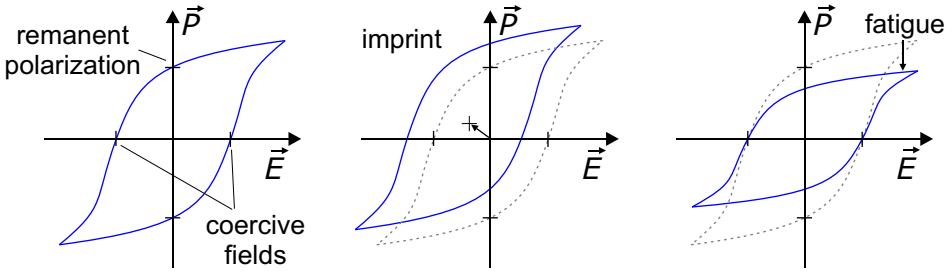

Fig. 5.1 *Parameters and effects obtainable from hysteresis curves [14]. Remanent polarization as well as coercive fields can be directly deduced from hysteresis curves. Imprint indicates the presence of additional internal fields and/or contributions of unswitchable parts of the polarization. Fatigue is a process of aging and leads to a decrease of remanent polarization after a large number of switching cycles.*

A popular method for hysteresis measurement at the nanometer scale is based on piezoresponse force microscopy for polarization monitoring [69, 70, 71]. With this method, ferroelectric switching has been demonstrated in structures down to 20 nm in lateral size [72]. However, it should be kept in mind that mechanical stress, applied by the cantilever, may alter the switching behavior due to ferroelastic effects [73].

Since AFM instrumentation is not limited to switching experiments at single points, it is also used for the fabrication of nanoscale domain structures [74, 75]. Detailed investigations on the switching mechanism have revealed significant differences in domain nucleation at macroscopic and nanoscopic scales. While macroscopic domain nucleation occurs at lower electric fields due to domain nucleation at defects and residual domains [76], it has been reported that nanoscopic domain nucleation typically requires much higher electric-field strengths [74, 76, 77]. In general, domain nucleation is followed by forward and sideward growth of the switched volume [76, 78].

There are also PFM studies about the dynamics of switching [79], but in most cases, they are limited to the inspection of switched domain areas after the application of the switching pulse. By variation of the height and length of the pulse, the stepwise evolution of the switched domain area can be observed. However, a real-time measurement of domain nucleation by PFM appears to be impossible due to its intrinsic bandwidth limitations given by the mechanical coupling to the cantilever motion.

Optical methods can in principle overcome this limitation in time resolution. Pulsed laser sources are available with pulse lengths down to the femtosecond range, which makes possible the inspection of ultrafast processes. For ferroelectrics and at much larger time scales the principle of stroboscopic monitoring of dynamic processes is widely used for macroscopic studies on domain evolution under external electric fields, and was already applied by Merz et al. in 1954 [80]. Other studies focus on the time-resolved electro-optic response to microwaves, to investigate the origin of losses for instance [81]. Furthermore, second-harmonic generation has been used at the microscopic scale to monitor the state

of polarization during switching with high temporal resolution [82]. This demonstrates the power of time-resolved optical methods and makes the combination of time resolution with very high spatial resolution an attractive long-term goal.

The hysteresis studies in this work concentrate on local-scale optical hysteresis measurements based on a SNOM setup, yet without providing time resolution. The intention is to find a suitable instrumentation for the local optical hysteresis measurement, which could later be upgraded with temporal resolution. In addition, the measurements provide information about the ferroelectric switching behavior as a complement to PFM investigations.

5.2 Experimental approach and results

Local scale electro-optic hysteresis measurements are performed with the same setup and under similar conditions as used for the electro-optic domain imaging reported in chapter 4. Details of the experimental setup are illustrated in Fig. 5.2. For safety reasons, mainly to protect the electronics connected to the tuning fork, the switching voltage is applied at the counter-electrode only, which is attached to the back of the sample. This is necessary to prevent possible leakage currents and sparkovers, since the conductive tip and the electrodes of the tuning fork are situated in close proximity to each other as described in Sec. 3.3.2. The much smaller modulation voltage, needed to probe the electro-optic response, is either added to the potential of the counter-electrode or applied directly to the conductive tip. Special care has to be taken with regard to the mounting and support of the sample, since the application of higher switching voltages induces electrostatic forces, which can cause unwanted movements of the sample and the support.

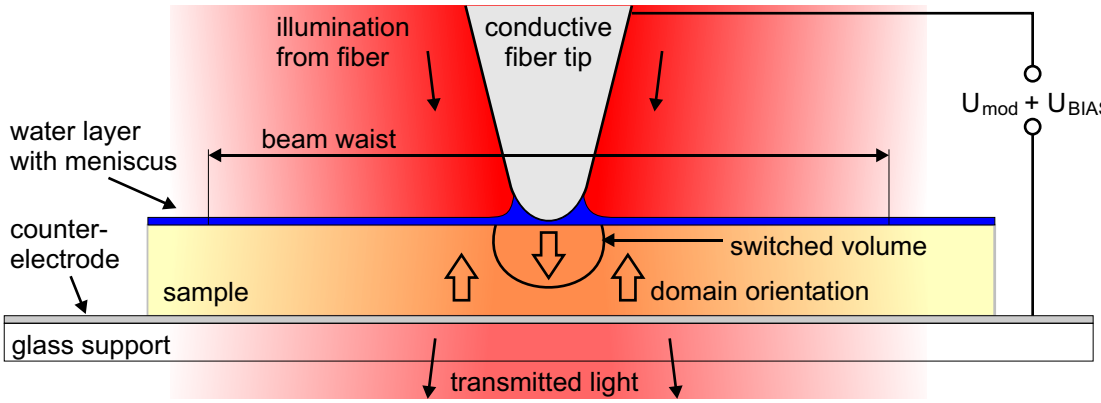

Fig. 5.2 *Setup for the local hysteresis measurement by electro-optic response. The conductive tip is placed at small distance in front of the ferroelectric sample. Variation of the strength of shear-force interaction is used to select different tip-sample separations. The switching voltage U_{Bias} as well as the electro-optic probing voltage U_{Mod} are applied between tip and counter-electrode. Increasing bias voltage will lead to nucleation and growth of a switched volume underneath the tip.*

The application of rather high switching voltages is necessary since barium titanate single crystals of about 200 µm thickness are used for the hysteresis measurements, the same as used also for domain imaging and domain wall inspection within this work. Prior to the hysteresis measurements, the domain pattern and the topography are imaged to ensure save identification of a specific same sample spot for consecutive measurements by various scanning probe techniques.

In our experiments different tip-sample separation is selected by incorporating the distant-dependent strength of shear force interaction with the water adsorption layer, the meniscus and sample surface (Sec. 3.3.2). This interaction leads to a damping of lateral tip oscillation, which decreases the detected tip amplitude. To control the distance a certain relative value of the oscillation amplitude (compared to the case without shear force damping) is used as setpoint for the distance controller. The relation between a selected setpoint and resulting relative tip-sample separation can be obtained by approach curves as presented in Fig. 3.9, while the absolute tip-sample separation is not determined exactly . Since the obtained results of relative tip-sample separation differ significantly for subsequent runs of approach curve recording, the average values, still with potentially large errors (at least 50%), are used for further discussion (Tab. 5.1).

Table 5.1 *Lookup table for the relation between the setpoint and the relative tip sample separation*

setpoint	relative tip-sample distance d [nm]		
%	run 1*	run 2*	average value
95	-4.4	-6.7	-5.6
90	-5.2	-8.2	-6.7
85	-5.5	-9.5	-7.5
80	-5.8	-10.0	-7.9
75	-6.1	-10.6	-8.4
70	-6.4	-11.0	-8.8
64	-6.9	-11.5	-9.2

**An additional offset between the "snap-in" and the water-layer position is introduced to improve consistency between the two different approach curves.*

In the experiment a sufficiently high bias voltage between the tip and the counter-electrode will switch the polarization directly underneath the tip apex. After such a nucleation of an inversely poled domain, the switched volume grows under the influence of the applied field. It can be expected that the growth of a domain can be tracked up to a diameter, for which the electro-optic response signal should saturate. This is found to be about 400 nm for the chromium-coated fiber tips in use (Sec. 4.3.1), since the area addressed by electro-optic response probing corresponds to the lateral resolution obtained in domain imaging.

Figure 5.3 shows hysteresis curves recorded for a sequence of different tip-sample separations, according to a varied setpoint of the shear-force distance control. The presented curves, which were averaged across four cycles, were recorded at a slow speed with a cycle time of 20 s. The shape, width, and height of the hysteresis curves in Fig. 5.3 show a dependence on the selected tip-sample distance. For smaller tip-sample separation (setpoint values of 64%...75%), nicely shaped hysteresis curves are obtained, showing a rudimentary saturation at the turning points of the bias voltage. With a further increase of the tip-sample distance (setpoint 80%...90%), the curve shape gets more disturbed and no evidence for saturation is found anymore.

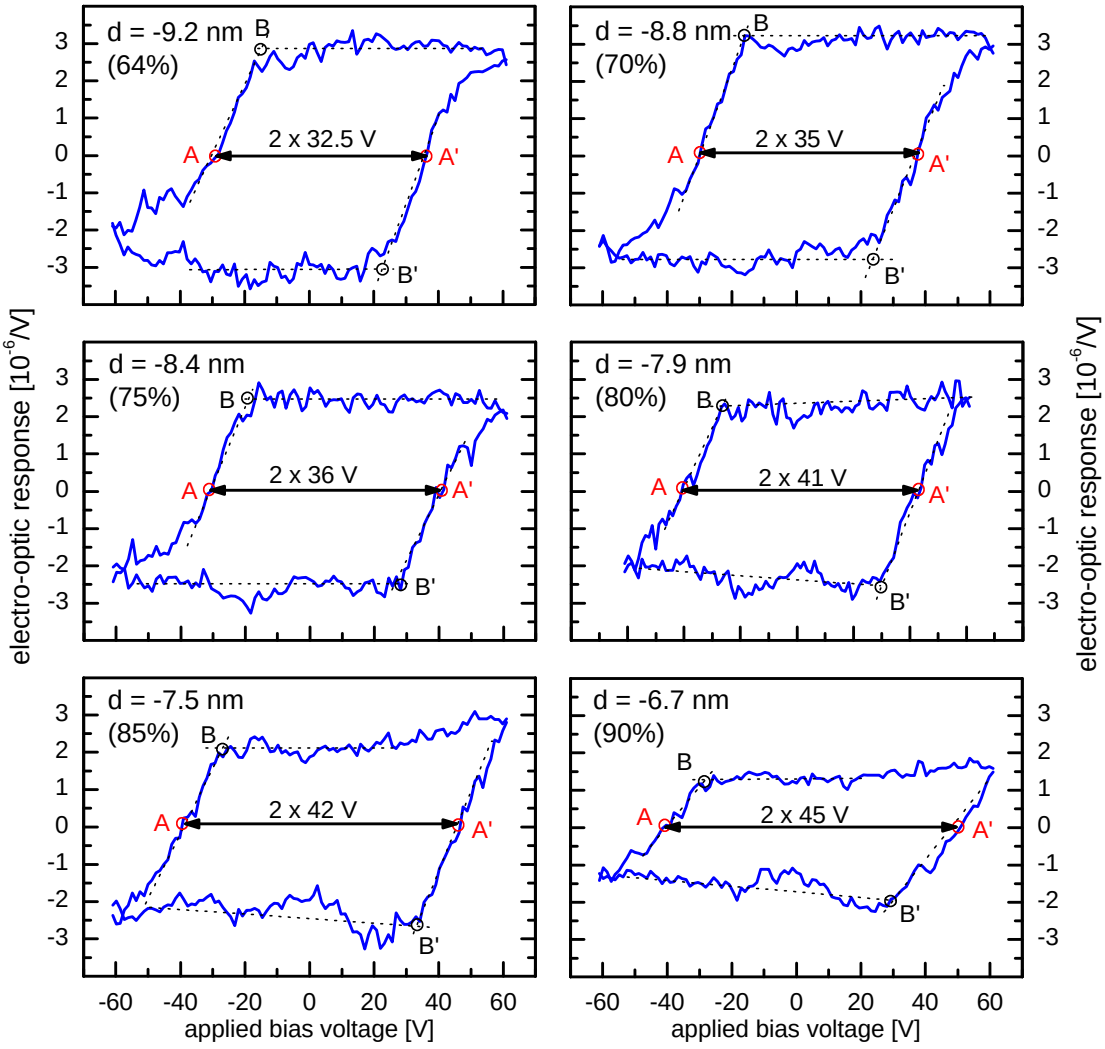

Fig. 5.3 *Ferroelectric hysteresis measured by means of electro-optic response with a chromium-coated fiber tip for different tip-sample separations. The points A,A' mark the coercive voltages while B,B' mark the onset of significant signal change. Saturation is not reached for most of the hysteresis curves. The coercive voltages as well as the onset voltages decrease when the tip-sample separation is reduced, while the electro-optic response signal at zero bias increases. This can be attributed to an increased value of applied field strength at smaller tip-sample distance.*

Altogether, we find a general trend of the coercive voltages (A, A' marks in Fig. 5.3) as well as the voltages marking the onset of significant change (B, B' marks in Fig. 5.3) with tip-sample distance. This is shown in Fig. 5.4, together with the electro-optic response signal measured at zero bias voltage. The coercive voltages as well as the voltage for the onset of significant change decrease when the tip-sample separation is reduced, which is accompanied by an increase of the electric-field strength applied to the sample. In contrast to this, the magnitude of the electro-optic response signal increases. This can be attributed to the increased probing field as well as the saturation level of switching reached during the hysteresis loop.

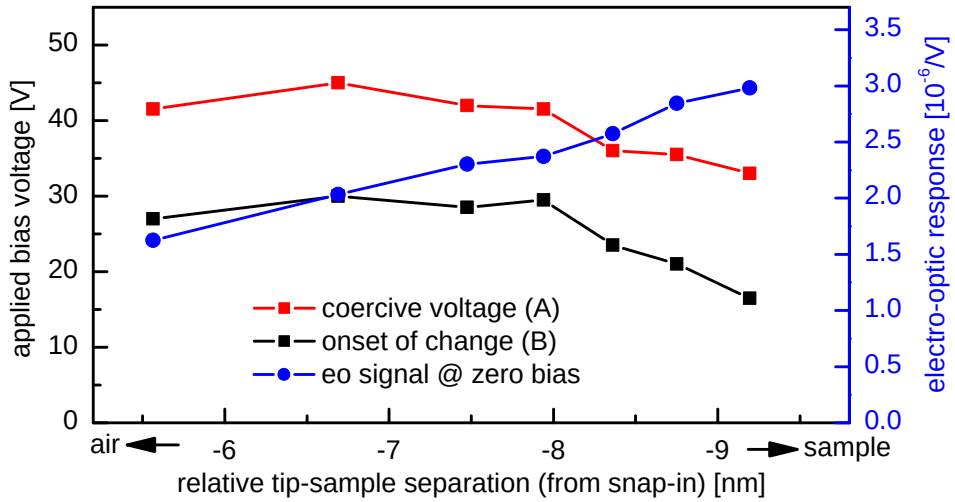

Fig. 5.4 *Dependence of the parameters of electro-optically acquired hysteresis curves on tip-sample separation. The coercive voltage decreases while the electro-optic response signal increases with decreasing tip-sample separation. The indicated z scale was taken from Tab. 5.1 and is subject to large uncertainty.*

There are indications that the obtained hysteresis curves are subject to secondary effects originating from the applied bias voltage, which introduces additional electrostatic forces. Therefore the selected effective tip-sample separation might change during the hysteresis measurement. If the distance control is disabled during the measurement, significant changes of tip oscillation amplitude and even of the transmitted light intensity occur, revealing an unwanted tip or sample movement. The connected risk of tip damage is the reason why the reported measurements were performed under active control of the tip-sample distance. The actuator position as recorded during acquisition of a hysteresis loop, shown in Fig. 5.5, can be used assess the effects of the bias voltage on the tip-sample separation. The plots of Fig. 5.5 show the recorded sample z position for two different setpoints of the distance feedback. In both cases, the sample is retracted at higher bias voltages, indicating a nominal increase of tip-sample separation.

There are two possible reasons for this. On the one hand, it may reflect the compensation of a tip or sample movement induced by the field. In this case, the real tip-sample separation remains constant. On the other hand, the amplitude of the tip oscillation can be directly affected by the additional electrostatic interaction. This is a mechanism that is known from Kelvin probe force microscopy (Sec. A.2). For both cases, a parabolic dependence on the bias voltage is expected, because this is found for electrostatic forces in general. This is the reason why the effective change of tip-sample distance remains undetermined, since the two possible contributions to the change cannot be separated clearly. Nevertheless, the dependence of the effect shown in Fig. 5.5 onto the selected amount of mechanical damping indicates a significant contribution of the direct influence of the electrostatic forces onto the tip amplitude. There, we observe less actuator movement for a larger amount of mechanical damping (smaller setpoint). In contrast to this, the movement is increased for smaller damping (larger setpoint). The effect can be attributed to the larger relative influence of the electrostatic forces at smaller values of mechanical damping. This proves the presence of a direct effect on the tip amplitude and indicates therefore a remaining effective change of tip-sample separation. The associated increase of tip-sample separation at higher bias voltages decreases, of course, the applied field strength available for ferroelectric switching. Therefore, higher coercive voltages and higher voltages for reaching the saturation region can be expected compared to case of a fixed tip-sample separation.

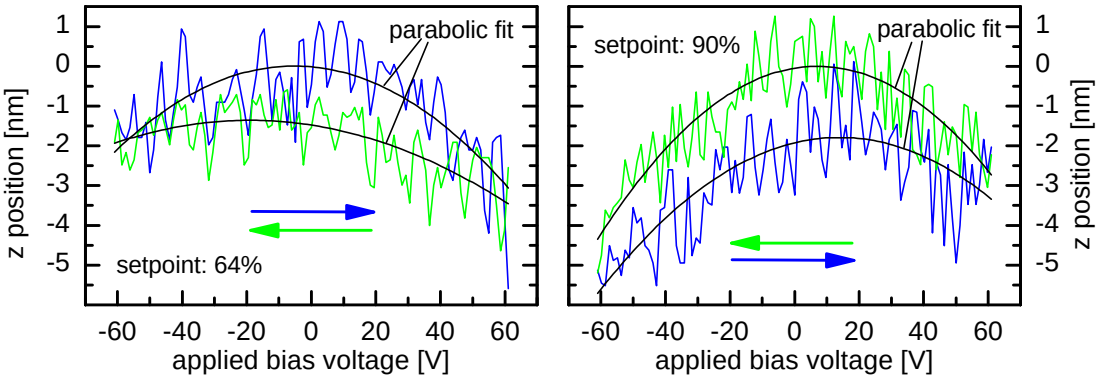

Fig. 5.5 *Response of the tip-sample distance control during a hysteresis measurement. The recorded actuator position shows a parabolic bias voltage dependence due to introduced electrostatic forces as known from Kelvin probe force microscopy (Sec. A.2). A significant direct effect on the detected tip oscillation amplitude can be assumed, since the magnitude of the measured effect depends on the selected damping by shear force interaction. This finally indicates an increased tip-sample separation for larger absolute values of applied bias voltage. The effective change of tip-sample distance remains undetermined due to the unknown contribution of sample movement.*

5.3 Reference hysteresis curve measurements

Without additional information from reference measurements or modelling, the obtained values of the coercive voltages of 33. . . 45 V, depending on the setpoint, have relevance only for the given tip-sample setup. They represent the switching voltage needed to produce artificial domain structures with the given tip. For this reason the comparison of these values with results obtained with other tip types and probing methods is of great interest.

At first, the above results, measured with the simple etched fiber tips, can be compared with results obtained by aperture probes, shown on the left side of Fig. 5.6. There, the same method of electro-optic response was applied, but with the probed volume being smaller due to the additional confinement of the optical field. This leads to a decrease of the coercive voltage to a value of about 13 V. Furthermore, no significant influence of changed tip-sample distance is found in the investigated setpoint interval.

The results of the electro-optic hysteresis measurement can be further compared with the results of hysteresis measurements by PFM at the same sample spot, shown on the right side of Fig. 5.6. There, the tip apex of the AFM cantilever is in contact with the sample surface, which increases the applied field strength. For this reason and because of the further reduced probing volume, the coercive voltage is decreased to a value of about 8 V.

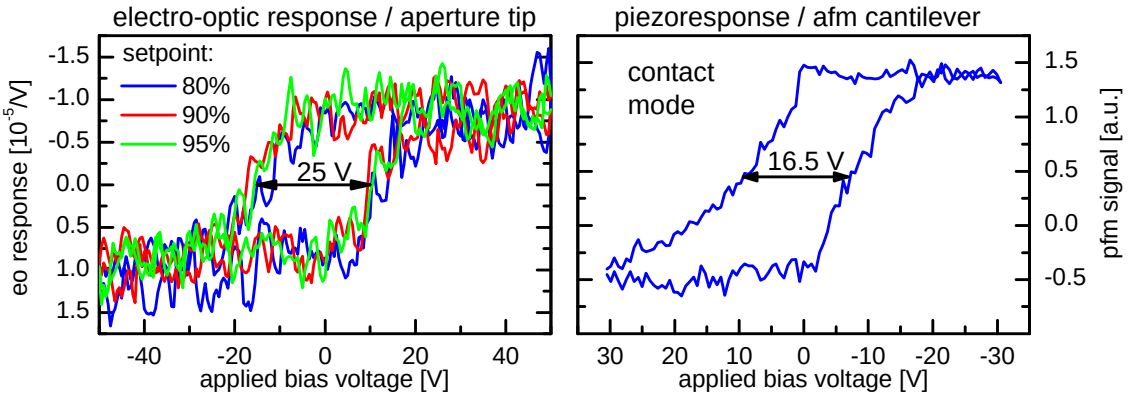

Fig. 5.6 *Reference hysteresis measurements. The left graph shows the hysteresis curve obtained by electro-optic response with an aperture tip. The decrease of the coercive voltage for this measurement is attributed to the smaller probed volume that needs to be switched for a certain amount of signal change. The right graph shows the hysteresis curve measured by piezoresponse force microscopy at the same sample spot. An even stronger reduction of coercive voltage is found, due to a further decrease of the probed volume and due to direct tip-sample contact.*

5.4 Conclusions

The measurements presented demonstrate the ability of the electro-optic response method to measure local hysteresis. The coercive voltages could be reproduced with different fiber tips of the same type to within ±50%. This variation can be attributed to different tip geometry, but may also be caused by changed environmental conditions, which affect the thickness of the water layer, for example. In general, the mechanical stability of the setup at higher bias voltages is not good enough in most cases, due to unwanted electrostatic forces acting on the tip-on-tuning fork system and on the sample. Only in a limited number of cases, such as the reported ones, is the setup insensitive enough to these disturbances to provide stable hysteresis curves. It turns out that the tip-on-tuning fork setup in its present form is not the best suited one for this type of measurements. But also for the tips used further improvements would be helpful, not only with respect to their geometrical, electrical, and optical properties, but also concerning the mechanical stability of the tip itself and its coating. Especially after the application of voltage pulses, one observes debris around the location of switching in subsequent topography scans. Presumably, it stems from the semitransparent chromium coating of the tip or from adsorbates previously picked up during scanning. Therefore, a conductive coating of the fiber tip that is more robust will be necessary to study the response to voltage pulses, as needed for time-resolved investigations of local-scale domain nucleation and domain growth.

Time-resolved experiments in combination with the modelling of the electric-field distribution induced by the tip could make possible the study of the radial domain growth dynamics and of its dependence on the local electric field. This could give a deeper insight into the nanoscale domain switching characteristics. But already the interpretation of the slow-speed hysteresis measurements presented above, profits considerably from supporting modelling of the electric field and the electro-optic response, as will be reported in Sec. 6.3.3. It allows us to study the influence of experimental conditions such as meniscus formation, tip geometry, spot size, and spot shift on the hysteresis and domain imaging characteristics. The comparison of the experimental results with the results of model calculations can be used to assess some unknown parameters of the experiment such as the meniscus size.

Chapter 6

Modelling electro-optical measurements

Based on the calculation of the electric-field distribution within the sample system, we model the electro-optic response of different domain configurations as well as ferroelectric switching. After a description of the model and its parameters, the influence of anisotropic samples and water adsorption layers on the electric field distribution is discussed first. After this, the derived electric field is used as an input for the calculation of the induced electro-optic response. The resulting images, modelled for a given domain distribution, are compared with the experimental results concerning the quantitative effect and the lateral resolution. The different contributions to the electro-optic response signal as well as the influence of the optical tip properties are discussed for the case of domain imaging. The last part of the is devoted to modelling the measurement of the ferroelectric hysteresis by electro-optic response.

6.1 Introduction

A growing number of scanning probe methods investigate the interaction of the sample with an external electric field applied via an electrically biased tip. Among these methods are piezoresponse force microscopy, Kelvin probe force microscopy, and electro-optic scanning probe microscopy, as used for detailed investigations of polar dielectrics and ferroelectrics.

It is obvious that the electric-field distribution for the given tip-sample geometry is very important for an improved qualitative and quantitative understanding of the interaction studied. Due to the special geometry, which is characterized by the tip-shaped electrode, confinement and enhancement of the electric field close to the tip are crucial.

All information derived by modelling is in general limited to idealized geometries and may depend on the assumption of a variety of model parameters. Tip properties such as the exact shape and conductivity at the apex are not only hard to determine but also possibly subject to changes during the experiment due to particle pickup or other deformation. If

the experiment is run under ambient conditions, also adsorbates can play an important role. Their distribution, characterized by layer thickness, wetting of the tip, and so on, as well as their physical properties can only be taken into account in the model by means of idealizing assumptions.

The result of the electric-field calculation is relevant for a variety of scanning probe techniques. Within this work, we focus on qualitative and quantitative modelling of electro-optic response and connected hysteresis measurements. In addition, similar calculations are successfully applied to investigate quantitative resolution limits in Kelvin probe force microscopy (Sec. A.2).

6.2 Electric-field modelling

6.2.1 Theoretical description

In the following, only quasi-static fields are considered. The electric-field distribution is determined then by the solution of the static subset of Maxwell's equations given by

$$\operatorname{div} \vec{D} = \rho \,, \tag{6.1}$$

$$\operatorname{rot} \vec{E} = 0 \,. \tag{6.2}$$

These local equations in terms of the electric field $\vec{E}$, the dielectric displacement $\vec{D}$, and the density of free electric charge ρ are connected by the material equation:

$$\vec{D} = \varepsilon_0 \, \boldsymbol{\varepsilon} \, \vec{E} \,, \tag{6.3}$$

where $\boldsymbol{\varepsilon}$ denotes the $\boldsymbol{\varepsilon}$ tensor in case of anisotropic media.

The second equation (Eq. 6.2) is inherently fulfilled if the problem is described in terms of the electrostatic potential Φ with

$$\vec{E} = -\operatorname{grad} \Phi \,. \tag{6.4}$$

In combination with Eq. 6.3, the first equation (Eq. 6.1) turns into

$$\operatorname{div} \left(\boldsymbol{\varepsilon} \, \vec{E} \right) = \rho, \tag{6.5}$$

which remains to be solved. If there are no free charges ($\rho = 0$) and $\boldsymbol{\varepsilon}$ is diagonal, Eq. 6.5 can be expressed as

$$\frac{\partial}{\partial x} \left(\varepsilon_x \frac{\partial}{\partial x} \Phi \right) + \frac{\partial}{\partial y} \left(\varepsilon_y \frac{\partial}{\partial y} \Phi \right) + \frac{\partial}{\partial z} \left(\varepsilon_z \frac{\partial}{\partial z} \Phi \right) = 0 \,, \tag{6.6}$$

with $\varepsilon_x = \varepsilon_{xx}$, $\varepsilon_y = \varepsilon_{yy}$, and $\varepsilon_z = \varepsilon_{zz}$ denoting the diagonal elements of the $\boldsymbol{\varepsilon}$ tensor. For the calculation, we have to specify their values within the region of interest as well as the potentials at the surfaces of the tip and the counter electrode.

For numerical computation of the electric potential Φ by means of the finite-element method, the region under consideration is divided into a mesh of small cells. The mesh density varies over several orders of magnitude, in accordance with the need to reproduce various geometrical features such as the tip apex. Then, the potential function $\Phi(\vec{r})$ is approximated across each single cell by taking the given boundary conditions into account. The cell is subdivided in the next computation cycle if its estimated error exceeds a given limit. Thereby, an adaptive mesh refinement takes place until a preselected accuracy is reached.

6.2.2 Geometrical layout of the model

There are several competing requirements that govern the choice of geometry parameters for the numerical computation. Since a large density of computation cells is needed to achieve high accuracy close to the tip apex, the outer dimensions of the model should be as small as possible to meet practical requirements on computation time and memory. On the other hand, proper boundary conditions at the borders of the volume of computation are only given at the electrode areas. The outer boundaries with undefined potential should be far away from the region of interest and this suggests using a larger model, which also comes closer to the geometrical extension of the real experiment. As a compromise we use the geometry illustrated in Fig. 6.1. Whenever allowed by symmetry, we may further reduce the model volume or even its dimensionality for further reduction of computational requirements.

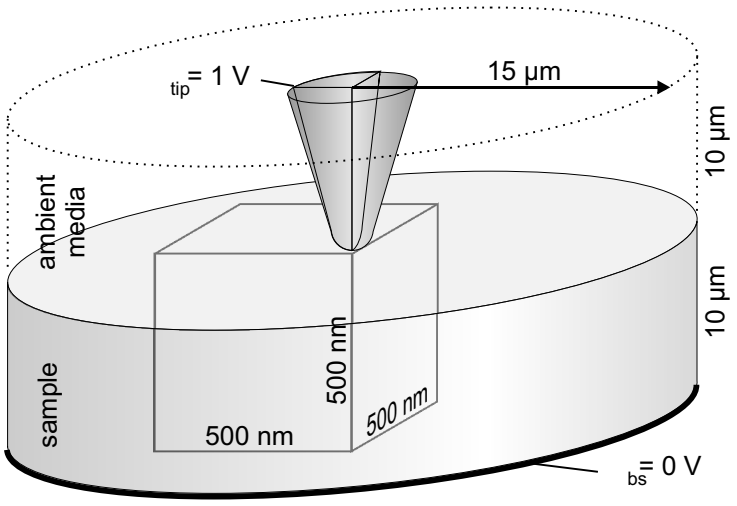

Fig. 6.1 *Model geometry used for numerical electric-field calculation. The conductive tip with a tip radius R_{tip} is placed at a distance d above the sample. The electric potential difference between tip and back electrode is set to $\Phi_{tip} - \Phi_{bs} = 1\ V$. The calculation is typically done within a cylinder having a radius of 15 µm, while the sample thickness and the vertical extension of the tip are set to 10 µm each. The highest possible symmetry is always used to decrease the size and dimensionality of the model volume as much as possible. Results are plotted on the faces of a cube with a side length of 500 nm placed below the tip as indicated.*

The computation is always carried out with a fixed difference of electric potential $\Phi_{tip} - \Phi_{bs}$ of 1 V between the conductive tip and the counter-electrode at the back of the sample. Electric fields for voltages different from 1 V can be easily determined by rescaling.

For the discussion of the distribution of the magnitude of the electric field and of its individual components within the sample, the results are plotted on the faces of a cube having a side length of 500 nm as indicated in Fig 6.1. This cube is positioned at the sample surface with one of its corners directly below the tip apex.

6.2.3 Anisotropic dielectric samples

In most cases, dielectric materials are used in plate-capacitor-like structures where they are subject to more or less homogeneous electric fields. Then, only the effective dielectric constant along the field direction is relevant and anisotropy plays a minor role. The tip-sample model discussed in this section is characterized by a much more complex electrode geometry leading to an inhomogeneous electric-field distribution with components along all directions, making anisotropy more important.

Figure 6.2 shows the results of electric-field calculations for different strengths and orientations of anisotropy with respect to the given tip-sample geometry. The dielectric constants $\varepsilon_c = 136$ along the c axis, and $\varepsilon_a = 4400$ perpendicular to the c axis of barium titanate were taken from the literature [24]. We consider five different cases: the extreme cases of an a and a c domain in $BaTiO_3$, two analog cases with less pronounced anisotropy, and the isotropic case. In all cases, we keep the value of $\sqrt{\varepsilon_c \varepsilon_a \varepsilon_a}$ constant for better comparability. The model geometry is characterized by a tip radius $R_{tip} = 150$ nm, a tip-sample separation $d = 5$ nm, and an ambient medium with $\varepsilon = 1$. The calculated distribution of the electric field $\vec{E}$ is plotted on the faces of a cube as shown in Fig. 6.1 in terms of its magnitude $|E|$ and its components normal ($|E_\perp| = |E_z|$) and parallel ($|E_{||}| = \sqrt{E_x^2 + E_y^2}$) to the sample surface plane.

The result for an isotropic sample is shown in the center row of Fig. 6.2. The magnitude of the electric field is governed by the large value of the dielectric constant $\varepsilon = 1380$, while the qualitative shape of the field distribution is not affected significantly if ε is varied (not shown). The decomposition of the electric field $\vec{E}$ into its components $E_\perp$ and $E_{||}$ reveals their different spatial distributions. $\vec{E}$ is dominated by $E_\perp$ directly below and by $E_{||}$ beside the tip apex position. Overall, $E_\perp$ and $E_{||}$ have similar influence.

The top rows of Fig. 6.2 show the results for an anisotropy corresponding to c domain orientation. Here, the dielectric constant ε along the normal direction is smaller than along the lateral directions. With stronger anisotropy, the electric field becomes stronger in a volume close to the sample surface. Therefore, the field distribution is characterized by a stronger confinement in the normal direction, but less lateral confinement. The field components indicate that this is mainly due to an increase of the normal component $E_\perp$ close to the surface, while the lateral component $E_{||}$ becomes more localized to the sample surface without much change in magnitude. This behavior is different for the isotropic

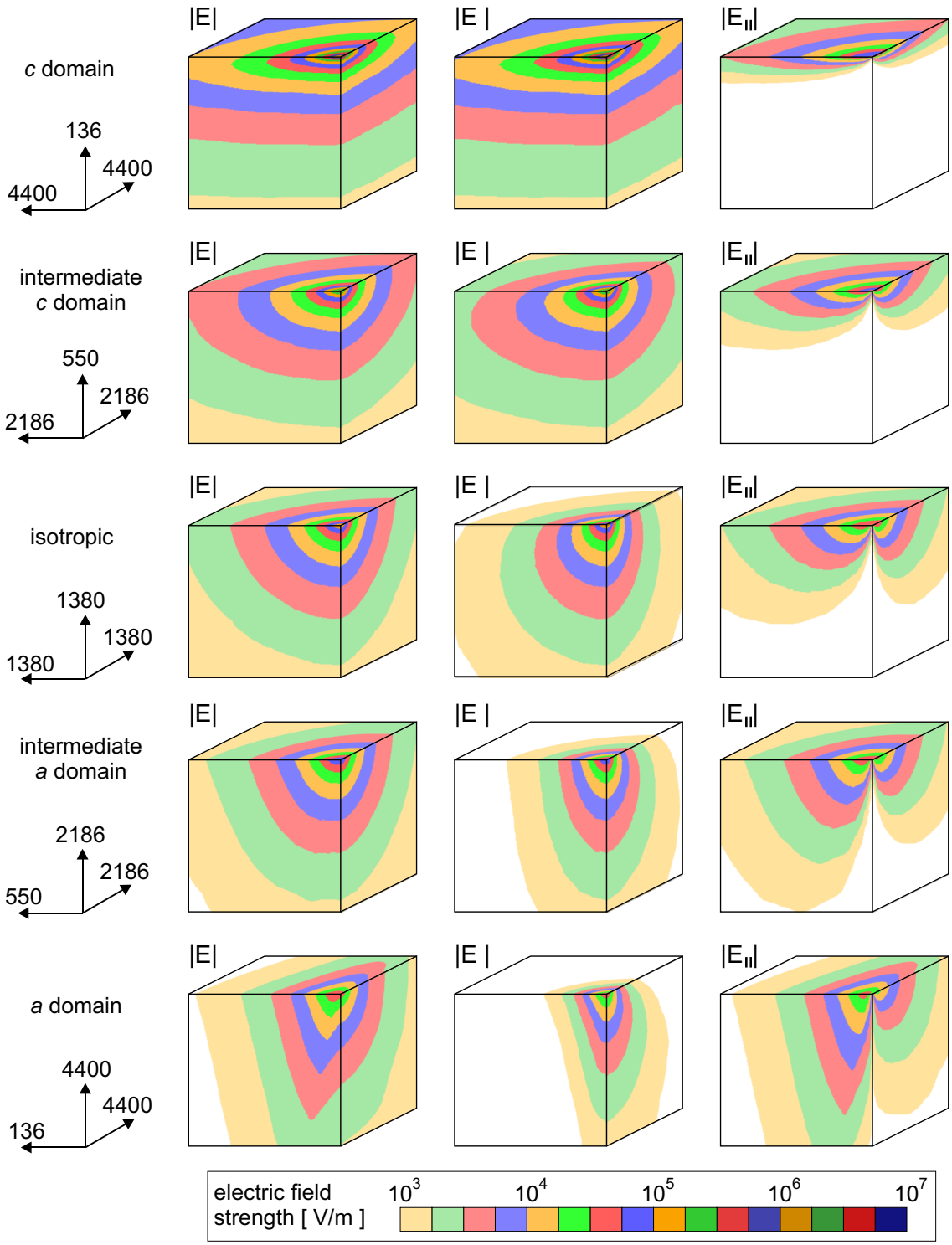

Fig. 6.2 *The effect of an anisotropic sample on the electric-field distribution produced by a tip (R_{tip} = 150 nm) at a distance d = 5 nm. The magnitude $|E|$ as well as the components normal ($|E_{\perp}|$) and parallel ($|E_{||}|$) to the sample surface indicate how the distribution of the electric field $\vec{E}$ is influenced by a change of the dielectric anisotropy. The c domain is characterized by increased normal and decreased lateral confinement of $\vec{E}$, while the a domain is characterized by a better lateral but less normal confinement. A complex interplay between the different field components and the associated dielectric constants is revealed.*

case. There, a general increase/decrease of all field components with decreased/increased dielectric constant is found throughout the whole volume of the model, as expected from the simple model of a plate capacitor partly filled with a dielectric. In the anisotropic case, it is not possible to consider each field component with its associated dielectric constant separately. Since all field components with their respective dielectric constants are linked by Poisson's equation Eq. 6.6, anisotropy introduces complex interdependencies having no simple explanation anymore.

The bottom rows of Fig. 6.2 present the results for an anisotropy corresponding to *a* domain orientation. Now, the dielectric constant along the lateral x direction is decreased, while it is increased along the normal direction and y direction. Compared to the isotropic case, the electric-field strength across the plotted volume is only slightly decreased. Since the dielectric constants along the lateral directions are different, the electric-field distribution gets different along these directions, too. The lateral field component along the x axis, gets much more dominant, decreasing the influence of the normal field component. This also splits the point of maximum field strength into two points shifted along the x axis. Altogether, compared with the results for the *c* domain orientation, higher lateral and less normal confinement of the electric-field distribution is found.

6.2.4 Effect of water layer and meniscus formation

The presence of a water adsorption layer in experiments run under ambient conditions has already been shown in Sec. 3.3.2 and Sec. 4.2. The typical thickness of this layer on a $BaTiO_3$ sample is found to be in the order of 10 nm. The shape and size of the corresponding meniscus and their dependence on the tip-sample separation are not accessible in the present experiments and can therefore only be roughly estimated. The geometry of water layer and meniscus assumed in the model is illustrated in Fig. 6.3. The meniscus shape is approximated by a segment of a circle with radius R_{men}. The meniscus size follows from R_{men} in connection with the radius $R_{contact}$ of the contact point between meniscus and tip.

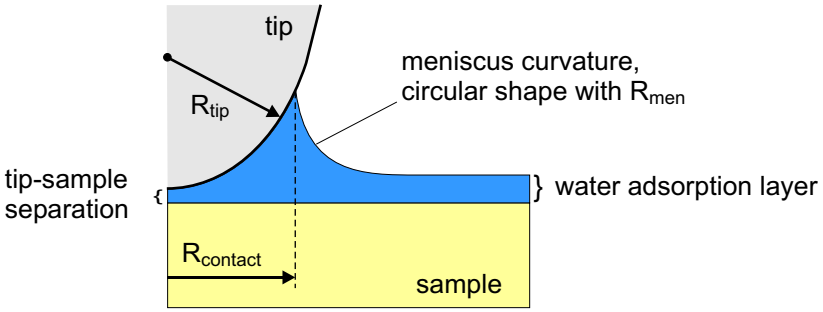

Fig. 6.3 *Geometry of the water layer and meniscus used in the model. The meniscus shape is approximated by a segment of a circle, while its size is also determined by the radius of contact between tip and meniscus. Modelling is done with* $R_{men} \backsimeq R_{contact} \backsimeq R_{tip} \backsimeq 150$ *nm.*

To investigate the influence of the water layer and meniscus formation on the electric-field distribution, the calculation is run with three different configurations with regard to the medium filling the space between tip and sample, while the tip radius as well as the tip-sample separation are kept constant. The first case assumes air or vacuum as ambient medium with a dielectric constant of $\varepsilon = 1$, with no water layer present. For the second case $\varepsilon = 82$ is assumed for the ambient space, being filled completely with water. The third case covers the situation with water layer and meniscus formation as illustrated in Fig. 6.3. R_{men} and $R_{contact}$ are assumed to be equal to the tip radius $R_{tip} = 150$ nm. We limit the treatment to c domain geometry, which allows us to reduce the calculation to two dimensions because of cylindrical symmetry. This provides increased accuracy at lower requirements on computational resources.

The calculated distributions of the electric-field strength E and its components perpendicular ($E_\perp$) and parallel ($E_{||}$) to the sample surface are shown in Fig. 6.4 for all three cases. The influence of the water layer is found to be twofold:
(i) Comparison of the two limiting cases, with the ambient medium being only air or water, demonstrates the effect of better "matching" between the dielectric constants within the tip-sample gap and in the sample. In case of water as ambient medium the applied field within the sample is more than one order of magnitude larger than in case of air, while the qualitative shape of the electric-field distribution remains almost unaffected. The effect of increased field strength is explainable by a simple plate capacitor model filled with different dielectric media.
(ii) The comparison between the cases with a meniscus and with only water in Fig. 6.4 reveals additional electric-field confinement by the meniscus. Especially at the sample surface, the $E_\perp$ component is found to be much more confined laterally. Underneath the tip apex, i.e. for radial positions $r < R_{contact}$, the magnitude of $E_\perp$ is further enhanced by a factor of two, while its radial decay is similar to the water-only case. For $R_{contact} < r < R_{contact} + R_{men}$, the radial decay is much steeper for the meniscus than in the water only case, whereas the decay is similar again in both cases for $r > R_{contact}+R_{men}$.

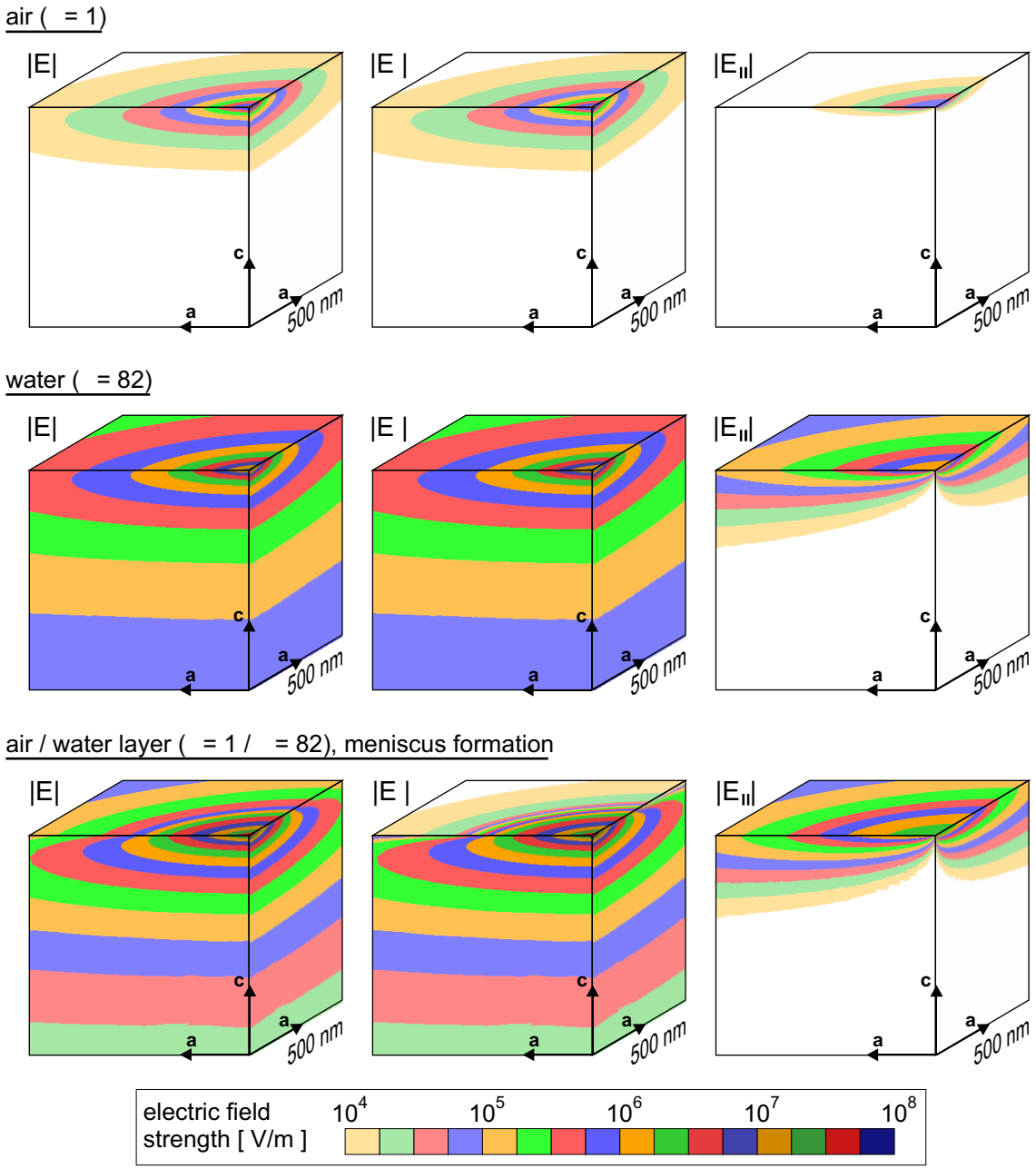

Fig. 6.4 *Effect of water adsorption layer and meniscus formation on the distribution of the electric field (E) and its perpendicular ($E_\perp$) and parallel ($E_{||}$) components with respect to the sample surface. The electric field strength increases by more than one order of magnitude if the ambient space is completely filled with water instead of air. In this case, the shape of the field distribution remains unaffected. If the water is present as a thin film with a meniscus filling the gap between tip and sample, an additional confinement of the electric field distribution is found in lateral directions mainly.*

6.3 Electro-optic response modelling

6.3.1 Electric-field induced changes of optical properties

The description of the influence of the electric field on the changed optical properties is much more complex than introduced in Sec. 4.1. Instead of a homogeneously distributed electric field with only a single component, strongly inhomogeneous distributions are found for all field components. Therefore, the influence of all three electric-field components has to be considered for a given domain orientation.

As already described in Sec. 4.1, the altered optical properties are given by the changed elements of the inverse dielectric tensor $\boldsymbol{\eta}$ according to

$$\Delta\eta_{ij} = \Delta\varepsilon_{ij}^{-1} = \left(r_{ijk}^{S} + p_{ijmn}^{E} d_{kmn}\right) E_k = r_{ijk}^{\text{eff}} E_k \,. \tag{6.7}$$

If a crystal having $4mm$ symmetry such as $BaTiO_3$ is considered, all occurring changes can be expressed in the crystal coordinates as

$$\Delta\eta_{ij} = \begin{pmatrix} r_{113}^{\text{eff}} E_3 & 0 & r_{131}^{\text{eff}} E_1 \\ 0 & r_{223}^{\text{eff}} E_3 & r_{232}^{\text{eff}} E_2 \\ r_{311}^{\text{eff}} E_1 & r_{322}^{\text{eff}} E_2 & r_{333}^{\text{eff}} E_3 \end{pmatrix} , \tag{6.8}$$

with $r_{113}^{\text{eff}} = r_{223}^{\text{eff}}$ and $r_{131}^{\text{eff}} = r_{311}^{\text{eff}} = r_{232}^{\text{eff}} = r_{322}^{\text{eff}}$. The complete $\boldsymbol{\eta}$ matrix reads

$$\eta_{ij} = \begin{pmatrix} \frac{1}{n_o^2} + r_{113}^{\text{eff}} E_3 & 0 & r_{131}^{\text{eff}} E_1 \\ 0 & \frac{1}{n_o^2} + r_{113}^{\text{eff}} E_3 & r_{131}^{\text{eff}} E_2 \\ r_{131}^{\text{eff}} E_1 & r_{131}^{\text{eff}} E_2 & \frac{1}{n_e^2} + r_{333}^{\text{eff}} E_3 \end{pmatrix} , \tag{6.9}$$

with n_o denoting the ordinary and n_e the extraordinary refractive index at zero electric field.

In case of a c domain, the crystal coordinate system (123) coincides with the coordinates used in the model system (xyz) and the electric-field components can be directly identified as $E_1 = E_x$, $E_2 = E_y$, and $E_3 = E_z$. For an a domain, we find an additional transformation between the coordinates of the model and the crystal, because of the different orientation. This transformation T_{ij} is simply given by

$$T_{ij} = \begin{pmatrix} 0 & 0 & -1 \\ 0 & 1 & 0 \\ 1 & 0 & 0 \end{pmatrix} \quad \text{and its inverse} \quad T_{ij}^{-1} = \begin{pmatrix} 0 & 0 & 1 \\ 0 & 1 & 0 \\ -1 & 0 & 0 \end{pmatrix} , \tag{6.10}$$

transforming a vector from the model system to the crystal system and vice versa. This transformation maps the electric-field components in accordance with $E_1 = -E_z$, $E_2 = E_y$, and $E_3 = E_x$.

Since optical fields must be described in the model coordinates for the numerical calculations, the resulting η matrix has to be transformed to the model coordinates, too, and is then given by

$$\eta^a_{ij} = \left(T^{-1}\,\eta\,T\right)_{ij} = \begin{pmatrix} \frac{1}{n_e^2} + r^{\text{eff}}_{333}E_3 & r^{\text{eff}}_{131}E_2 & -r^{\text{eff}}_{131}E_1 \\ r^{\text{eff}}_{131}E_2 & \frac{1}{n_o^2} + r^{\text{eff}}_{113}E_3 & 0 \\ -r^{\text{eff}}_{131}E_1 & 0 & \frac{1}{n_o^2} + r^{\text{eff}}_{113}E_3 \end{pmatrix}. \tag{6.11}$$

It it obvious that additional transformations are needed to describe the electro-optic response of inverted domains in the same way. These transformations are reported in the appendix A.1 and leads to a very simple result: The electro-optic response of inverted domains can be described in terms of the response of the non-inverted ones by inverting the signs of all electric-field components. This result is valid for both *a* and *c* domains.

The next step for modelling the electro-optic measurements is to transform the changed optical properties, as given by the $\boldsymbol{\eta}$ matrix, into a change of transmitted light power, which is the quantity recorded in the experiment. For this, Fresnel's formula is applied to calculate the local transmittance for each addressed point on the sample surface, which we do by simply using the electro-optically changed refractive index Δn_s directly at the surface. In a more accurate treatment, one would have to calculate an effective change Δn_{eff} for the given depth profile of Δn. However, this value comes close to Δn_s, provided that the decay of Δn into the sample is not too steep. In the present case, this is fairly well fulfilled as illustrated by Fig. 6.5, which shows $\Delta n_{eff}/\Delta n_s$ for an exponential Δn profile, as calculated for $\lambda = 633$ nm and normal incidence [83]. From this, values of 96% and 74%, respectively, rather close to 100% for an *a* and a *c* domain can be estimated, which demonstrates that our simplified treatment is satisfactory.

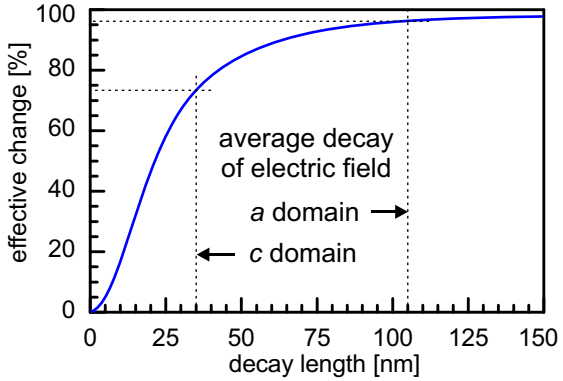

Fig. 6.5 *Quality of the approximation by Fresnel's formula for a spatially nonuniform change of the refractive index. The curve was calculated for an exponentially decaying change of the refractive index [83] at a wavelength $\lambda = 633$ nm and shows the effective value of the change. The accuracy of the approximation for the electro-optic-response modelling of a and c domain areas is reflected by the effective changes of 96% and 74%.*

Table 6.1 *Probed electro-optic coefficients and corresponding field components with respect to the selected orientation $\vec{u}$ of optical polarization.*

$\vec{u} = (u_x, u_y, u_z)$	probed η_{uv}	probed $r_{ijk}E_w$	
		a domain	c domain
$(1, 0, 0)$	η_{xx}	$r_{333}E_x$	$r_{113}E_z$
$(\cos\phi, 0, \sin\phi)$	η_{xx}	$r_{333}E_x$	$r_{113}E_z$
tilt in xz plane	η_{zz}	$r_{113}E_x$	$r_{333}E_z$
	η_{xz}, η_{zx}	$-r_{131}E_z$	$r_{131}E_x$
$(0, 1, 0)$	η_{yy}	$r_{333}E_x$	$r_{113}E_z$
$(0, \cos\gamma, \sin\gamma)$	η_{yy}	$r_{113}E_x$	$r_{113}E_z$
tilt in yz plane	η_{zz}	$r_{113}E_x$	$r_{333}E_z$
	η_{yz}, η_{zy}	0	$r_{131}E_y$

As incidence of the light can be assumed to be approximately normal in our model, the transmission coefficient $T(n)$ is simply given by

$$T(n) = \frac{4n}{(n+1)^2}\,. \tag{6.12}$$

With reference to Sec. 4.1, the refractive index n can be calculated for normal modes of optical polarization from

$$n(\vec{u}) = (\eta_{ij} u_i u_j)^{-1/2}\,, \tag{6.13}$$

where $\vec{u}$ is the unit vector along the polarization direction of the optical field. By selecting a proper $\vec{u}$, different elements of the $\boldsymbol{\eta}$ matrix can be probed. This way, different electro-optic coefficients and electric-field components can be addressed as listed in Tab. 6.1.

To calculate the total transmitted power, assumptions about the incident light have to be made. The light radiated from an etched fiber tip is characterized by a Gaussian-like focus close to the tip apex, as reported in Sec. 3.2.2. For modelling the incident light, the intensity I is therefore approximated by a Gaussian distribution given by

$$I = I_0 \exp\left(\frac{-2r^2}{w_b^2}\right), \tag{6.14}$$

with w_b being the beam waist parameter. Furthermore, a constant orientation of $\vec{u}$ is assumed across the whole light spot, which is experimentally not given in general. But since no other information about the distribution of $\vec{u}$ is available, this assumption is the most reasonable one. The final transmitted power P_t results from an integration across the illumination profile at the sample surface, weighted with the local transmittance T:

$$P_t = \int T(n) \cdot I \, dA\,. \tag{6.15}$$

For comparison with experimental data, we normalize the electro-optically induced change of P_t to the power at zero field $P_t|_{E=0}$ and to the potential difference $U = \Phi_{tip} - \Phi_{bs}$ between the tip and the back electrode, as already defined for the experiments by Eq. 4.5.

6.3.2 Application to domain imaging

All modelling results presented in the following were derived by using the bulk values of the dielectric constants ε_a, ε_c, refractive indices n_o, n_e, and electro-optic constants r_{113}^{eff}, r_{131}^{eff}, r_{333}^{eff} (unclamped, low frequency), listed in Tab. 3.1. At the sample surface, these values are typically modified as predicted by theory [84]. But as long as no complete set of experimentally validated parameters is available, we prefer using bulk values, even though this may give rise to additional errors of the numbers obtained.

The beam waist parameter was set to a fixed value $w_b = 1$ µm, while the tip radius R_{tip}, meniscus radius R_{men}, tip-sample distance d, tilt angle ϕ of $\vec{u}$ within the xz plane, and lateral shifts s_x, s_y of the illumination profile with respect to the tip apex were varied.

We first discuss the influence of the water adsorption layer and meniscus on the electro-optic-response signal in order to find a range of realistic values of these parameters. Section 6.2.4 already showed that they have strong impact on the electric-field distribution. Since this is the electric field that probes the local electro-optic properties, there is a strong influence on the electro-optic response, too. Again, we consider a c domain, allowing the electric-field calculation to be performed in reduced 2D geometry. However, a sharp 180° domain wall breaks the cylindrical symmetry as far as the electro-optic response is concerned, and therefore the calculation of the electro-optic signal near such a domain boundary requires a complete 3D treatment.

The signal as calculated across a 180° c domain wall is shown in Fig. 6.6 for two different radii $R = R_{tip} = R_{men} = R_{contact}$ of R =100 nm and R =150 nm, and for all three configurations of ambient media (meniscus, water only, air only). The other parameters were set to $d = 5$ nm, $\phi = 0$, and $s_x = s_y = 0$. For both values of R, Fig. 6.6 reveals a significantly enhanced resolution for the meniscus case as compared to the air-only and water-only cases. This is a direct consequence of the additional electric-field confinement caused by the meniscus as described in Sec. 6.2.4. The experimentally determined resolution shown in Fig. 4.7 is well reproduced by the model only if meniscus formation is taken into account. Also the absolute numbers indicate that water must be present between the tip and the sample. The electro-optic signal calculated with only air as ambient medium is much lower than the experimentally observed one, while the values for the water-only and meniscus case fit quite well to the typical experimental value of $5 \cdot 10^{-6}$/V. Therefore, all subsequent calculations were performed under the assumption that a water layer is present and a meniscus is formed with $R = 100 \ldots 150$ nm.

We now extend the modelling to a complete domain structure with mixed a and c domain areas. The assumed domain geometry is illustrated in Fig. 6.7. A stripelike a domain with a width of 2 µm is embedded into a structure of antiparallel c domains. This geometry now makes it necessary to perform the calculation of the electric-field distribution in a complete 3-dimensional treatment.

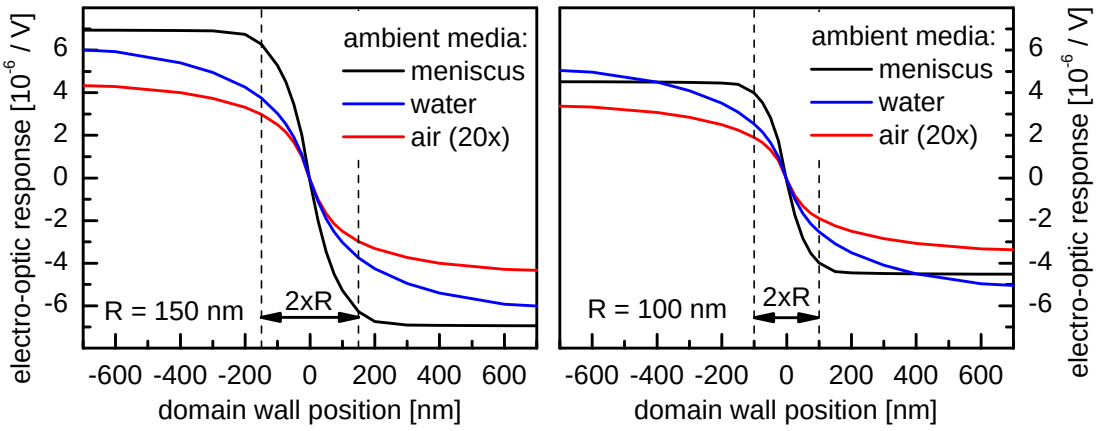

Fig. 6.6 *Effect of water layer and meniscus formation on the electro-optic response as modelled for a sharp 180° c domain wall. For both considered values of the characteristic radius $R = R_{tip} = R_{men} = R_{contact}$, the resolution is enhanced significantly by the meniscus. With regard to both resolution and absolute numbers of the electro-optic response, good agreement with the experiment is only achieved if a water layer forming a meniscus is included in the model.*

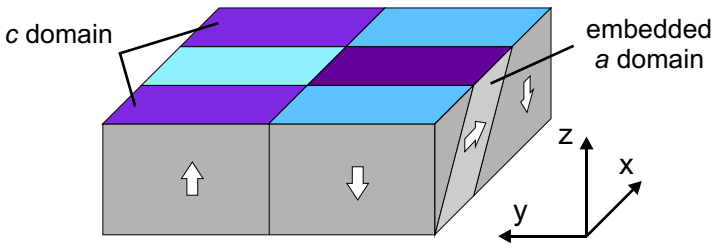

Fig. 6.7 *Mixed domain structure assumed for modelling. A stripelike a domain with a width of 2 µm is embedded into a structure of antiparallel c domains. The walls between the c and a domains run at an angle of 45° into the sample. In accordance with the orientation of the adjacent c domain, the middle stripe contains two antiparallel a domains.*

Because of the increased requirements of a 3D calculation for computational resources, we can afford only a limited number of variations of the geometric parameters. The electric-field modelling is therefore done for two parameter sets only, assuming again $R = R_{tip} = R_{men} = R_{contact}$ with $R = 100$ nm and $R = 150$ nm, respectively, at a tip-sample separation $d = 5$ nm. Once we have calculated the electric-field distribution, we can use it to determine the electro-optic response for different sets of optical parameters.

First, we model the electro-optic response with a simple set of optical parameters given by: beam waist $w_b = 1$ µm, tilt angle $\phi = 5°$, and zero lateral shifts $s_x = s_y = 0$. The resulting electro-optic response signal across the domain structure is shown in Fig. 6.8 for

both values of R. Compared to the experimental data reported in Sec. 4.3.1, the model underestimates the a domain signal, while the c domain signal is reproduced quite well. As seen from the color scale bar in Fig. 6.8, the electro-optic-response signal is stronger in case of $R = 150$ nm than for $R = 100$ nm. The lateral resolution, as deduced from the line profiles in the bottom part of Fig. 6.8, is found to be in the order of $2R$ for both cases, so it is higher for $R = 100$ nm. It is remarkable that the resolution is equal for a and c domain transitions. This is generally not found in the experiment.

Figure 6.8 shows also a very pronounced electro-optic response decorating the a-c domain boundaries. This can be attributed to an extraordinary electric-field distribution close to the boundary, resulting from the changed anisotropy orientation of the dielectric tensor ε. It manifests itself as two rims of opposite sign at the boundaries between the a domain and the two adjacent c domains. Similar effects can be found in experimental data (Figs. 4.6, 4.8, 4.13), where however the decoration being in phase with the a domain response is typically not visible because it may be similar in magnitude to the dominating a domain signal. This is not perfectly reflected in the model, probably due to underestimation of the a domain response.

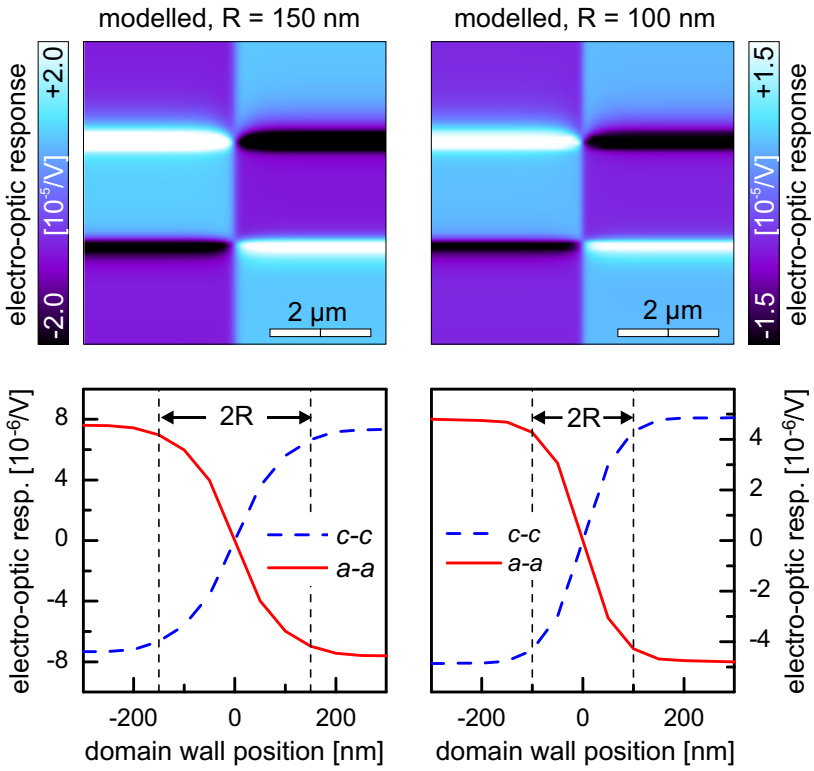

Fig. 6.8 *Modelled electro-optic response at a mixed domain structure. The a domain signal is underestimated, while the c domain signal is reflected correctly, as suggested by comparison with experimental data. Compared with the results for $R = 100$ nm, the electro-optic response is increased and lateral resolution is decreased for $R = 150$ nm. The pronounced electro-optic response at the a-c domain boundaries indicates an extraordinary electric-field distribution at these locations.*

To isolate the contribution of a specific electric-field component, we repeat the calculation of the electro-optic signal with all other components set to zero. Furthermore, we set also the electro-optic coefficients of either the a or the c domains to zero, so that the response of only one domain type becomes visible. By this, we can elucidate how the two domains at an a-c domain boundary contribute to the signal. As there are two relevant electric-field components E_x and E_z for the selected optical polarization orientation (Tab. 6.1), and two domain orientations a and c, the calculation splits up into four cases.

Figure 6.9 shows the modelling results obtained for $R = 150$ nm and $\phi = 5°$. For easy comparison, all images are plotted with the same color scale, already used in Fig. 6.8. The center image of Fig. 6.9 includes all contributions, while the outer images correspond to the four limiting cases as indicated. For the present set of parameters we find that for areas away from a-c domain boundaries the electro-optic response for both domain orientations stems only from the E_z component of the electric field. In contrast to this, very pronounced contributions stemming from the lateral field component E_x are found close to the a-c boundary. They are produced by the a domain as well as the c domain, with different magnitudes. They can be attributed to the special electric-field distribution at the boundary, which is characterized by an average lateral field component of significant magnitude across the optically addressed area.

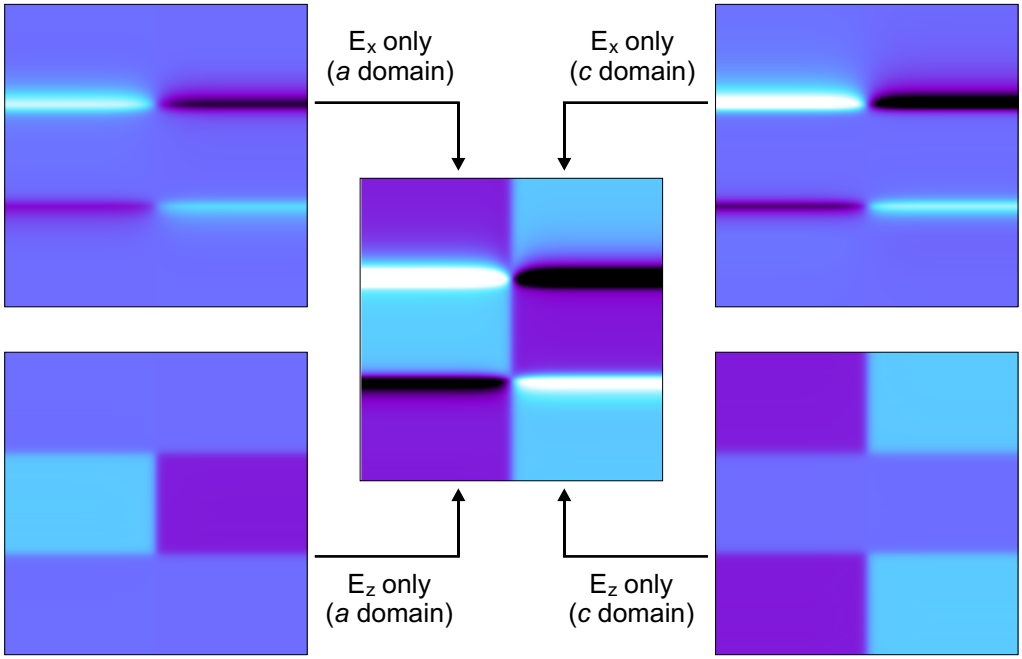

Fig. 6.9 *Contributions of the different domain types and electric-field components to the electro-optic response. The normal component of the electric field (E_z) determines the electro-optic response inside the domains, while lateral field components (E_x) give rise to significant contributions close to the a-c domain boundaries. This decoration of the domain walls stems from the electro-optic response of both the a and the c domains.*

The pronounced electro-optic response at the domain boundaries demonstrates that lateral components of the electric field can effectively contribute to the signal, provided that their average across the optically addressed volume does not vanish. This gets generally true for all domain areas – not only the boundaries – if the optical spot is shifted against the tip apex. Then, the electro-optic changes induced by the lateral components of electric-field distribution are weighted in an asymmetric way by the illumination profile. If these changes are probed by the chosen state of optical polarization, they will have an influence on the electro-optic response signal.

To show how a lateral shift of the spot modifies the signal for various orientations of the optical polarization (given by $\vec{u}(\phi)$), we arrange the results in a "matrix" shown in Fig. 6.10, with columns corresponding to different spot shifts $s_x = (-500, 0, 500)$ nm and rows corresponding to different angles $\phi = (-5, 0, 5)^\circ$. The underlying electric-field distribution was again calculated for a characteristic radius $R = 150$ nm and a tip-sample distance $d = 5$ nm.

The dependence on $\vec{u}(\phi)$ is a consequence of the probing of different elements of the $\boldsymbol{\eta}$ matrix as indicated in Tab. 6.1. For normal incidence ($\phi = 0^\circ$), only η_{xx} is probed, and for each domain type only one field component and the corresponding electro-optic coefficient play a role. If $\phi \neq 0$ is selected, then η_{zz}, η_{xz}, and η_{zx} are probed as well. Contributions stemming from diagonal elements (η_{xx}, η_{zz}) are affected only by the absolute value of ϕ, while contributions arising from off-diagonal elements (η_{xz}, η_{zx}) show an additional dependence on the sign of ϕ. All contributions to the electro-optic response can be associated with certain elements of the $\boldsymbol{\eta}$ matrix and the related electro-optic coefficients and field components.

For $\phi = 0^\circ$, the electro-optic response of the c domain area stems only from $\eta_{xx} = r_{113}E_z$. Its value decreases if a lateral spot shift s_x is introduced because of misalignment of the electrically and optically addressed areas. Since the electro-optic response of the a domain area stems from $\eta_{xx} = r_{333}E_x$, no signal is obtained in general for zero spot shift $s_x = 0$ because E_x has an average value of zero across the light spot. Only close to the domain boundaries is a significant value found because of the special electric-field distribution present here. If a spot shift $s_x \neq 0$ is introduced, either positive or negative values of E_x get favored by the "optical" weighting by the illumination, and therefore an electro-optic response arises across the whole a domain area. If s_x is replaced by $-s_x$, then also the favored sign of E_x is reversed and, hence, the electro-optic response changes its sign.

In case of $\phi \neq 0$, additional elements of $\boldsymbol{\eta}$ with a different dependence on ϕ are probed. For the c domain area, a small contribution of $\eta_{zz} = r_{333}E_z$ is expected, which is independent of the sign of ϕ. A much stronger contribution is provided by $\eta_{xz} = \eta_{zx} = r_{131}E_x$, which is connected with a lateral field component again. At zero spot shift $s_x = 0$, a noticeable contribution is therefore found only close to the domain boundary, as already discussed above for the case of an a domain. If a spot shift $s_x \neq 0$ is introduced, the electro-optic response will be altered across the entire c domain area. In accordance with the probed element $\eta_{xz} = \eta_{zx} = r_{131}E_x$, this contribution depends on the signs of ϕ and s_x.

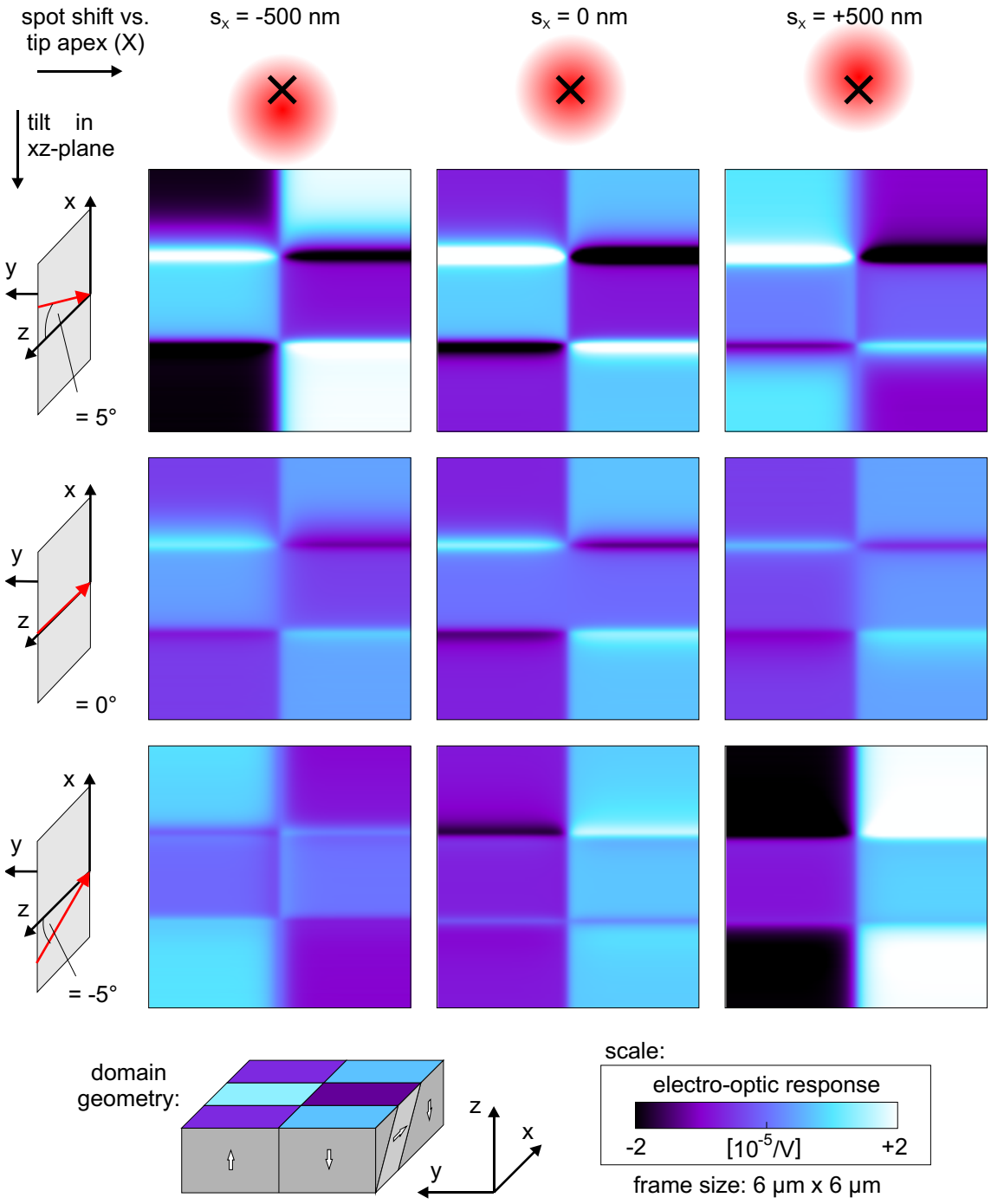

Fig. 6.10 *Effect of spot shift and tilt on electro-optic response imaging. Depending on the angle ϕ, different elements of the $\boldsymbol{\eta}$ matrix are probed. A spot shift s_x with respect to the tip apex leads to an effective contribution of elements connected with lateral field components.*

Therefore, the electro-optic response of a c domain can be enhanced or suppressed or even overcompensated compared to the case $\phi = 0°$. In the a domain area, $\eta_{zz} = r_{113}E_x$ and $\eta_{xz} = \eta_{zx} = -r_{131}E_z$ become probed additionally in case of $\phi \neq 0$. The first element depends on the lateral field component and behaves similar to the η_{xx} element in the case $\phi = 0$, while the second element depends also on the sign of ϕ and is connected with the normal field component E_z. It delivers the main contribution to the electro-optic response of the a domain area and decreases slightly with increasing absolute value of the spot shift, similar to the η_{xx} component in the c domain case.

In summary, different tilt angles ϕ and lateral spot shifts s_x give rise to various combinations of signal contributions, providing a variety of possible contrasts between the different domain orientations.

6.3.3 Application to ferroelectric hysteresis

The electric-field distribution produced by the scanning probe tip has a twofold function in case of the electro-optic inspection of ferroelectric switching characteristics. First, a sufficiently high electric-field component along the polar axis of the ferroelectric sample is required for domain switching. Second, the electric field strength is modulated by a much smaller value to probe the state of polarization averaged across the relevant sample volume. Both functions are provided by the same distribution of the electric field.

Switching occurs between the two antiparallel c domain orientations, that means ferroelectric polarization is always aligned normal to the sample surface in the switching experiments. Therefore, the normal component $E_\perp$ is the most important one for domain switching. For the c domain geometry, this is also the relevant field component for electro-optic polarization detection, at least as long as the tilting angle ϕ and lateral shifts s_x, s_y of the illumination are small. Since the experiments are performed at different tip-sample separations d, also the electric-field distribution was calculated for a number of distances. The results for the normal component $E_\perp$ of the electric field at the sample surface are shown in Fig. 6.11. The size and shape of the meniscus was kept constant with $R_{tip} = R_{men} = 150\,\mathrm{nm} \approx R_{contact}$, and the cylindrical symmetry was used again to reduce the computation to two dimensions.

The value of $E_\perp$ changes with the tip-sample separation d mainly close to the tip apex, while only a weak distance dependence is found farther away from the symmetry axis. Underneath the tip apex the electric field strength increases significantly with decreased distance d and reaches values in the order of 10^8 V/m at a bias voltage of 1 V.

For the description of an inverted domain underneath the tip apex a circularly shaped area with opposite state of polarization can be assumed. On the basis of the distribution of the probing electric field, the electro-optic response can be calculated for various radial sizes of the inverted domain area. The resulting electro-optic response was calculated for different tip-sample separations d and is plotted in Fig. 6.12.

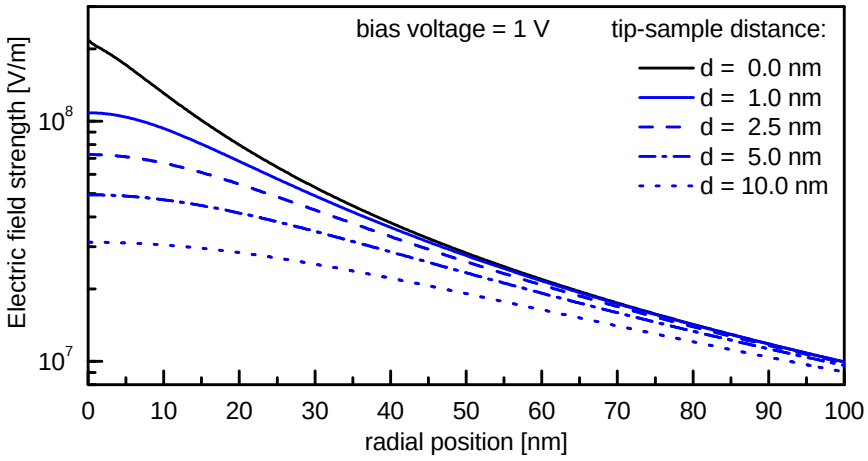

Fig. 6.11 *Radial distribution of the normal component $E_\perp$ of the electric field at the sample surface for various tip-sample separations d. $E_\perp$ varies significantly with d only at positions close to the tip apex. Here, the electric-field strength increases strongly with decreasing distance d.*

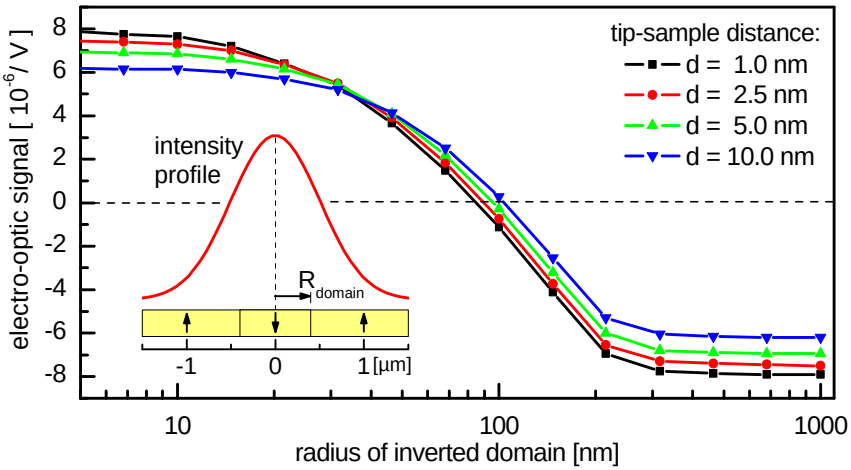

Fig. 6.12 *Electro-optic response as a function of domain radius for various tip-sample separations d. The electro-optic responses of oppositely oriented domains cancel each other for a radius of the inverted domain of $r_c \approx 100$ nm. With smaller distance d, increased electro-optic response in the uniformly oriented states and a decrease of r_c are found.*

The signals stemming from the inverted cylinder and from the surrounding non-inverted area compensate each other at a radius of the inverted domain of about 100 nm. This state corresponds to the points of coercive voltage or field in hysteresis plots. The radius of the inverted domain at which this state is reached increases slowly with tip-sample distance, which is a manifestation of decreased lateral resolution. Furthermore, the initial value of the electro-optic response decreases slightly with increasing distance due to the connected decrease of the field strength.

The modelling of hysteresis curves requires information about how large the inverted domain is at the sample surface for a certain applied voltage. The simplest assumption is that there is a certain threshold field strength E_{sw} and that switching takes place wherever E_{sw} is exceeded. Since the applied field strength scales linearly with the applied voltage U, the normal component $E_\perp(r)$ at a position r is given by

$$E_\perp(r) = E_\perp^{1\mathrm{V}}(r)\frac{U}{1\mathrm{V}}\,, \tag{6.16}$$

with $E_\perp^{1\mathrm{V}}(r)$ being the value calculated for 1 V. At the coercive voltage U_c, an inverted domain of radius r_c will produce zero electro-optic response signal. In accordance with the above assumption, we have $E_{sw} = E_\perp(r_c)$, leading to an expression for U_c given by

$$U_c = 1\mathrm{V}\cdot E_{sw}\ \cdot\ \frac{1}{E_\perp^{1\mathrm{V}}(r_c)}\,. \tag{6.17}$$

A plot of $1/E_\perp^{1\mathrm{V}}(r_c)$, which is directly proportional to U_c, vs. distance will allow a direct comparison between model and experiment with respect to the distance dependence of the coercive voltage. This is shown in Fig. 6.13 a) together with the electro-optic response at zero field for two variants of the model. The first variant assumes a constant meniscus size for all tip-sample separations as described above, while the second one assumes a slight decrease of the meniscus size with distance. Both models reflect qualitatively the general trends of decreased coercive voltage and increased electro-optic response with decreased tip-sample separation. But there are significant quantitative discrepancies between the model and the experimental results shown in Fig. 6.13 b). The experimental position scale with its large uncertainty (Secs. 3.3.2, 5.2) is only one source of the differences. That the experimental electro-optic response is weaker than the calculated one may be a consequence of nonideal tip properties, but may also result from nonuniform polarization of the probed volume as suggested by the lack of saturation in the hysteresis cycle. The experimental trends concerning the distance dependence are not reflected perfectly, indicating that the set of parameters and assumptions might be improper or the model too simplified. Beside the material properties themselves, especially the shape of the tip apex as well as the geometry of the meniscus formation are critical parameters. This is stressed by the results of the second model variant shown in Fig. 6.13 a), which assumes a meniscus size slightly decreasing with tip-sample distance. This improves the agreement between model and experiment significantly. Now, also the experimentally observed decrease of the coercive voltage at the largest distance investigated is reflected. It can be attributed to a decrease of the probed volume caused by the narrowing of the meniscus.

By comparing the scales on the left ordinates of Fig. 6.13 a) and b), referring to model and experiment, respectively, the threshold field for switching can be directly identified to be $E_{sw} \approx 4\cdot 10^8$ V/m. On the basis of this value, we can calculate the hysteresis curve by combining the model results for the electric field and the electro-optic response. Figure 6.14 a) shows the modelled hysteresis curve for a tip-sample distance of 1 nm. The dotted lines correspond to the curve expected if complete saturation of the switched polarization is reached. This is not the case if the bias voltage is limited to the range used

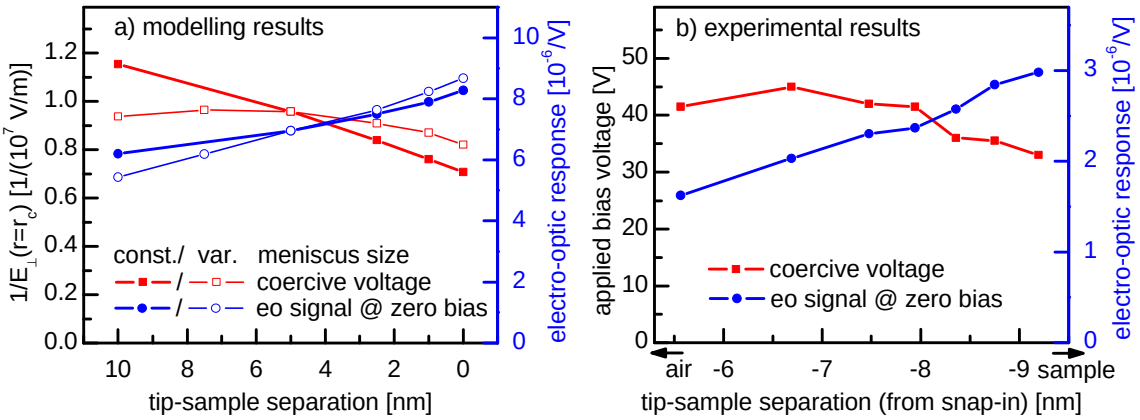

Fig. 6.13 *Modelling results (a) and experimental data (b) for the distance dependence of hysteresis measurements. The general trends of decreased coercive voltage and increased electro-optic response with smaller distance is reflected by the model already for a fixed meniscus size. Even better agreement is found for a meniscus size which decreases slightly with increasing distance. The discrepancies between the position scales can be attributed to the large error of the experimental scale, while the difference in the absolute numbers of the electro-optic response is probably related to tip and meniscus properties.*

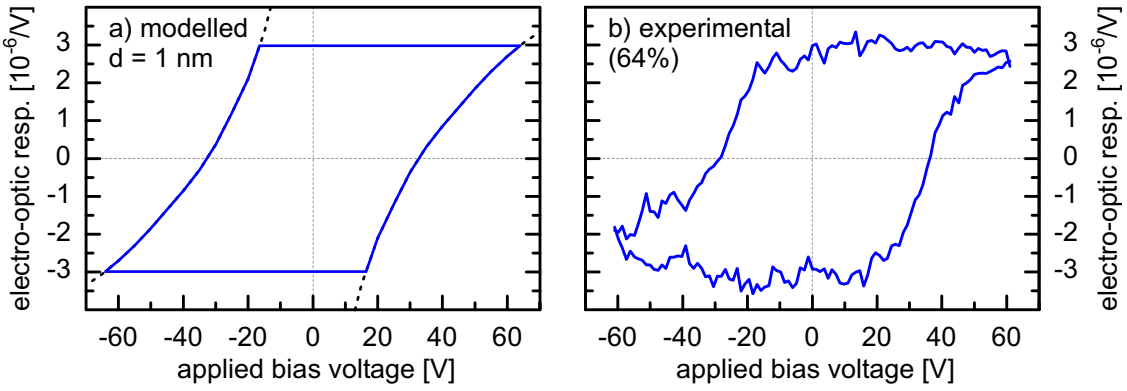

Fig. 6.14 *Comparison of modelled and experimental hysteresis curves. The modelled curve was calculated for $E_{sw} = 4.2 \times 10^8$ V/m. The dotted lines correspond to complete saturation of the hysteresis curve, which is not reached for the solid curve for which the bias voltage is limited to the experimental range. Good agreement between the modelled and experimental hysteresis curves is found.*

in the experiment, leading to the not completely saturated hysteresis curve indicated by the solid line. This also explains why the model overestimates the electro-optic response at zero bias, since the values given in Fig. 6.13 a) correspond to complete saturation. Overall, a good agreement is found between the modelled and experimental hysteresis curves shown in Fig. 6.14 a), b).

6.4 Conclusions

In contrast to most analytical approaches, our numerical framework for the electric-field calculation allows the incorporation of anisotropic dielectric materials in realistic model geometries. It is found that inside the sample the electric-field distribution is strongly influenced by the anisotropy of the sample as well as by the water adsorption layer and meniscus between the tip and the sample.

The results of the associated calculation of the electro-optic response are in good qualitative and quantitative agreement with the experimentally obtained image contrast. Furthermore, the model allows us to identify which electro-optic coefficients and electric-field components are probed and thereby facilitates a more detailed interpretation of the experimental results. It also explains some imaging artifacts, in particular those found at *a*-*c* domain boundaries.

Finally, the model is successful also in reproducing the experimental observations concerning the ferroelectric hysteresis measurements by electro-optic response. The modelling of the dependence on tip-sample separation and its comparison with the experiment allow us to assess some parameters which are not known directly from the experiment.

In conclusion, the presented framework for the modelling of the electro-optic response is a powerful tool for studying in advance possible improvements of the experimental setup and of the probes. Furthermore, this method can be applied to predict the electro-optical behavior of devices with micro- and nanostructured electrodes or domain patterns.

Chapter 7

Optical properties of a single 180° domain wall

In this chapter, we discuss the optical properties of single domain walls. First, a theoretical approach is discussed which allows us to calculate the refractive-index profiles of single domain walls. These predicted profiles are further used to estimate the effects being measurable experimentally. In the second part of this chapter, we describe the experiments that were performed in order to optically detect single domain walls, as well as their results.

7.1 Introduction

The optical properties of a specimen are determined by the electronic polarizabilities of its constituents. These polarizabilities depend not only on the constituents themselves, but also on the local electric fields. Since ferroelectric polarization is connected with the presence of local electric fields, the above dependence plays a very prominent role in the case of ferroelectrics, being important for the occurrence of birefringence, electro-optic response, and so on.

Across a ferroelectric domain wall, the polarization changes its orientation and therefore the local electric field is subject to a change, too. Within a limited interaction region around the domain wall, the local electric field differs not only in orientation, but also in magnitude. The optical properties are changed in this region because of the change of the local electric field. In this context, two questions arise: What is the magnitude of the change and what is the geometric extension of the region with modified optical properties at the domain wall?

For the magnitude of the change, one can develop a rough estimation, at least for the center of the domain wall. At this special point, the polarization-related electric field must vanish for symmetry reasons and therefore the optical anisotropy should be reduced. That means that birefringence is expected to be reduced within the domain wall. Also the resulting refractive index can be expected to be more or less comparable in magnitude to the case of vanishing ferroelectric polarization, as found in the paraelectric phase. For $BaTiO_3$ in this phase, a refractive index $n = 2.4$ is reported [85], a value that is also similar to the ordinary refractive index in the ferroelectric phase.

The extension of the region having modified properties is expected to be quite small, since the ferroelectric polarization can be reversed completely across only a few unit cells [12]. Nevertheless, much wider regions have been reported for some non-stoichiometric crystals. There, the domain wall region is characterized by long-range strain [86], attributed to non-stoichiometric defects [87]. For such a domain wall in lithium niobate ($LiNbO_3$), the modified optical properties have been directly measured, and from that the refractive-index profile could be deduced implicitly [87].

Here, we focus on ordinary 180° domain walls in barium titanate. In this case, the domain wall region is expected to be very small since it is assumed that the ferroelectric polarization is reversed completely within 2 nm [12, 19]. Therefore, we start the discussion with a theoretical analysis of the refractive-index profiles, followed by the modelling of effects accessible in the experiments, which are presented in the last parts of the chapter.

7.2 Theoretical description

The present model was developed and the calculations were done by Hassan Chaib, a guest scientist in our group. The application of the model to a variety of materials is published in detail in [18, 88, 89, 90], for example. The two most important ingredients of the model are the electronic polarizabilities of all ions as a function of the local electric field on the one hand, and the effective charges and positions of the ions on the other hand, as illustrated in Fig. 7.1. The polarizabilitiy of each individual ion under the influence of the local electric field $\vec{E}$ is derived by quantum mechanical perturbation theory. Since the

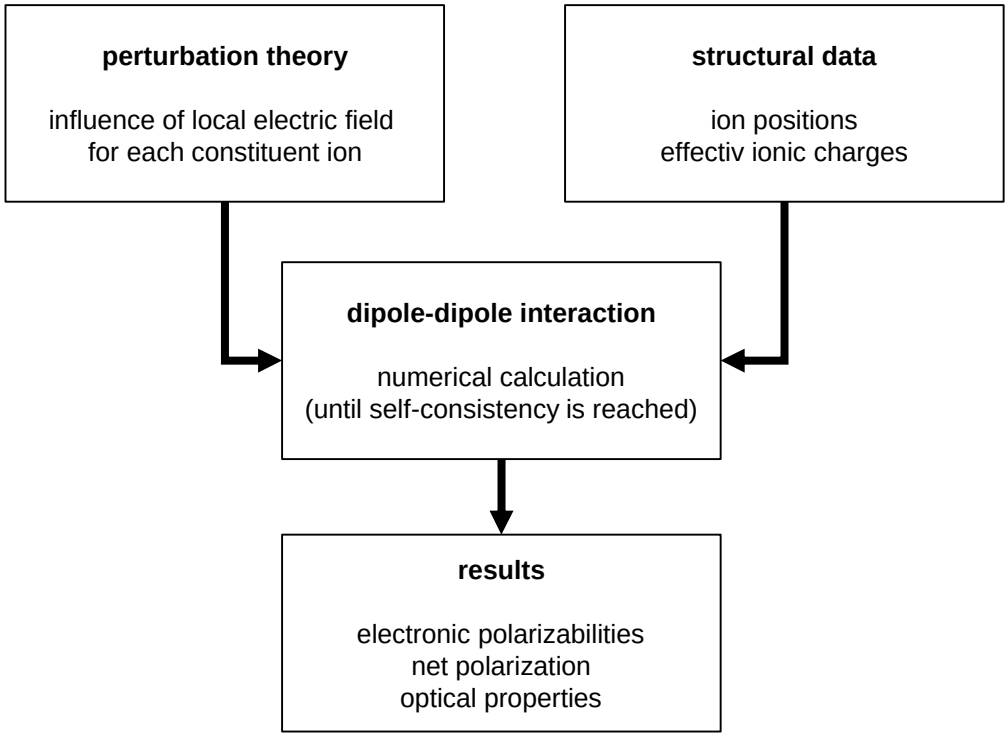

Fig. 7.1 *Steps for modelling the optical properties of $BaTiO_3$ domain structures.*

Hamiltonians of the present ions are too complex, the so-called "orbital approximation" is applied. This approximation considers an outer electron orbiting at the distance R around the core of the ion, which consists of the nucleus and the inner electrons with an effective charge Z, and leads to the Hamiltonian H_0 at zero field as noted in Eq. 7.1. The influence of the electric field $\vec{E}$ is introduced by H_1 (Eq. 7.2), leading to the resulting Hamiltonian H (Eq. 7.3) for the core-shell system in an external electric field.

$$H_0 = \frac{p^2}{2m} - \frac{Z}{R}e^2 \,, \tag{7.1}$$

$$H_1 = e\vec{E} \cdot \vec{R} \,, \tag{7.2}$$

$$H = H_0 + H_1 \tag{7.3}$$

In this theory, the perturbation, that means the influence of the local electric field, is introduced by a variational parameter λ. Therefore, it is assumed that the resulting wave function ψ in the presence of an external field can be written as

$$\psi\left(\lambda\right) = \left(1 + \lambda\, \vec{E} \cdot \vec{R}\right) \psi_0 \,, \tag{7.4}$$

where ψ_0 is the wavefunction for zero external field. The variational principle now claims that the expectation value of the energy $\langle\psi|H|\psi\rangle$ must be a minimum with respect to the variational parameter λ. This determines not only the parameter λ, but also the resulting wave function ψ.

From the wavefunction ψ_r of an orbital r in the presence of a local electric field $\vec{E}$, we may deduce the resulting dipole moment $\vec{p}_r^{\,e}$ and the electronic polarizability $\alpha_{kl,r}$ according to:

$$\vec{p}_r^{\,e} = \frac{(-e)\int \psi_r^* \vec{R} \psi_r \,\mathrm{d}v}{\int \psi_r^* \psi_r \,\mathrm{d}v} \,, \tag{7.5}$$

$$\alpha_{kl,r} = \frac{\partial p_{k,r}^e}{\partial E_l} = \alpha_{k,r}^* \left[\delta_{kl} - \theta_r^* \left(E^2 \delta_{kl} + 2\, E_k E_l\right)\right] \tag{7.6}$$

with

$$\alpha_{k,r}^* = \frac{4\left\langle x_3^2\right\rangle_r \left\langle x_k^2\right\rangle_r}{a_B} \quad , \qquad \theta_r^* = \frac{8\,\left\langle x_3^2\right\rangle_r^3}{a_B^2 e^2} \,,$$

and

$$\left\langle x_k^2\right\rangle = \int \psi_0^* x_k^2 \psi_0 \mathrm{d}v, \qquad a_B = \frac{\hbar^2}{me^2} \,.$$

We find then the polarizability $\alpha_{kl}(j)$ of the whole ion i by summing up the contributions of all orbitals r. Since the polarizabilities have to match the experimental value for the free ion at zero field, an anisotropic effective ionic charge of the outer shells of the ion is assumed and fitted to fulfill this condition. This determines the coefficients $\alpha_{k,r}^*$, θ_r^* and leads to the final expression for the polarizability of a constituent ion in the presence of a local electric field $\vec{E}$ [22]:

$$\alpha_{kl}(i) = \alpha^{exp}(i) \left[\delta_{kl} - \theta_k(i) \left(E^2(i)\delta_{kl} + 2E_k(i)E_l(i)\right)\right] \,. \tag{7.7}$$

The next step is to calculate the local electric field $\vec{E}$ at the position of each ion i. This field depends on the properties and the arrangement of all other ions of the crystal and can be expressed as a superposition of the fields produced by all dipoles $\vec{p}_j$ in the crystal [6]:

$$\vec{E}(i) = \vec{E}^{\,ext} + \sum_j \frac{3\,(\vec{p}_j\vec{r}_j)\,\vec{r}_j - \vec{r}_j^{\,2}\vec{p}_j}{r_j^5}\ . \tag{7.8}$$

The dipole $\vec{p}_j$ of an ion consists of two parts, an electronic part $p^{\mathrm{e}}_{k'}(j)$ and an ionic part $p^{\mathrm{i}}_{k'}(i,j)$ with the latter depending also on the effective charge $Z^*_{k'}(j)$ of the ion:

$$p_{k'}(i,j) = p^{\mathrm{e}}_{k'}(j) + p^{\mathrm{i}}_{k'}(i,j)\ , \tag{7.9}$$

$$\text{with} \qquad p^{\mathrm{e}}_{k'}(j) = \sum_{l=1}^{3} \alpha_{k'l}(j)\, E^{\mathrm{loc}}_l(j) \tag{7.10}$$

$$\text{and} \qquad p^{\mathrm{i}}_{k'}(i,j) = Z^*_{k'}(j)\, e\,(s_{k'}(j) - s_{k'}(i))\ . \tag{7.11}$$

The position $\vec{r}_i$ of each ion is calculated using structural data of the unit cell, including its size and the position of the ion within the unit cell, as well as the spontaneous ionic shifts $s_{k'}$ in the ferroelectric phase. These numbers are taken from the literature. Across the domain wall, the ionic shift makes a transition from positive to negative values. We assume that this transition can be described by the following function [19]:

$$s_{k'}(\tilde{m},j) = s^0_{k'}(j)\cdot\tanh\left(\frac{x(\tilde{m},j)}{2r_c}\right)\ , \tag{7.12}$$

where $\tilde{m}$ denotes the unit cell and $x(\tilde{m},j)$ is the distance of the ion j in this cell from the domain boundary. The parameter r_c characterizes the thickness of the domain wall and $s^0_{k'}(j)$ is the ionic shift far away from the boundary. The calculation of the local electric field is iterated until a self-consistent solution is found. As the final result, the polarization P_k is calculated by averaging the dipole moment across one unit cell of volume v, and the optical coefficients $\varepsilon^{\mathrm{opt}}_{kl'}$ are calculated as follows [19]:

$$P_k = \frac{1}{v}\sum_j \left(p^{\mathrm{e}}_k(j) + p^{\mathrm{ion}}_k(j)\right)\ , \tag{7.13}$$

$$\text{with} \qquad p^{\mathrm{ion}}_k(j) = Z^*_k(j)\, e s_k(j) \quad \text{, and} \qquad \varepsilon^{\mathrm{opt}}_{kl'} = \delta_{kl'} + 4\pi\frac{\partial P_k}{\partial E^{\mathrm{opt}}_{l'}}\ .$$

Figure 7.2 shows the results for the refractive-index profiles across a domain wall for different domain wall thicknesses r_c. For all these cases, the crystal shows three different refractive indices within the domain wall, that means the crystal gets biaxial while it is uniaxial far away from the domain wall. At the domain wall, the refractive index n_c, i.e. for light polarized parallel to the spontaneous polarization, exhibits the biggest change, followed by n_b. The refractive index n_a is left almost unchanged. The shape of the refractive-index profiles is symmetric with respect to the center of the domain wall and depends strongly on its width r_c. For the smaller values of r_c, the maximum of n_b at the center is flanked by two minima. With increasing r_c, the profile acquires a Gaussian-like shape.

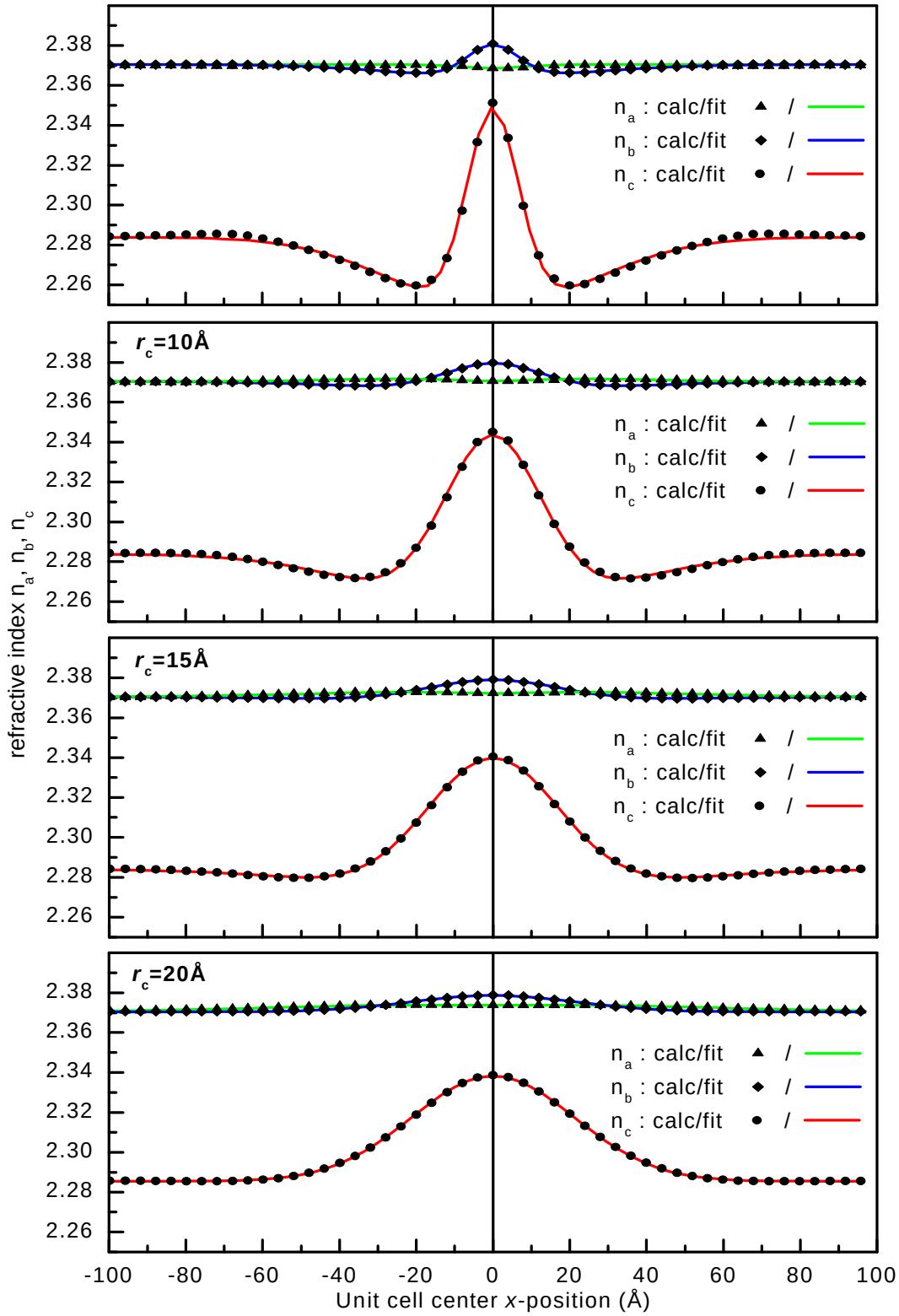

Fig. 7.2 *Modelled refractive index profiles for a 180° domain wall of $BaTiO_3$ for different values of the domain wall thickness parameter r_c. The index n_c experiences the biggest change, followed by n_b, while n_a remains almost unchanged. In case of smaller values of r_c, the profiles of n_c and n_b show a small decrease at the periphery of the wall, beside the stronger increase at the domain wall center. For larger r_c, the profiles get Gaussian-like.*

The refractive-index profiles, can be approximated by continuous functions, which will be used for estimations of experimental quantities in the following section. For this, the profiles of n_k^2 were fitted with up to two Gaussian function of different amplitude and width as stated in equation 7.14. The resulting functions are plotted in Fig. 7.2 and the corresponding fit parameters are listed in table 7.1.

$$n_k^2 = n_{k,bulk}^2 + A_{k,1} * exp(-2x^2/w_{k,1}^2) + A_{k,2} * exp(-2x^2/w_{k,2}^2) \tag{7.14}$$

Table 7.1 *Parameters of fit functions describing the refractive index-profiles for different values of the domain wall width r_c. The parameters correspond to Eq. 7.14.*

r_c [Å]	n_k	$A_{k,1}$	$w_{k,1}$ [Å]	$A_{k,2}$	$w_{k,2}$ [Å]
5	n_a	-0.0083	16.16	-	-
5	n_b	0.0762	13.35	-0.0282	51.20
5	n_c	0.4622	13.49	-0.1617	51.28
10	n_a	-0.0092	24.53	0.0106	59.34
10	n_b	0.0648	24.88	-0.0211	61.94
10	n_c	0.3991	25.12	-0.1228	61.25
15	n_a	-0.0063	28.38	0.0151	79.70
15	n_b	0.0519	34.21	-0.0111	71.38
15	n_c	0.3233	34.55	-0.0647	68.83
20	n_a	-0.0051	38.99	0.0209	95.10
20	n_b	0.0393	42.91	-	-
20	n_c	0.2439	42.23	-	-

7.3 Estimation of experimental effects

The key question for the application of near-field and confocal optical microscopy is the interaction between the confined optical source or probe and the inspected specimen. Measurable quantities are the reflected and transmitted light intensity, and in case of coherent light the phase of the transmitted light, provided that enough stability of the optical path is guaranteed.

In the next section, two experiments will be described, aiming at the detection of the modified optical properties of domain walls. Here, we present a theoretical estimation of the signal to be expected. Both experiments use a Gaussian-like intensity distribution of the probing light, which we describe by $I \sim \exp\left(-2r^2/w_b^2\right)$ with a beam waist parameter w_b.

The first experiment uses adapted SNOM cantilever probes as described in Sec. 3.2.4 for illumination, while the light power transmitted through the sample is detected. To estimate the expected effects, a beam waist parameter of about $w_b = 100\,\mathrm{nm}$ is assumed for these tips. The second experiment uses a diffraction-limited spot in a confocal setup to measure the effect of the domain wall on the reflected light power. In this case, a larger beam waist parameter of $w_b = 300\,\mathrm{nm}$ is assumed.

Figure 7.3 shows the relative change of the transmitted / reflected light power occurring when the illumination profile is moved across the domain wall. The calculation was done for the three cases of linear polarization along the crystal axes. Since the region of modified refractive index at the domain wall is much narrower than the beam waist, the domain wall acts like a probe of the optical field and details of the refractive-index profile can obviously not be resolved. Nevertheless, the amplitude and sign of the signal depend on the characteristics of the refractive-index profile. One observes the largest relative change for light polarized along the c axis. Therefore, we concentrate on that configuration.

The plots in Fig. 7.3 indicate that a relative sensitivity in the order of 10^{-4} is needed to detect these changes. Such a high static sensitivity is hard to achieve, especially in SNOM experiments for stability reasons. Therefore it is advisable to apply a modulation

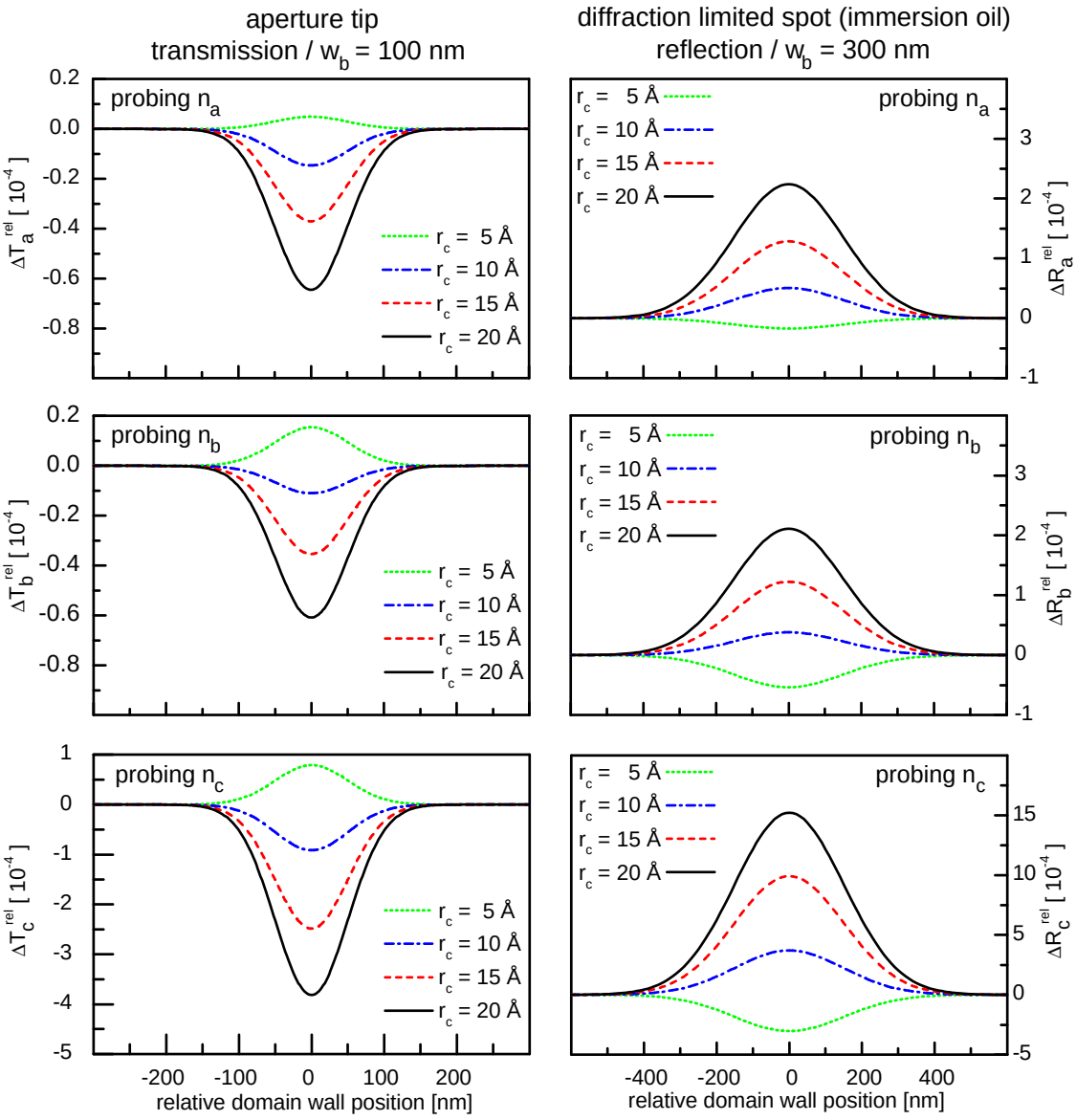

Fig. 7.3 *Intensity profiles for crossing a 180° domain wall with different optical probes. The effect on the transmitted / reflected light power is in the order of* 10^{-4}*. The largest effect is observed for light polarized along the c axis.*

technique to improve the sensitivity. Of course, one could try to use ferroelectric switching to let the domain wall appear and disappear periodically, but it is doubtful whether it is possible to control this mechanism precisely enough. Therefore, two other ideas were pursued in this work.

The first one is to modulate the position of the probe with respect to the domain wall. For oscillation amplitudes that are small compared to the beam waist w_b, the modulation of the detected light power corresponds to the derivative of the intensity profiles shown in Fig. 7.3. The result for light polarized along the c axis is plotted in Fig. 7.4 a) and b), and shows clear differences in magnitude and sign for different values of the domain wall thickness parameter r_c. The predicted relative power modulation is in the order of 10^{-6} per nm of oscillation amplitude.

The second idea concerning the application of modulation is based on the change of birefringence at the domain wall. If the polarization of the illuminating beam is oscillating between a and c axis orientation, one can obtain a modulated power connected to the difference of the refractive indices $\delta_{ac} = n_a - n_c$. At the domain wall, Fig. 7.2 predicts a change of this value and therefore a change of the modulation amplitude is expected as shown in Fig. 7.4 c) and d). Again, the curves show a clear difference in magnitude and sign for different values of r_c.

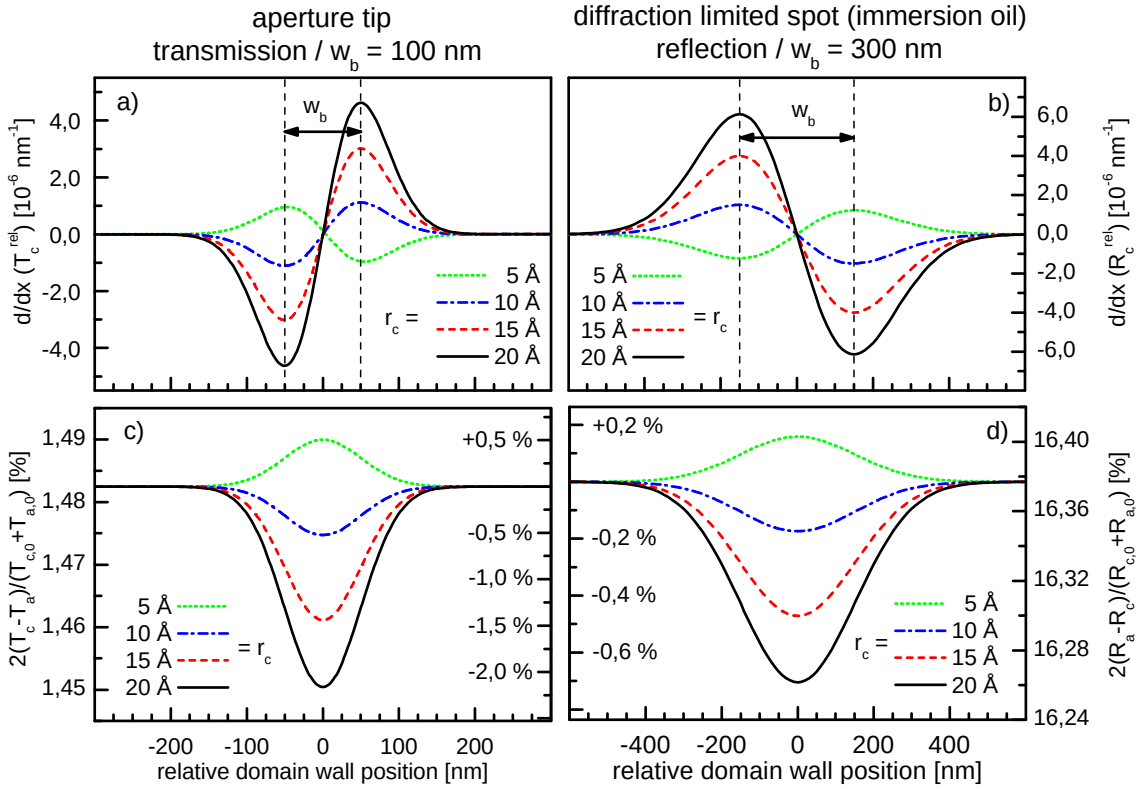

Fig. 7.4 *Estimations for modulation techniques at domain wall. The upper graphs show the effect of a position modulation of the probed volume with respect to the domain wall, while the lower graphs correspond to detection of birefringence by polarization modulation. For both techniques, the curves clearly distinguish different values of r_c.*

7.4 Experimental investigation of domain walls

At the beginning of the preceding section, it got clear that the refractive-index profiles of the domain walls cannot be resolved directly with the present optical probes. The expected effects, estimated by averaging the optical properties across the optically addressed area, are very small and therefore modulation techniques are utilized. To obtain the strongest effects, expected for optical polarization oriented along the c axis of the crystal, the c axis has to be parallel to the surface plane. Therefore, a domain wall within an a domain area is addressed in the following experiments.

7.4.1 Domain wall observation with an aperture tip

This experiment uses the adapted SNOM cantilever tips already successfully used for electro-optic domain imaging (Sec. 4.3.2). As described in Sec. 3.2.4, these probes are used like a standard fiber probe with the tip-sample separation being controlled by a tuning-fork-based shear-force feedback. The lateral oscillation of the tip end provides already the modulation of the probe position needed for the application of the first modulation technique mentioned in the previous section 7.3.

Before the optical properties of a domain wall can be inspected, a proper position on the sample has to be located. This is done with the same tip by taking an electro-optic-response image, shown on the left side of Fig. 7.5. There we can find an a domain area in the middle, while c domain areas are located at the top and the bottom of the image. Also antiparallel a and c domains can be identified. The region selected for domain wall inspection is marked by the rectangle.

The right side of Fig. 7.5 shows the result of domain wall inspection. The bright spot on top of the intensity map, which probably is caused by a topography feature, produces a clear signature in the demodulated signal as expected for a tip oscillation along the horizontal axis. This proves that the modulation detection is working properly. The demodulated signal is typically superimposed on a rather high offset that seems to be inherent to the setup, since it is also present without any sample mounted. It may be caused by some diaphragms along the optical path of the microscope. This offset has been subtracted from the signal. To calibrate the scale of the modulated light power we use some pronounced feature such as the bright spot at the top of the intensity image. With this calibrated scale, the oscillation amplitude can be estimated to be in the order of 1 nm.

The signature of the domain wall is expected to depend on the size of the light spot, which can be deduced from the resolution achieved in electro-optic response measurements of about 200 nm. Hence, we approximate the intensity distribution by a Gaussian with a beam waist parameter $w_b = 100\,\mathrm{nm}$. The expected signature of the domain wall is plotted in Fig. 7.4 a). The demodulated signal is expected to show a single oscillation centered at the domain wall with a spacing of w_b between minimum and maximum. Such a signature, is however not visible at the domain wall position in Fig. 7.5 due to noise, lack of stability,

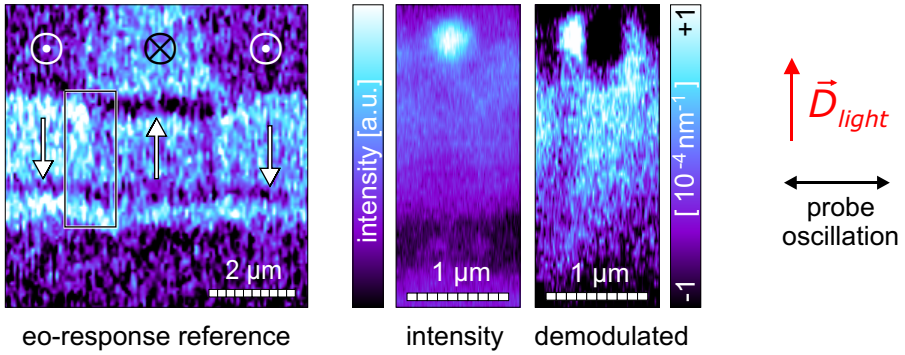

Fig. 7.5 *Domain wall inspection with an aperture tip, based on position modulation. The right part shows the measured dc intensity and the demodulated signal. The signature in the demodulated signal caused by the bright spot at the top of the intensity image provides a proof of principle and is also used for calibration. The inspected area is marked by the rectangle in the electro-optic-response reference image. No clear evidence for a domain wall signature can be found in the demodulated signal for the given noise and background.*

and background variations. The noise along a single scan line is in the order of $2.5 \cdot 10^{-5}$ nm^{-1}, about one order of magnitude larger than the estimated effect. Nevertheless, this experiment can at least give an upper limit to the optical effect of the domain wall: the effect cannot be larger than five times the effect predicted for $r_c = 20$ Å.

The second modulation technique mentioned in Sec. 7.3, is expected to be less prone to background, since it can operate with a stationary light spot. It is based on probing the birefringence by modulating the polarization orientation of the optical field, and therefore needs very good polarization control. However, the SNOM tips do not allow control of the polarization with sufficiently high quality. Indeed, the moderate polarization properties could be compensated to some extent by a sophisticated adjustment, but this makes the system very sensitive to slight drifts of the input polarization. Therefore, no useful results with polarization modulation could be obtained with such tips.

7.4.2 Domain wall observation with confocal microscopy

In these confocal-microscopy experiments, a diffraction-limited spot (Sec. 3.2.1) is used as optical probe. The main advantages are the higher available light power and excellent polarization control. On the other hand, the method provides neither any topography information nor the option of electro-optic response imaging, as no tip is present that could act as electrode. Therefore, optical information about domain orientation is limited to the classical contrast between *a* and *c* domain areas without the possibility of distinguishing antiparallel domains. Thus, it is necessary to find out the full domain structure of the inspected area in advance by a reference measurement. For this, we use piezoresponse force microscopy, providing information about topography and domain orientation as shown in Fig. 7.6. Both signal channels are combined to form a mask allowing us to identify the position of 180° domain walls in the following experiments.

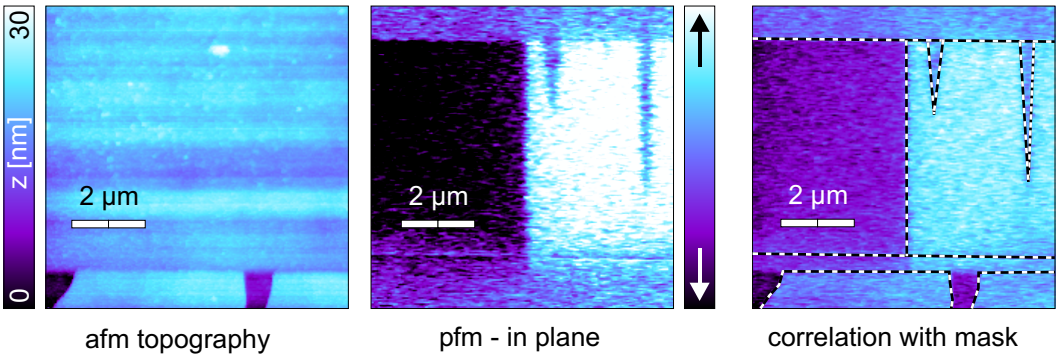

Fig. 7.6 *Reference image for confocal experiments taken by piezoresponse force microscopy. The topography signal as well as the in-plane PFM signal, which differentiate the a domains, are combined to build up a mask, allowing us to identify domain orientations in the following confocal experiments.*

To inspect the surface directly, the sample has to be flipped in the present setup. Now the sample surface previously characterized by PFM points directly to the microscope objective. The gap between the sample and the objective is filled with immersion oil to achieve the smallest spot possible. The immersion oil also reduces the refractive-index jump at the sample surface and increases therefore the relative sensitivity of the reflectance to refractive-index changes of the sample as listed in table 7.2.

Table 7.2 *The effect of immersion oil on the transmitted and reflected light intensity.*

medium	n_{medium}	T_a	T_c	$\frac{2(T_c-T_a)}{T_c+T_a}$	R_a	R_c	$\frac{2(R_c-R_a)}{R_c+R_a}$
air	1.0	83.1 %	84.3 %	1.47 %	16.9 %	15.7 %	-7.6 %
oil	1.5	94.7 %	95.5 %	0.81 %	5.3 %	4.5 %	-15.6 %

By the use of immersion oil the relative sensitivity to index changes is increased for reflected light, while it is decreased for transmitted light.

Position modulation of the optical probe is provided by a piezo-controlled mirror this time. The left side of Fig. 7.7 shows the measured reflected intensity. The normalized difference between the values obtained for a and c domain areas is about 16%, and agrees therefore well with the expected values in Tab. 7.2. There are also topography artifacts visible at the bottom c domain area, allowing us to identify the correct position of the mask. The demodulated signal shown on the right-hand side of Fig. 7.7 should correspond to the derivative of the intensity map along the horizontal direction. This is in fact true for the small spots and the topography-induced intensity changes at the top and at the bottom of the image and proves that the demodulation works correctly. As intended, a much higher sensitivity is achieved compared to the intensity image. However, the expected changes of

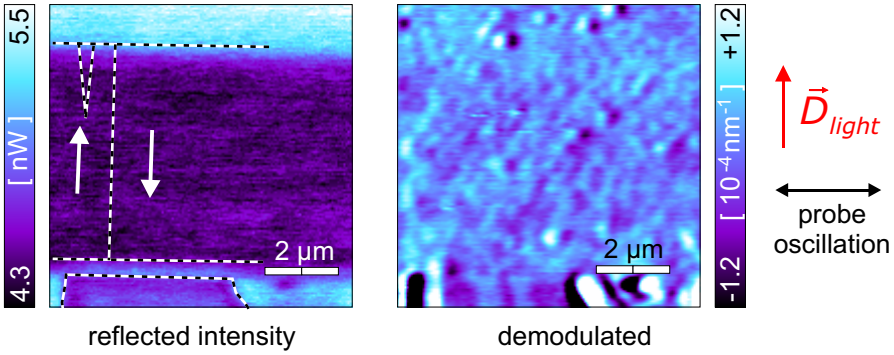

Fig. 7.7 *Domain wall inspection by confocal microscopy under horizontal position modulation. The left side shows the reflected intensity overlayed with the aligned mask. The relative difference in measured intensity between a and c domain areas is about 16% as expected from Tab. 7.2. The small spots at the top of the right image, showing the demodulated signal, demonstrate nicely the gain in sensitivity achieved by means of the modulation technique. Similar to the experiment using an aperture tip, no clear evidence for any domain wall signature can be found.*

the reflected light intensity near the domain wall, as estimated in Fig. 7.4 b), are again covered by much larger background variations in the order of $\pm 3 \cdot 10^{-5}\,\mathrm{nm}^{-1}$. This is in the same order of magnitude as for the aperture probe and therefore again only an upper limit to the effect produced by the domain wall can be given, which is six times larger than the effect predicted for $r_c = 20$ Å.

The confocal setup is much better suited for the method based on modulation of the polarization than the SNOM setup because of the excellent polarization control offered by the diffraction-limited spot. Yet, a small polarization dependence of the optical path is still present, as illustrated in Fig. 7.8, which gives rise to an additional intensity modulation. To get rid of this disturbance, we adjust the polarization such that it is modulated between two orthogonal states of equal intensity (Fig. 7.8). Then only an intensity modulation at the double frequency is left, which is suppressed by the lock-in amplifier. The sample has to be aligned accordingly (see Fig. 7.8).

The right side of Fig. 7.9 shows a large-area scan not only used to locate the sample area depicted in Fig. 7.6, but also to find the correct geometrical transformation for the mask. This transformation, illustrated on the left side of Fig. 7.9, is not a simple rotation because of a small difference of the length scales and a small non-orthogonality of the x and y axis of the scanner. The image of the reflected intensity itself, recorded with a fixed optical polarization parallel to the ferroelectric polarization of the *a* domain areas, shows nice contrast between *a* and *c* domain areas. The normalized difference between the intensities reflected from *a* and *c* domain areas of about 9% is again in fair agreement with the expected values listed in Tab. 7.2.

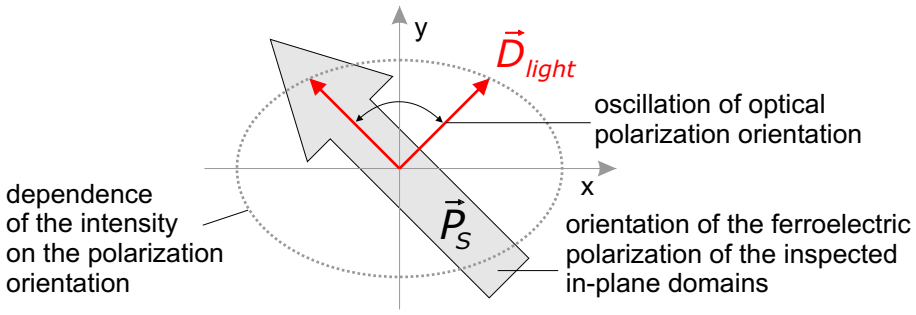

Fig. 7.8 *Adjustment of the optical polarization and sample alignment. The extreme orientations reached by the optical polarization during each modulation cycle are adjusted to be symmetric with respect to the polarization dependence of the setup. This way, the intensity modulation caused by the setup is shifted to the double frequency. Finally, the sample is reoriented with respect to the optical polarization such that the maximum amount of birefringence is detected.*

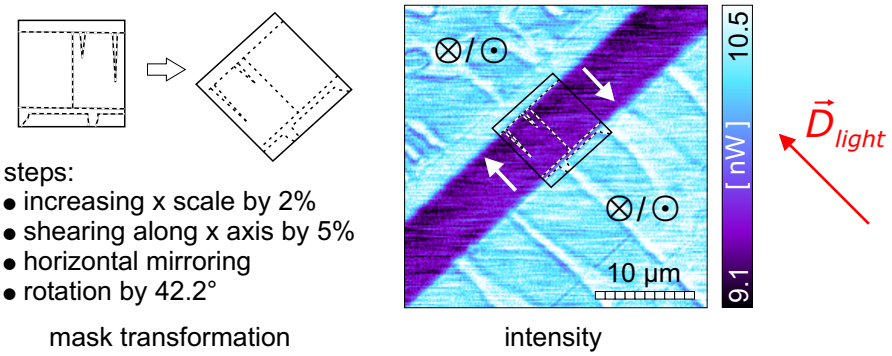

Fig. 7.9 *Locating of the domain structure and image transformation. Due to nonideal scanner properties and the rotation of the sample, the mask needs to be transformed geometrically. This is done by correlation of large-area scans, also used to locate the reference area.*

The result for active polarization modulation is shown in Fig. 7.10. The demodulated amplitude, reflecting the amount of birefringence, distinguishes nicely between *a* and *c* domain areas. The border between these domain types as well as the topography effects visible in the bottom left corner are used to position the mask in the right image of Fig. 7.10, which shows the same data but with higher contrast. 100% of modulation is assigned to the averaged amount of birefringence measured across the *a* domain area. Local variations of the modulation amplitude not related to the domain walls are observed to be in the order of about 4%. This is again much larger than the changes expected at the domain wall (Fig. 7.4 d). Also here, we can thus only state that the domain wall effect cannot be larger than a certain limit, namely five times the value of 0.7% found in the simulation for $r_c = 20$ Å.

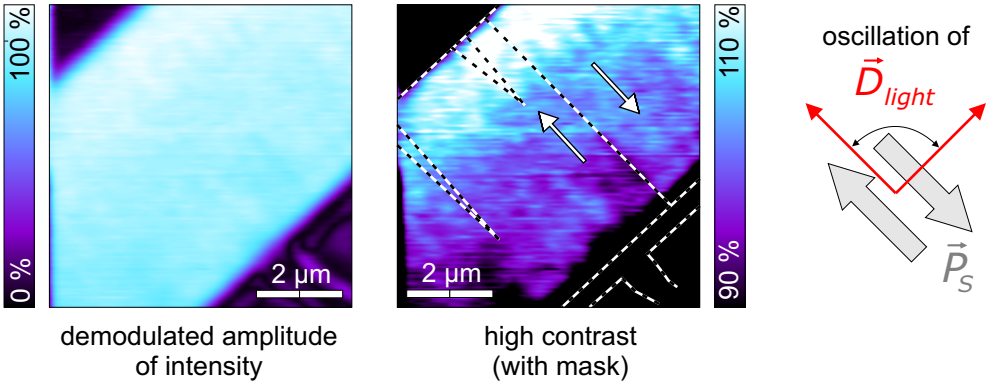

Fig. 7.10 *Domain wall inspection by confocal microscopy with polarization modulation. The maps of the modulation amplitude separates nicely between c domain (0%) and a domain (100%) areas. The right image shows the same data scaled to high contrast and is expected to show a small decrease or increase of modulation amplitude at domain walls (Fig. 7.4). A possible signal of this kind is, however, completely swamped by local variations in the order of 4% that are not related to domain walls. Therefore, only an upper limit to the influence of the domain wall can be derived.*

7.5 Conclusions

Here, we have presented the results of optical investigations of 180° ferroelectric domain walls in barium titanate single crystals at room temperature. Their optical properties are expected to differ from those found well inside a ferroelectric domain. The expected amount and the spatial extension of this modification were deduced from theory by considering the electric-field-dependent electronic polarizabilities as well as the arrangement in space of all constituent ions. The resulting refractive-index profiles (Fig. 7.2) are characterized mainly by changes of the extraordinary refractive index within a region of ±5 nm around the domain wall position. As expected from a simple picture, assuming a vanishing electric field at the domain wall center position, the birefringence is decreased at this location and the refractive index gets comparable to the one of barium titanate in its paraelectric phase.

The modification of the refractive index is localized to a much smaller volume than the volume addressed by the available optical probes. Therefore, the effect of the domain wall is averaged out to a large extent in the optical signal (Fig. 7.3), so that only a very small effect in the order of 10^{-4} remains, too small to be detected in a static measurement. Therefore, two different modulation techniques were developed to gain enough sensitivity (Fig. 7.4).

The experiments make use of two different kinds of optical probes in combination with the two modulation techniques (Figs. 7.5, 7.6, 7.10). Unfortunately, the sensitivity was still not high enough to reveal domain wall effects, either due to noise or due to background effects which may be connected with the quality of the sample. All experiments performed reach a sensitivity that would need to improved by a factor of five to detect the effects expected for $r_c = 20$ Å. Therefore, no proof or disproof of the theory was achieved.

To find evidence for the predicted refractive-index profiles, experiments with an extreme confinement of the optical probe to a few nanometers should be developed. Experiments using scattering-SNOM [91] techniques have the potential to achieve such a high resolution, but they are still lacking the sensitivity needed to detect small changes of the refractive index. Another option might be to study collective effects produced by a sample containing many domain walls [92].

Chapter 8

Conclusions and outlook

8.1 Summary

The further development of optical technology needs smart optical materials, structures, and devices. Ferroelectrics are one promising class of materials because of their outstanding optical properties. Their large optical anisotropy as well as their large values of elasto-optic, electro-optic, and nonlinear-optic coefficients are already very important for applications. Yet, artificial domain structures play a minor role so far, although they show a large potential for the application in smart structures and devices. In this context, the inspection of the optical properties of ferroelectric domains and domain walls at the very local scale is of great interest.

Within this work, the electro-optic properties of differently oriented domains as well as the refractive-index profile across a single domain wall in single-crystalline barium titanate were analyzed. These crystals exhibit a convenient number of domain orientations and their bulk properties are well documented in the literature, so that a complete set of parameters required for modelling is available.

For local probing of the electro-optic effect, conductive optical fiber tips were used as local electrodes. They provide strongly localized electric fields, thereby confining the probed volume, so that no additional optical confinement is required in general. By this, the local electro-optic response can be measured, which allowed us to identify the orientation of all occurring domains. By controlling the angular distribution and the polarization orientation of the probing light, various electro-optic constants can be probed.

Electro-optic response was also used to monitor the state of ferroelectric polarization during ferroelectric switching and domain growth. Ferroelectric hysteresis curves were obtained by applying a cyclic bias field via the same tip as also used for the electro-optic probing. Because of the limited confinement of the optical field, also the domain growth can be tracked up to a diameter of 400 nm of the switched domain.

The method of local electro-optic probing was extended to operate also at higher frequencies by utilizing a modulated light source. With this setup, the local electro-optic response

as well as ferroelectric hysteresis were examined in different frequency regimes. Similar principles can be applied for time-resolved measurements of switching and domain wall movement based on advanced pulsed laser sources.

The experimentally obtained results of electro-optic domain imaging and hysteresis measurement were supported in detail by numerical modelling. This provided very good qualitative and quantitative understanding of the experimental results. Additionally, parameters, not directly given for our experiment, were assessed by comparing the experimental results with those of the model.

Concerning the optical properties of single domain walls, our theoretical analysis suggests that the weak effects to be expected could be measured, provided that the sensitivity and resolution are pushed to extreme values. The improvements achieved in the present work turned out to still be insufficient. Nevertheless, an upper limit to the change of the optical properties at domain walls could be established, which is five times larger than the theoretically predicted value.

8.2 Outlook

The methods developed for electro-optical domain imaging and hysteresis measurements are a promising tool for the optical characterization of artificial domain structures, as used for smart optical devices, as well as for time-resolved measurements of domain nucleation and growth. In this context, local electro-optic-response probing could benefit from novel probe types. In particular, concerning the replacement of the structure acting as local electrode there are interesting options such as individually addressed nanoparticles or carbon nanostructures. The possible advantage of such structures can easily be evaluated in advance within the framework of the model developed in this work, which could also be applied for the analysis of optical devices containing nanostructured domain patterns or electrodes. Finally, the predicted refractive-index profiles of ferroelectric domain walls could be used as a passive element in such smart optical devices.

Appendix

A.1 Electro-optic properties of inversely poled domains

The modelling of electro-optic-response measurements requires the description of the changed optical properties not only of a and c domain areas, but also of inversely poled a and c domains. These inverted domains can be described in terms of simple mirror transformations of the crystal coordinates. These mirror operations are characterized by a mirror plane being normal to the ferroelectric polarization. If an initial polarization orientation along the z axis in case of a c and along the x axis in case of an a domain is assumed, then the according mirror transformations I_c and I_a are given by

$$I_c = I_c^{-1} = \begin{pmatrix} 1 & 0 & 0 \\ 0 & 1 & 0 \\ 0 & 0 & -1 \end{pmatrix} \quad \text{and} \quad I_a = I_a^{-1} = \begin{pmatrix} -1 & 0 & 0 \\ 0 & 1 & 0 \\ 0 & 0 & 1 \end{pmatrix} . \tag{A.1}$$

For an inverted domain, the electric-field components (E_1, E_2, E_3) in the crystal frame of reference are connected with the field components (E_x, E_y, E_z) in the reference frame of the model by

$$(E_1, E_2, E_3)^\top = I_c \cdot \vec{E} = (E_x, E_y, -E_z)^\top \tag{A.2}$$

in case of a c and

$$(E_1, E_2, E_3)^\top = T \cdot I_a \cdot \vec{E} = (-E_z, E_y, -E_x)^\top \tag{A.3}$$

in case of an a domain area with T transforming to the crystal coordinates as defined for an a domain.

To describe the electro-optic response of inversely poled domains we have to transform also the η matrices. In case of a c domain, the η matrix of a non-inverted orientation was found in Sec. 6.3.1 to be

$$\eta_c = \begin{pmatrix} \frac{1}{n_o^2} + r_{113}^{\text{eff}} E_3 & 0 & r_{131}^{\text{eff}} E_1 \\ 0 & \frac{1}{n_o^2} + r_{113}^{\text{eff}} E_3 & r_{131}^{\text{eff}} E_2 \\ r_{131}^{\text{eff}} E_1 & r_{131}^{\text{eff}} E_2 & \frac{1}{n_e^2} + r_{333}^{\text{eff}} E_3 \end{pmatrix} , \tag{A.4}$$

with $(E_1, E_2, E_3)^\top = (E_x, E_y, E_z)^\top$. The resulting η matrix for an inverted c domain $\eta_{\bar{c}}$ is then given by

$$\eta_{\bar{c}} = I_c^{-1} \cdot \eta_c \cdot I_c = \begin{pmatrix} \frac{1}{n_o^2} + r_{113}^{\text{eff}} E_3 & 0 & -r_{131}^{\text{eff}} E_1 \\ 0 & \frac{1}{n_o^2} + r_{113}^{\text{eff}} E_3 & -r_{131}^{\text{eff}} E_2 \\ -r_{131}^{\text{eff}} E_1 & -r_{131}^{\text{eff}} E_2 & \frac{1}{n_e^2} + r_{333}^{\text{eff}} E_3 \end{pmatrix}, \tag{A.5}$$

with $(E_1, E_2, E_3)^\top = (E_x, E_y, -E_z)^\top$.

The comparison of Eq. A.4 and Eq. A.5 reveals that the electro-optical properties of an inverted c domain area can be described in terms of the non-inverted one by simply altering the signs of all three electric-field components.

The same result can be derived for inverted a domains. In Sec. 6.3.1 the η matrix of a non-inverted a domain was found to be

$$\eta_a = \begin{pmatrix} \frac{1}{n_e^2} + r_{333}^{\text{eff}} E_3 & r_{131}^{\text{eff}} E_2 & -r_{131}^{\text{eff}} E_1 \\ r_{131}^{\text{eff}} E_2 & \frac{1}{n_o^2} + r_{113}^{\text{eff}} E_3 & 0 \\ -r_{131}^{\text{eff}} E_1 & 0 & \frac{1}{n_o^2} + r_{113}^{\text{eff}} E_3 \end{pmatrix}, \tag{A.6}$$

with $(E_1, E_2, E_3)^\top = (-E_z, E_y, E_x)^\top$. The η matrix of an inverted a domain $\eta_{\bar{a}}$ is

$$\eta_{\bar{a}} = \left(I_a^{-1} \, \eta_a \, I_a \right) = \begin{pmatrix} \frac{1}{n_e^2} + r_{333}^{\text{eff}} E_3 & -r_{131}^{\text{eff}} E_2 & r_{131}^{\text{eff}} E_1 \\ -r_{131}^{\text{eff}} E_2 & \frac{1}{n_o^2} + r_{113}^{\text{eff}} E_3 & 0 \\ r_{131}^{\text{eff}} E_1 & 0 & \frac{1}{n_o^2} + r_{113}^{\text{eff}} E_3 \end{pmatrix}, \tag{A.7}$$

with $(E_1, E_2, E_3)^\top = (-E_z, E_y, -E_x)^\top$.

Again, electro-optic properties of inverted domains can be described like those of non-inverted ones by altering the signs of all three electric-field components.

A.2 Modelling Kelvin probe force microscopy

In this work we use a numerical treatment for the electric-field calculation in complex geometries, which allows us to incorporate also anisotropic dielectric media (Sec. 6.2). The results are successfully applied for the modelling of electro-optic response measurements (Sec. 6.3). Further confirmation for the method used is provided by the successful application to the modelling of Kelvin probe force microscopy. There, an oscillating AFM cantilever, being in non-contact operation, senses local potential differences between tip and sample surface via the electrostatic forces. The experimental setup can be configured to minimize either the electrostatic force or its gradient by applying a certain bias voltage between the cantilever and the sample back electrode, as reported in [93, 94]. The electrostatic interaction is singled out by superposing a modulation voltage on the applied bias voltage. The resulting electro-static force will lead to a direct bending of the cantilever, which produces a deflection signal at the modulation frequency of given amplitude (AM signal). Additionally, the applied modulation voltage alters the cantilever resonance frequency via the electrostatic force gradient. This leads to a frequency-modulated (FM) signal in the cantilever response. Depending on which of these two signals is nullified by the bias voltage adjustment, either the electrostatic force (for the AM signal) or the force gradient (for the FM signal) is minimized by the Kelvin bias voltage controller.

In order to model the Kelvin probe experiment, the model geometry described in Sec. 6.2.2 is modified by replacing the sample by a surface with a given potential distribution. Additionally, the radius and the cone angle of the tip are adapted to the situation of the real AFM experiment. For each sample configuration, the model calculations are run for a series of distances d and tip potentials U_{tip} . From the resulting electric-field distribution, finally the force $\vec{F}$ or its gradient $\partial\vec{F}/\partial d$ has to be determined.

The force along the sample surface normal is given by the first derivative of the total field energy W with respect to d. W can be obtained by integrating $\frac{1}{2}\varepsilon_0 E^2$ across the entire model volume. Then the force is given by

$$F = \frac{\partial}{\partial d} W = \frac{\partial}{\partial d} \cdot \frac{1}{2} \int \varepsilon_0 E^2 d^3\vec{r}\,. \tag{A.8}$$

Alternatively, it is useful to express directly the electro-static force acting on the cantilever, since the numerical accuracy is increased if no extra differentiation step is required.

As illustrated in Fig. A.1, a surface charge σ is formed at the electrode to compensate the electric field inside the metal. The field E_{sc}, produced by σ at the surface, can be directly derived from the integral formulation of Maxwell's equations [95] and is given by

$$E_{sc} = \frac{\sigma}{2\varepsilon_0}\,. \tag{A.9}$$

The field E_{sc} of the surface charge not only compensates the external electric field E_{ext} within the metal, but also contributes to the total electric field $E = E_{ext} + E_{sc}$ in the free space as illustrated in Fig. A.1.

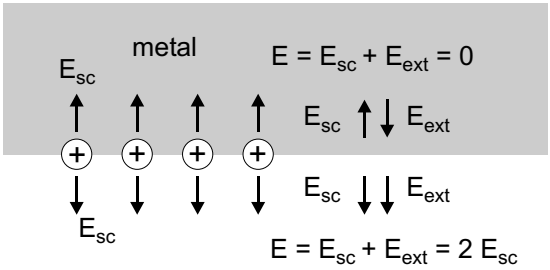

Fig. A.1 *Electrostatic force acting on a metal electrode. An external electric field E_{ext} induces a surface charge distribution σ such that the field E_{sc} produced by σ makes the total electric field E vanish inside the metal. On the outside surface, E_{sc} and E_{ext} contribute with equal parts to the total field E.*

The electrostatic force $d\vec{F}$ acting on the surface charges is given by the electric field E_{ext} of the external sources only and points along the surface normal $\vec{n}$. For a surface element dA it is given by

$$\begin{aligned} d\vec{F} &= E_{ext}\,\sigma\,dA\,\vec{n} \\ &= \tfrac{1}{2}E\,\sigma\,d\vec{A} \\ &= \tfrac{1}{2}\varepsilon_0\,E^2\,d\vec{A}\,. \end{aligned} \tag{A.10}$$

The total force $\vec{F}$ is finally obtained by an integration across the metal surface by

$$\vec{F} = \int \frac{1}{2}\varepsilon_0\,E^2\,d\vec{A}\,. \tag{A.11}$$

In both approaches for the electrostatic force calculation, the force gradient, which is required for modelling of the FM method, is obtained by the additional differentiation with respect to d.

First, we consider a surface with a sharp boundary between two areas of different surface potential and compare experimental data with results of the modelling for the AM and FM operation. The experimental data was obtained on a Au(111) sample surface covered by half a monolayer of potassium chloride (KCl) [93]. This provides a suitable test structure as KCl forms compact islands which extend laterally over several microns. The surface potential difference between the Au(111) and KCl surfaces is found to be 906 mV in the experiment. Therefore, we model the surface as consisting of two regions with potentials +0.45 V and -0.45 V and we assume that the potential makes a sharp transition between the two values within only 2 nm. The tip radius is set to $R = 15$ nm, which is the value stated in the datasheet, and a tip-sample separation of $d = 3 \ldots 8$ nm is chosen, comparable to the experiment.

The measured and the modelled Kelvin voltages across the boundary are shown in Fig. A.2 for AM and FM Kelvin operation. The modelling reflects very well the experimental behavior for both Kelvin modes. Especially the difference between the two operation

modes with regard to the approach towards saturation is reproduced. For the FM method, saturation at the correct level of ±0.45 V is reached within the first 50 nm on either side of the step, while for the AM method the saturation level is not reached within the displayed distance of 400 nm. Hence, it becomes clear that the FM method provides higher resolution and is much better suited for quantitative studies.

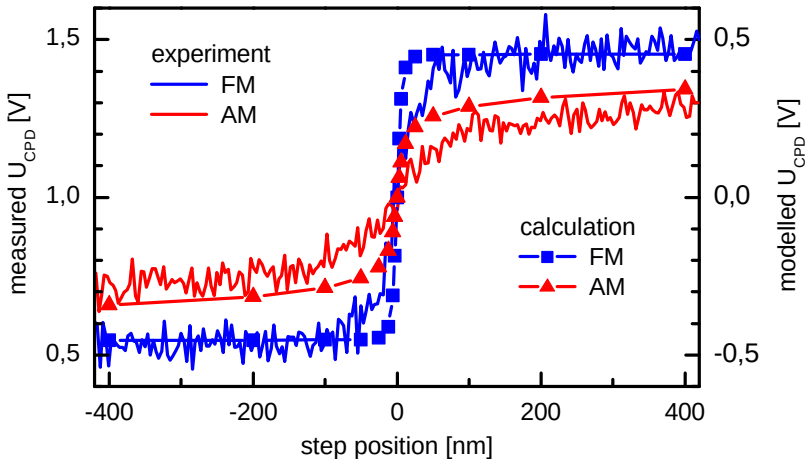

Fig. A.2 *Measured and modelled resolution of AM and FM Kelvin probe force microscopy at a step-like transition of the surface potential. The model results reflect very well the spatial dependence of the Kelvin potential for both modes of operation. It is found that only the FM mode is able to measure the correct potential near the sharp transition.*

Similar agreement between experiment and model is found for the the dependence of the Kelvin potential on the tip-sample separation. Furthermore, also the influence of the tip radius on the Kelvin potential can be investigated [94]. These results show that the present method of modelling provides useful support in selecting the proper Kelvin method and finding the best tip shape for a certain structure under investigation.

Bibliography

[1] BMBF VDI-Technology Center. Optical technology "made in germany". Agenda of Light, 2000. www.optischetechnologien.de.

[2] L. E. Cross and R. E. Newnham. *Ceramics and Civilization, Volume III, High-Technology Ceramics - Past, Present, and Future*, chapter History of Ferroelectrics, page 289. The American Ceramic Society, Inc., 1987.

[3] G. H. Haertling. Ferroelectric ceramics: History and technology. *J. Am. Ceram. Soc.*, 82(4):797, 1999.

[4] C. A. Randall, R. E. Newnham, and L. E. Cross. History of the first ferroelectric oxide, batio$_3$. The American Ceramic Society, Electronics Division http://209.115.31.62/electronicsdivision.

[5] M. E. Lines and A. M. Glass. *Principles and Applications of Ferroelectrics and Related Materials*. Oxford University Press, 2001.

[6] Ch. Kittel. *Einführung in die Festkörperphysik*. R. Oldenbourg Verlag, 12. edition, 1999.

[7] L. Carlsson. Crystal structure changes in batio$_3$. *Acta Cryst.*, 20:459, 1966.

[8] W. J. Merz. The electric and optical behavior of batio$_3$ single-domain crystals. *Physical Review*, 76(8):1221, 1949.

[9] Y. Xu. *Ferroelectric Materials and Their Applications*. North-Holland, 1991.

[10] S. Bauer. Poled polymers for sensors and photonic applications. *J. Appl. Phys.*, 80(10):5531, 1996.

[11] V. K. Wadhawan. *Introduction to ferroic materials*. Gordon and Breach, 2000.

[12] J. Padilla, W. Zhong, and D. Vanderbilt. First-principles investigation of 180° domain walls in batio$_3$. *Phys. Rev. B*, 53(10):5969, 1996.

[13] B.A. Strukov and A.P. Levanyuk. *Ferroelectric Phenomena in Crystals*. Springer-Verlag, 1998.

[14] *Neue Materialien für die Informationstechnik*. Schriften des Forschungszentrums Jülich - Materie und Material / Matter and Materials, Band 7. Forschungszentrum Jülich GmbH, Institut für Festkörperforschung, 2001.

[15] M. Veithen, X. Gonze, and Ph. Ghosez. Nonlinear optical susceptibilities, raman efficiencies, and electro-optic tensors from first-principles density functional perturbation theory. *Phys. Rev. B*, 71:125107, 2005.

[16] B. G. Potter Jr., V. Tikare, and B. A. Tuttle. Monte carlo simulation of ferroelectric domain structure and applied field response in two dimensions. *J. Appl. Phys.*, 87(9):4415, 2000.

[17] E. B. Tadmor, U. V. Waghmare, G. S. Smith, and E. Kaxiras. Polarization switching in pbtio$_3$: an ab initio finite element simulation. *Acta Mater.*, 50:2989, 2002.

[18] H. Chaib, D. Khatib, and W. Kinase. Theoretical study of refractive indices, birefringence and spontaneous polarization of batio$_3$ and knbo$_3$ in the tetragonal phase. *Phys. Stat. Sol. (B)*, 214:453, 1999.

[19] H. Chaib, T. Otto, and L. M. Eng. Theoretical study of ferroelectric and optical properties in the 180° ferroelectric domain wall of tetragonal batio$_3$. *Phys. Stat. Sol. (b)*, 233 (2):250, 2002.

[20] H. Chaib, F. Schlaphof, T. Otto, and L.M. Eng. Electric and optical properties of the 90° ferroelectric domain walls in tetragonal barium titanate. *Journal of Physics: Condensed Matter*, 15:8927, 2003.

[21] H. Chaib, L.M. Eng, and T. Otto. Dielectric polarization and refractive indices of ultrathin barium titanate films on strontium titanate single crystals. *J. Phys.: Condens. Matter*, 17:161, 2005.

[22] H. Chaib, A. Toumanari, D. Khatib, and W. Kinase. Theoretical study of temperature dependence of spontaneous polarization, optical properties and free and clamped linear eletrooptic cofficients of batio$_3$ in the tetragonal phase. *Ferroelectrics*, 234(1-4):61, 1999.

[23] N. Setter and R. Waser. Electroceramic materials. *Acta mater.*, 48:151, 2000.

[24] M. Zgonik, P. Bernasconi, M. Duelli, R. Schlesser, and P. Günter. Dielectric, elastic, piezoelectric, electro-optic, and elasto-optic tensors of batio$_3$ crystals. *Phys. Rev. B*, 50(9):5941, 1994.

[25] J. P. Remeika. A method for growing barium titanate single crystals. *J. Am. Chem. Soc.*, 76(3):940, 1954.

[26] F. Schlaphof. Abbildung und manipulation ferroelektrischer domänen auf der oberfläche von batio$_3$ - einkristallen mit rasterkraftmikroskopie und optischer nahfeldmikroskopie. Diplomarbeit, Technische Universität Dresden, 2000.

[27] G. Tarrach, P. Lagos L., R. Hermans Z., F. Schlaphof, Ch. Loppacher, and L.M. Eng. Nanometer spot allocation for raman spectroscopy on ferroelectrics by polarization and piezoresponse force microscopy. *Appl. Phys. Lett.*, 79(19):3152, 2001.

[28] J. Y. Chang, C. F. Chu, C. Y. Huang, and R. R. Yueh. Optical and photorefractive properties of nb-doped batio$_3$. *J. Appl. Phys.*, 85(4):2318, 1999.

[29] T. Zhao, Z.-H. Chen, F. Chen, H.-B. Lu, and G.-Z. Yang. Electrical and optical properties of strongly reduced epitaxial batio$_3$ thin films. *Appl. Phys. Lett.*, 77(26):4338, 2000.

[30] T. Takenada and H. Nagata. Current status and prospects of lead-free piezoelectric ceramics. *J. Eur. Ceram. Soc.*, 25:2693, 2005.

[31] E. H. Synge. A suggested method for extending microscopic resolution into the ultramicroscopic region. *Philos. Mag.*, 6:356, 1928.

[32] B. Hecht, B. Sick, U. P. Wild, V. Deckert, R. Zenobi, O. J. F. Martin, and D. W. Pohl. Scanning near-field optical microscopy with aperture probes: Fundamentals and applications. *J. Chem. Phys.*, 112(18):7761, 2000.

[33] G. Genolet, M. Despont, P. Vettinger, U. Staufer, W. Noell, N. F. Rooji, T. Cueni, M.-P. Bernal, and F. Marquis-Weible. Micromachined photoplastic probe for scanning near-field optical microscopy. *Rev. Sci. Instrum.*, 72(10):3877, 2001.

[34] L. Novotny and C. Hafner. Light propagation in a cylindrical waveguide with a complex, metallic, dielectric function. *Phys. Rev. E*, 50(5):4094, 1994.

[35] R. Hillenbrand and F. Keilmann. Complex optical constants on a subwavelength scale. *Phys. Rev. Lett.*, 85(14):3029, 2000.

[36] M. B. Raschke and C. Lienau. Apertureless near-field optical microscopy: Tip–sample coupling in elastic light scattering. *Appl. Phys. Lett.*, 83(24):5089, 2003.

[37] J. Renger, S. Grafström, L. M. Eng, and V. Deckert. Evanescent wave scattering and local electric field enhancement at ellipsoidal silver particles in the vicinity of a glass surface. *J. Opt. Soc. Am. A*, 21:1362, 2004.

[38] A. Bek, R. Vogelgesang, and K Kern. Optical nonlinearity versus mechanical anharmonicity contrast in dynamic mode apertureless scanning near-field optical microscopy. *Appl. Phys. Lett.*, 87:163115, 2005.

[39] R. Stöckle, C. Fokas, V. Deckert, R. Zenobi, B. Sick, B. Hecht, and U.P. Wild. High-quality near-field optical probes by tube etching. *Appl. Phys. Lett.*, 75(2):160, 1999.

[40] Y. D. Suh and R. Zenobi. Improved probes for scanning near-field optical microscopy. *Adv. Mater.*, 12(15):1139, 2000.

[41] A. Lazarev, N. Fang, Q. Luo, and X. Zhang. Formation of fine near-field scanning optical microscopy tips. part i. by static and dynamic chemical etching. *Rev. Sci. Instrum.*, 74(8):3679, 2003.

[42] T. Okayama and H. Seki. Fabrication and evaluation of silica-based optical fiber probes by chemical etching method. *Optical Review*, 12(1):25, 2005.

[43] P.-K. Wei, Y.-C. Chen, and H.-L. Kuo. Systematic variation of polymer jacketed fibres and the effects on tip etching dynamics. *J. of Microscopy*, 210(3):334, 2002.

[44] J. Shi and X. R. Qin. Formation of glass fiber tips for scanning near-field optical microscopy by sealed- and open-tube etching. *Rev. Sci. Instrum.*, 76:013702, 2005.

[45] T. Otto, S. Grafström, J. Seidel, and L.M. Eng. Novel transparent electrodes for electro-optical near-field microscopy. *SPIE Int. Soc. Opt. Eng. Adv. Mater.: Advanced optical materials*, 5122:366, 2003.

[46] S. Trogisch. Aufbau der abtasteinrichtung eines optischen nahfeldmikroskopes / photonenrastermikroskopes. Diplomarbeit, Technische Universität Dresden, 1997.

[47] K. Karrai and R.D. Grober. Piezoelectric tip-sample distance control for nearfield optical microscopes. *Appl. Phys. Lett.*, 66(14):1842, 1995.

[48] R. Brunner, O. Marti, and O. Hollricher. Influence of environmental conditions on shear–force distance control in near-field optical microscopy. *J. Appl. Phys.*, 86(12):7100, 1999.

[49] P. K. Wei and W. S. Fann. The effect of humidity on probe-sample interactions in near-field scanning optical microscopy. *J. Appl. Phys.*, 87(5):2561, 2000.

[50] M. Schenk, M. Füting, and R. Reichelt. Direct visualization of the dynamic behaviour of a water meniscus by scanning electron microscopy. *J. Appl. Phys.*, 84(9):4880, 1998.

[51] J.U. Schmidt, H. Bergander, and L.M. Eng. Shear force interaction in the viscous damping regime studied at 100 pn force resolution. *J. Appl. Phys.*, 87(6):3108, 2000.

[52] M. Antognozzi, A. D. L. Humphris, and M. J. Miles. Observation of molecular layering in a confined water film and study of the layers viscoelastic properties. *Appl. Phys. Lett.*, 78(3):300, 2001.

[53] A. L. Gruverman, J. Hatano, and H. Tokumoto. Scanning force microscopy studies of domain structures in batio$_3$ single crystals. *Jpn. J. Appl. Phys.*, 36(4A):2207–2211, 1997.

[54] M. Abplanalp, L.M. Eng, and P. Günter. Mapping the domain distribution at ferroelectric surfaces by scanning force microscopy. *Appl. Phys. A*, 66:S231, 1998.

[55] A. Rüdiger, T. Schneller, A.Roelofs, S. Tiedke, T. Schmitz, and R. Waser. Nanosize ferroelectric oxides - tracking down the superparaelectric limit. *Appl. Phys. A*, 80:1247, 2005.

[56] F. Schlaphof. *Kraftmikroskopische Untersuchungen dünner ferroelektrischer Filme.* PhD thesis, Technische Universität Dresden, 2005.

[57] H. Chaib. *Étude théorique des propriétés ferroélectriques, optiques et électrooptiques de $BaTiO_3$ et $KNbO_3$ dans la phase quadratique.* PhD thesis, Université Ibn Zohr, Agadir, 2000.

[58] N. V. Perelomova and M. M. Tagieva. *Problems in Crystal Physics with Solutions.* Mir Publishers Moscow, 1983.

[59] C. Hubert and J. Levy. Confocal scanning optical microscopy of $\mathrm{ba}_x\mathrm{sr}_{1-x}\mathrm{tio}_3$. *Appl. Phys. Lett.*, 71(23):3353, 1997.

[60] O. Tikhomirov, B. Red'kin, A. Trivelli, and J. Levy. Visualization of 180° domain structures in uniaxial ferroelectrics using confocal scanning optical microscopy. *J. Appl. Phys.*, 87(4):1932, 2000.

[61] C. Hubert and J. Levy. Nanometer-scale imaging of domains in ferroelectric thin films using apertureless near-field scanning optical microscopy. *Appl. Phys. Lett.*, 73(22):3229, 1998.

[62] H. Heinzelmann and D. W. Pohl. Scanning near-field optical microscopy. *Appl. Phys. A*, 59:89, 1994.

[63] Pingsheng Tang, D. J. Towner, T. Hamano, A. L. Meier, and B. W. Wessels. Electrooptic modulation up to 40 ghz in a barium titanate thin film waveguide modulator. *Optics Express*, 12(24):5962, 2004.

[64] B. Hecht, H. Bielefeldt, Y. Inouye, D. W. Pohl, and L. Novotny. Facts and artifacts in near-field optical microscopy. *J. Appl. Phys.*, 81(6):2492, 1997.

[65] A. Rüdiger, T. Schneller, A.Roelofs, S. Tiedke, T. Schmitz, and R. Waser. Nanosize ferroelectric oxides - tracking down the superparaelectric limit. *Appl. Phys. A*, 80:1247, 2005.

[66] M. Dawber, I. Farnan, and J. F. Scott. A classroom experiment to demonstrate ferroelectric hysteresis. *Am. J. Phys.*, 71(8):819, 2003.

[67] S. Tiedke, T. Schmitz, K. Prume, A. Roelofs, T. Schneller, U. Kall, R. Waser, C. S. Ganpule, V. Nagarajan, A. Stanishevsky, and R. Ramesh. Direct hysteresis measurements of single nanosized ferroelectric capacitors contacted with an atomic force microscope. *Appl. Phys. Lett.*, 79(22):3678, 2001.

[68] S. Prasertchoung, V. Nagarajan, Z. Ma, R. Ramesh, J. S. Cross, and M. Tsukada. Polarization switching of submicron ferroelectric capacitors using an atomic force microscope. *Appl. Phys. Lett.*, 84(16):3130, 2004.

[69] A. Gruverman, H. Tokumoto, A. S. Prakash, S. Aggarwal, B. Yang, M. Wuttig, R. Ramesh, O. Auciello, and T. Venkatesan. Nanoscale imaging of domain dynamics and retention in ferroelectric thin films. *Appl. Phys. Lett.*, 71(24):3492, 1997.

[70] Ch. Loppacher, F. Schlaphof, S. Schneider, U. Zerweck, S. Grafström, L.M. Eng, A. Roelofs, and R. Waser. Lamellar ferroelectric domains in pbtio$_3$ grains imaged and manipulated by afm. *Surf. Sci.*, 523-533:483, 2003.

[71] S. V. Kalinin, A. Gruverman, and D. A. Bonnell. Quantitative analysis of nanoscale switching in srbi$_2$ta$_2$o$_9$ thin films by piezoresponse force microscopy. *Appl. Phys. Lett.*, 85(5):795, 2004.

[72] A. Roelofs, T. Schneller, K. Szot, and R. Waser. Piezoresponse force microscopy of lead titanate nanograins possibly reaching the limit of ferroelectricity. *Appl. Phys. Lett.*, 81(27):5231, 2002.

[73] S. V. Kalinin, A. Gruverman, B. J. Rodriguez, J. Shin, A. P. Baddorf, E. Karapetian, and M. Kachanov. Nanoelectromechanics of polarization switching in piezoresponse force microscopy. *J. Appl. Phys.*, 97:074305, 2005.

[74] L. M. Eng. Nanoscale domain engineering and characterization of ferroelectric domains. *Nanotechnology*, 10:405, 1999.

[75] Y. Rosenwaks, D. Dahan, M. Molotskii, and G. Rosenman. Ferroelectric domain engineering using atomic force microscopy tip arrays in the domain breakdown regime. *Appl. Phys. Lett.*, 86:012909, 2005.

[76] J. Fousek and L. E. Cross. Open issues in application aspects of domains in ferroic materials. *Ferroelectrics*, 293:43, 2003.

[77] M. Molotskii, A. Agronin, P.Urenski, M. Shvebelman, G. Rosenman, and Y. Rosenwaks. Ferroelectric domain breakdown. *Phys. Rev. Lett.*, 90(10):107601, 2003.

[78] A. Agronin, Y. Rosenwaks, and G. Rosenman. Ferroelectric domain reversal in linbo$_3$ crystals using high-voltage atomic force microscopy. *Appl. Phys. Lett.*, 85(3):452, 2004.

[79] A. Gruverman, B. J. Rodriguez, C. Dehoff, J. D. Waldrep, A. I. Kingon, R. J. Nemanich, and J. S. Cross. Direct studies of domain switching dynamics in thin film ferroelectric capacitors. *Appl. Phys. Lett.*, 87:082902, 2005.

[80] W. J. Merz. Domain formation and domain wall motions in ferroelectric batio$_3$ single crystals. *Phys. Rev.*, 95(3):690, 1954.

[81] C. Hubert and J. Levy. New optical probe of ghz polarization dynamics in ferroelectric thin films. *Rev. Sci. Instrum.*, 70(9):3684, 1999.

[82] E. D. Mishina, N. E. Sherstyuk, V. I. Stadnichuk, A. S. Sigov, V. M. Mukhorotov, Yu. I. Golovko, A. van Etteger, and Th. Rasinga. Nonlinear-optical probing of nanosecond ferroelectric switching. *Appl. Phys. Lett.*, 83(12):2402, 2003.

[83] S. Grafström. Reflectivity of a stratified half-space: the limit of weak inhomogeneity and anisotropy. *J. Opt. A: Pure Appl. Opt.*, 8:134, 2006.

[84] H. Chaib, L.M. Eng, and T. Otto. Surface effect on the electrical and optical properties of barium titanate at room temperature. *Phys. Rev. B*, 71:085418, 2005.

[85] M. Veithen and Ph. Ghosez. Temperature dependence of the electro-optic tensor and refractive indices of batio$_3$ from first principles. *Phys. Rev. B*, 71:132101, 2005.

[86] T. Jach, S. Kim, V. Gopalan, S. Durbin, and D. Bright. Long-range strains and the effects of applied field at 180° ferroelectric domain walls in lithium niobate. *Phys. Rev. B*, 69:064113, 2004.

[87] S. Kim and V. Gopalan. Optical index profile at an antiparallel ferroelectric domain wall in lithium niobate. *Materials Science and Engineering B*, 120:91, 2005.

[88] D. Khatib, H. Chaib, and W. Kinase. Theoretical study of refractive indices, birefringence and spontaneous polarization of batio$_3$ at room temperature. *Physica B*, 269:200, 1999.

[89] H. Chaib, D. Khatib, and W. Kinase. Theoretical study of optical properties and linear electro-optic coefficients r_c and r_{42} of tetragonal batio$_3$. *Nonlinear Optics*, 23:97, 2000.

[90] H. Chaib, T. Otto, and L.M. Eng. Electrical and optical properties of linbo$_3$ single crystals at room temperature. *Phys. Rev. B*, 67:174109, 2003.

[91] T. Taubner, R. Hillenbrand, and F. Keilmann. Performance of visible and mid-infrared scattering-type near-field optical microscopes. *Journal of Microscopy*, 210:311, 2002.

[92] Chaib et al. Bragg reflector from ferroelectric domain walls. (manuscript in prep.).

[93] Ch. Loppacher, U. Zerweck, and L. M. Eng. Kelvin probe force microscopy of alkali chloride thin films on au(111). *Nanotechnology*, 15:S9, 2004.

[94] U. Zerweck, Ch. Loppacher, T. Otto, S. Grafström, and L.M. Eng. Accuracy and resolution limits of kelvin probe force microscopy. *Phys. Rev. B*, 71:125424, 2005.

[95] C. Gerthsen and H. Vogel. *Physik*. Springer-Verlag, Berlin Heidelberg New York, 17. edition, 1993.

List of Figures

List of Tables

Publications

Papers

H. Chaib, L.M. Eng, and T. Otto. *Surface effect on the electrical and optical properties of barium titanate at room temperature.* Phys. Rev. B **71**, 085418 (2005).

U. Zerweck, Ch. Loppacher, T. Otto, S. Grafström, and L.M. Eng. *Accuracy and resolution limits of Kelvin probe force microscopy.* Phys. Rev. B **71**, 125424 (2005).

Ch. Loppacher, U. Zerweck, S. Teich, E. Beyreuther, T. Otto, S. Grafström, and L.M. Eng. *FM demodulated Kelvin Probe Force Microscopy for Surface Photovoltage Tracking.* Nanotechnology **16**, S1–S6 (2005).

H. Chaib, L.M. Eng, and T. Otto. *Dielectric polarization and refractive indices of ultrathin barium titanate films on strontium titanate single crystals.* J. Phys.: Condens. Matter **17**, 161 (2005).

L. M. Eng, S. Grafström, I. Hellmann, C. Loppacher, T. Otto, J. Renger, F. Schlaphof, J. Seidel, and U. Zerweck. *Nanoscale nondestructive electric field probing in ferroelectrics, organic molecular films, and near-field optical nanodevices.* Proc. SPIE **5392**, 21 (2004).

H. Chaib, T. Otto, and L.M. Eng. *Modeling the Electrical and Optical Properties of $BaTiO_3$ and $LiNbO_3$ Single Crystals at Room Temperature.* Ferroelectrics **304**, 93 (2004).

T. Otto, S. Grafström und L. M. Eng. *Electric Field Modeling in Anisotropic Dielectrics.* Ferroelectrics **303**, 149 (2004).

T. Otto, S. Grafström, H. Chaib und L. M. Eng. *Probing the nanoscale electro-optical properties in ferroelectrics.* Appl. Phy. Lett. **84**, 1168 (2004).

T. Otto, S. Grafström, J. Seidel, and L.M. Eng. *Novel transparent electrodes for electro-optical near-field microscopy.* SPIE Int. Soc. Opt. Eng. Adv. Mater.: Advanced optical materials **5122**, 366 (2003).

H. Chaib, S. Grafström, T. Otto, and L. M. Eng. *Ferroelectric and optical properties in the 180° ferroelectric domain wall of tetragonal $BaTiO_3$.* SPIE Int. Soc. Opt. Eng. Adv. Mater.: Advanced optical materials **5122**, 358 (2003).

H. Chaib, F. Schlaphof, T. Otto, and L.M. Eng. *Electrical and Optical Properties in the 180° Ferroelectric Domain Wall of Tetragonal $KNbO_3$.* Ferroelectrics **291**, 143 (2003).

H. Chaib, F. Schlaphof, T. Otto, and L.M. Eng. *Electric and optical properties of the 90° ferroelectric domain walls in tetragonal barium titanate.* Journal of Physics: Condensed Matter **15**, 8927 (2003).

H. Chaib, T. Otto, and L.M. Eng. *Electrical and optical properties of $LiNbO_3$ single crystals at room temperature.* Phys. Rev. B **67**, 174109 (2003).

H. Chaib, T. Otto, and L. M. Eng. *Theoretical Study of Ferroelectric and Optical Properties in the 180° Ferroelectric Domain Wall of Tetragonal $BaTiO_3$.* Phys. Stat. Sol. (b) **233 (2)**, 250 (2002).

Talks and posters

H. Chaib, T. Otto, and L. M. Eng.
Electrical, optical, and electrooptical properties of $BaTiO_3/SrTiO_3$ superlattices with symmetric and asymmetric structures.
Talk, DPG spring meeting, Berlin 2005.

T. Otto, S. Grafström, F. Schlaphof, H. Chaib, and L. M. Eng
Collecting nanoscale optical hysteresis in ferroelectrics.
Talk, DPG spring meeting, Berlin 2005.

Ch. Loppacher, U. Zerweck, T. Otto, S. Grafström, and L.M. Eng
Accuracy and Resolution of Quantitative Kelvin Probe Force Microscopy.
Poster, DPG spring meeting, Berlin 2005.

U. Zerweck, Ch. Loppacher, T. Otto, S. Grafström, and L.M. Eng
Resolution and Accuracy of Quantitative Kelvin Probe Force Microscopy.
Poster, 7th International Conference on Non-Contact Atomic Force Microscopy (NC-AFM), Seattle (USA), 2004.

T. Otto, F. Schlaphof, H. Chaib, S. Grafström, and L. M. Eng
Collecting nanoscale optical hysteresis in ferroelectrics.
Poster, The 8th International Symposium of Ferroic Domains (ISFD-8), Tsukuba (Japan), 2004.

T. Otto, S. Grafström, F. Schlaphof, H. Chaib, and L. M. Eng
Imaging ferroelectric domains by electro-optically modulated near-field microscopy.
Talk, The 10th European Meeting on Ferroelectricity (EMF-10), Cambridge (UK), 2003.

T. Otto, S. Grafström, F. Schlaphof, H. Chaib, and L. M. Eng
Electro-optical imaging of ferroelectric domains by scanning near-filed microscopy.
Poster, The 10th European Meeting on Ferroelectricity (EMF-10), Cambridge (UK), 2003.

T. Otto, S. Grafström, F. Schlaphof, H. Chaib, and L. M. Eng
Imaging ferroelectric domains by electro-optically modulated near-field microscopy.
Talk, 7th meeting of Near-field optical microscopy and related topics (NFO 7), Rochester (NY, USA), 2002.

H. Chaib, S. Grafström, T. Otto, and L. M. Eng
Theoretical study of ferroelectric and optical properties in the 180^o ferroelectric domain wall of tetragonal BaTiO3.
Poster, 3rd International Conference on Advanced Optical Materials and Devices (AOMD-3), Riga (Lettonie), 2002

T. Otto, S. Grafström, F. Schlaphof, H. Chaib, and L. M. Eng
Abbildung ferroelektrischer Domänen mittels elektrooptisch modulierter Nahfeldmikroskopie.
Talk, DPG spring meeting, Regensburg, 2002.

T. Otto, S. Grafström, F. Schlaphof, H. Chaib, and L. M. Eng
3D-imaging of ferroelectric domains by electro-optially modulated near-field microscopy.
Poster, DPG spring meeting, Regensburg, 2002.

Acknowledgements

At this point, I would like to thank all those who have contributed to this work in many ways.

First of all, Prof. Lukas Eng initiated this challenging research and stimulated this work with lots of ideas and recommendations. He provided the necessary infrastructure and funding, and gave me the opportunity to present the results at conferences.

Dr. Stefan Grafström helped me with careful discussions and recommendations to understand the matter in more detail. He also spent a lot of time on intensive proof reading of this thesis.

Dr. Hassan Chaib developed the theoretical description for the optical properties of single domain walls.

The members of the SPM^2 group are a great source of stimulation. They motivated me with discussions, crazy ideas, and interesting projects. They also helped me by lending me various parts and devices, as well as providing me with sufficient lab time, without this, I could not have carried out all the experiments.

I wish to thank all members of the Photophysics department who keep the institute working. S. Furkert etches the SNOM tips we use, V. Trepte makes the smallest mechanical parts, R. Raupach repairs broken electrical devices, K. Schmidt keeps the computers and network running, and last but not least, E. Schmidt, A. Wortmann, and H. Fröb protect us from to much administrative work.

The exciting atmosphere at this institute and especially in the SPM^2 group make me enjoy working. I thank all people I use to meet during the coffee breaks as well as the occupants of the "cubicle of the year" for inspiring conversation. Additionally, it is always a pleasure to bring in my voice in the choir of the institute.

Finally, I want to thank my family, especially my parents and my fiancée Sandra for encouragement and caring support during my studies.

Die vorliegende Arbeit wurde am Institut für Angewandte Physik der Technischen Universität Dresden unter wissenschaftlicher Betreuung von Prof. Dr. Lukas M. Eng durchgeführt.

Versicherung

Hiermit versichere ich, dass ich die vorliegende Arbeit ohne unzulässige Hilfe Dritter und ohne Benutzung anderer als der angegebenen Hilfsmittel angefertigt habe; die aus fremden Quellen direkt oder indirekt übernommenen Gedanken sind als solche kenntlich gemacht. Die Arbeit wurde bisher weder im Inland noch im Ausland in gleicher oder ähnlicher Form einer anderen Prüfungsbehörde vorgelegt.

Dresden, den 17.01.2006 Tobias Otto